RESOURCE EFFICIENT FPGA IMPLEMENTATION AND WEIGHTED LOGARITHMIC MODEL FOR ENHANCEMENT OF FOG DEGRADED IMAGES

Submitted in
fulfillment of the requirements for the degree of

Doctor of Philosophy

by

Hitendra Gupta
2008REC502

Under the supervision of

Prof. K.K Sharma

DEPARTMENT OF ELECTRONICS AND COMMUNICATION ENGINEERING

MALAVIYA NATIONAL INSTITUTE OF TECHNOLOGY JAIPUR

December 2019

DECLARATION

I, **Hitendra Gupta**, declare that this thesis titled, "**RESOURCE EFFICIENT FPGA IMPLEMENTATION AND WEIGHTED LOGARITHMIC MODEL ENHANCEMENT OF WEATHER DEGRADED IMAGES** " and the work presented in it, are my own. I confirm that:

- This work was done wholly or mainly while in candidature for a research degree at this university.

- Where any part of this thesis has previously been submitted for a degree or any other qualification at this university or any other institution, this has been clearly stated.

- Where I have consulted the published work of others, this is always clearly attributed.

- Where I have quoted from the work of others, the source is always given. With the exception of such quotations, this thesis is entirely my own work.

I have acknowledged all main sources of help.

Where the thesis is based on work done by myself, jointly with others, I have made clear exactly what was done by others and what I have contributed myself.

Date:

Hitendra Gupta

(2008REC502)

CERTIFICATE

This is to certify that this Thesis entitled **"RESOURCE EFFICIENT FPGA IMPLEMENTATION AND WEIGHTED LOGARITHMIC MODEL FOR ENHANCEMENT OF FOG DEGRADED IMAGES"** being submitted by **Hitendra Gupta (2008REC502)** is a bonafide research work carried out under my supervision and guidance in fulfillment of the requirement for the award of the degree of Doctor of Philosophy in the Department of Electronics and Communication Engineering, Malaviya National Institute of Technology, Jaipur, India. The matter embodied in this thesis is original and has not been submitted to any other University or Institute for the award of any other degree.

Place: Jaipur
Date:

K.K. Sharma
Professor
Dept. of ECE
MNIT Jaipur

Acknowledgment

I would like to profusely thank my guide Prof. K.K. Sharma and Prof. S.D. Joshi for their timely advice and encouragement throughout my work and for reviewing my work from time to time. A special note of gratitude goes to Jean-Charles Pinoli for the support he extended to this work by sending his research articles all the way from France via post. I would also like to thank my parents, wife and my son for all the support and motivation provided by them. I would also like to thank all who helped me during my work.

Hitendra Gupta

Abstract

Real time image enhancement systems require benchmark speed and robustness. These systems require extensive post processing of the acquired images in order to improve the visibility and detect ability of image features. The information content of the images captured in misty and scattering media such as fog, haze, and smoke are low and hence suffers from degradation in visibility. In such media, the radiance and transmittance from a scene point radically gets diffused and modulated. This thesis work presents a novel method for enhancement of weather degraded images, single stage pipeline VLSI architecture of the same and that of the conventional image enhancement algorithms. The proposed enhancement method is based upon the logarithmic image processing (LIP) framework and human visual system (HVS). The proposed method uses multiple images of the same scene in order to increase the information content and produce a visibly enhanced resultant image. Another method based on Hilbert Vibration Decomposition (HVD) is also illustrated here in this thesis along with its experimental results. A region based contrast measure called the logarithmic region contrast measure (LRCM) for finding the optimal value of parameters and its comparison with other traditional contrast measures (some are based on Entropy) has been presented here in this thesis. The experimental results on two data sets of weather degraded images that are captured by a conventional silicon sensor camera (Sony DSC-W210) are also included. A resource efficient image enhancement processor architecture is also presented here. A comparison of the hardware and operating speed of the proposed architectures is also included here in this thesis. It has been illustrated that the proposed architectures can easily be embedded on an existing image sensing system which improves the versatility and throughput of the system significantly.

CONTENTS

List of Figures

List of Tables

List of Abbreviation

1.	HVS	Human Visual System
2.	CLIP	Conventional Linear Image Processing
3.	FPGA	Field Programmable Gate Array
4.	DSP	Digital Signal Processor
5.	DMA	Direct Memory Access
6.	ASIC	Application Specific Integrated Circuits
7.	RAM	Random Access Memory
8.	LIP	Logarithmic Image Processing
9.	HVD	Hilbert Vibration Decomposition
10.	EME	Weber Law Based Measure of Enhancement
11.	EMEE	Weber Law Based Measure of Enhancement using Entropy
12.	AME	Michelson Law Based Measure of Enhancement
13.	AMEE	Michelson Law Based Measure of Enhancement using Entropy
14.	LRCM	Logarithmic Region Based Contrast Measure
15.	FSM	Finite State Machine
16.	RTL	Register Transfer Logic

Chapter 1

Introduction

In this chapter section 1.1 describes difference between generalized image enhancement and adaptive image enhancement, section 1.2 elaborates upon enhancement of fog degraded digital images, further section 1.3 describes the organization of the Thesis.

1.1 Image Enhancement

Adaptive image enhancement is a process that improves the feature of the image adaptively for a particular task. Enhancing degraded and noisy images, increasing contrast, and revealing details are examples of enhancement operations. Image enhancement can be performed in two domains viz. spatial domain and frequency domain [1]. The term spatial domain refers to the image plane itself and approaches in this category are based on direct manipulation of pixels in an image. Frequency domain processing techniques are based on modifying the Fourier transform of an image [1].

1.1.1 Motivation

The existing enhancement/restoration algorithms either addresses all category of images or are computationally slow to be implemented in hardware. Thus, there is an immense need of the algorithms/methods that can enhance the visibilty of the images/scenes, depending upon their characteristics as well as are computationally faster, to be able to be implemented into hardware.

1.1.2 Problem Statement

The present research work is done to propose image enhancement algorithms which can improve the visibility of the fog degraded images. Here, work is also done to

propose and implement the VLSI architecture of a system that executes the proposed algorithms. The systems are designed in such a way that they may either be embedded onto the framework of the existing medical imaging systems, i.e, CT Scan Machine, Digital X-Ray Machine etc., or they may be installed onto the aircraft, ship and automobiles, that faces problem of poor visibilty in the bad weather, and hence will reduce the risk of the life of the passengers.

The mentioned image enhancement systems, specially designed for medical images can also be used for the prediagnosis of the critical diseases, and will help the doctor in accurate diagnosis, which is a key problem in prescribing the right treatment to the patient.

1.2 Enhancement of Fog Degraded Digital Images

The information content of the images captured in the scattering media such as fog, haze, and smoke is low and hence suffers from degradation in visibility. In such media, the radiance and transmittance from a scene point radically gets diffused and modulated. Enhancement of such images formed by transmitted light [2] or the human visual system (HVS) [3] may not comply with the classical linear image processing (CLIP) techniques [4], [5], [6]. These images acquired under murky atmosphere results in the information content loss which increases with increase in distance [7]. Retrieving or improving the visual information in poor visibility is significant for various machine vision and user-assisted applications such as aircraft traffic, mapping, surveillance, navigation, and on-road visibility. There is, thus, a growing interest in the analysis and enhancing the visibility of weather degraded images [7], [8], [9], [10].

1.3 Organization of the Thesis

Chapter 2 consists of literature survey, which describes the previous work related to enhancement of fog degraded images. It also includes the comparison of FPGA , DSP and Microprocessor for implementation of the proposed model as well as the adaptive image enhancement techniques.

Chapter 3 discusses the proposed weighted logarithmic model for the enhancement of fog degraded images and HVD based enhancement for fog degraded images. It also includes a novel contrast measures used for the measurement of contrast of fog degraded images. An analysis of the computational complexity and the resource efficient FPGA implementation of the proposed model is also included here in this chapter. Here we also present the simulation results of the proposed image enhancement methods onto two sets of experimental image data of on road weather degraded images (Distant Vehicle and Letter Board). We compare the results of the proposed method using the basic LIP model, method using conventional multiplicative parameters and the result of the method using logarithmic multiplicative parameters. We also compare the enhancement results of the proposed method with the result of histogram equalization. For finding the optimum parameters; we use the presented measure LRCM and compare the same with those found using AMEE.

Chapter 4 The conventional linear image enhancement algorithms that are made adaptive to medical images along with their resource efficient architectures are included in this chapter.

Chapter 5 Conclusions and future work are included in this followed by references.

Chapter 2

Literature Survey

This chapter describes literature review on enhancement of fog degraded images in section 2.1 followed by a comparison between FPGA, DSP and Microprocessor.

2.1 Fog Degraded Images

Several methods have been proposed to restore good visibility of fog degraded images. Nayar et al.[7] [8] [34] illustrates that virtually all the work in the enhancement of fog degraded images is based on the assumption that the observer is immersed in a transparent medium (air). It is assumed that light rays reflected by scene objects travel to the observer without attenuation or alteration. Under this assumption, the brightness of an image point depends solely on the brightness of a single point in the scene. Quite simply, existing vision sensors and algorithms have been created only to function on "clear" days. A robust image enhancement system, however, must abide by with the entire spectrum of weather conditions, including, haze, fog, etc [7]. Atmospheric optics lies at the heart of the most magnificent visual experiences known to man, including, the colors of sunrise and sunset, the blueness of the clear sky, and the rainbow [7]. The key characteristics of light, such as its intensity and color, are altered by its interactions with the atmosphere. These interactions can be broadly classified into three categories, namely, scattering, absorption and emission. Of these, scattering due to suspended particles is the most pertinent to us. As can be expected, this phenomenon leads to complex visual effects. So, at first glance, atmospheric scattering may be viewed as no more than a hindrance to an observer. However, it turns out that bad weather can be put to good use. The farther light

has to travel from its source (say, a surface) to its destination (say, a camera), the greater it will be affected by the weather.

They conferred on various types of weather conditions and their formation processes and summarized two models of atmospheric scattering – attenuation and airlight. These are the most pertinent to a Human Visual System (HVS). Using these models they recovered the depth map of the scene for enhancing it. Nayar et al. [7] very well describes that fog is formed when the relative humidity of air reaches saturation then by the process of condensation water droplets of about 1-10 μm are formed at a concentration of 100-10 cm^{-3} as described by Table 1.

Table 1
Weather conditions and associated particle types, sizes and concentrations [7]

Condition	Particle type	Radius (μm)	Concentration (cm^{-3})
Air	Molecule	10^{-4}	10^{19}
Haze	Aerosol	10^{-2}–1	10^{3}–10
Fog	Water droplet	1–10	100–10
Cloud	Water droplet	1-10	300-10
Rain	Drop	10^{2} - 10^{4}	10^{-2} – 10^{-5}

The size of particles produce a number of weather conditions which we have described below.

Haze: Haze is constituted of aerosol which is a dispersed system of small particles suspended in gas. Haze has a diverse set of sources including volcanic ashes, foliage exudation, combustion products, and sea salt [7]. The particles produced by these sources respond quickly to changes in relative humidity and act as nuclei (centers) of small water droplets when the humidity is high. Haze particles are larger than air

molecules but smaller than fog droplets. Haze tends to produce a distinctive gray or bluish hue and is certain to effect visibility.

Fog: Fog evolves when the relative humidity of an air parcel reaches saturation. Then, some of the nuclei grow by condensation into water droplets. Hence, fog and certain types of haze have similar origins and an increase in humidity is sufficient to turn haze into fog. This transition is quite gradual and an intermediate state is referred to as mist. While perceptible haze extends to an altitude of several kilometers, fog is typically just a few hundred feet thick. A practical distinction between fog and haze lies in the greatly reduced visibility induced by the former. There are many types of fog (ex., radiation fog, advection fog, etc.) which differ from each other in their formation processes [8].

Cloud: A cloud differs from fog only in existing at higher altitudes rather than sitting at ground level. While most clouds are made of water droplets like fog, some are composed of long ice crystals and ice-coated dust grains. For now, clouds are of less relevance to us as we restrict ourselves to vision at ground level rather than high altitudes.

Rain and Snow: The process by which cloud droplets turn to rain is a complex one [9]. When viewed up close, rain causes random spatial and temporal variations in images and hence must be dealt with differently from the more static weather conditions mentioned above. Similar arguments apply to snow, where the flakes are rough and have more complex shapes and optical properties [10], [11]. Snow too, we will set aside for now.

Schechner, Narasimhan and Nayar [10], discuses that the limitations of physics based models are that they are based on some strong approximations. Satherley et al. [13]

[34] proposed a method for reversing contrast loss in diffuse daylight illumination conditions based on the principle of scattering (depicted in Fig. 1) which required information about the scene geometry.

The manner in which a particle scatters incident light depends on its material properties, shape and size. The exact form and intensity of the scattering pattern varies dramatically with particle size [7]. As seen in Fig. 1, a small particle (about 1/10 λ, where λ is the wavelength of light) scatters almost equally in the forward (incidence) and backward directions, a medium size particle (about 1/4 λ) scatters more in the forward direction, and a large particle (larger than λ) scatters almost entirely in the forward direction. Substantial theory has been developed to derive scattering functions and their relations to particle size distributions.

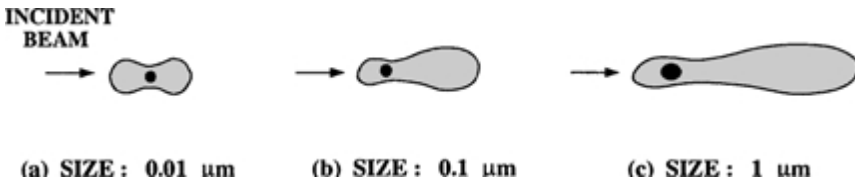

Fig. 1. A particle in the path of an incident light. [7]

Fig. 1 illustrates scattering by a single particle. Clearly, particles are accompanied in close proximity by numerous other particles. However, the average separation between atmospheric particles is several times the particle size. Hence, the particles can be viewed as independent scatters whose scattered intensities do not interfere with each other. This does not imply that the incident light is scattered only by a single article.

Multiple scatterings take place and any given particle is exposed not only to the incident light but also light scattered by other particles. A simple analogy is the inter-

reflections between scene points. In effect, multiple scattering causes the single scattering functions in Fig. 2. to get smoother and less directional.

Now, consider the simple illumination and detection geometry shown in Fig. 3.2. A unit volume of scattering medium with suspended particles is illuminated with spectral irradiance $E(\lambda)$ per cross section area. The radiant intensity $I(\theta, \lambda)$ of the unit volume in the direction θ of the observer is given as in [7]

$$I(\theta, \lambda) = \beta(\theta, \lambda) * E(\lambda) \quad (1)$$

Where, $\beta(\theta, \lambda)$ is the angular scattering coefficient. The radiant intensity $I(\theta, \lambda)$ is the flux radiated per unit solid angle, per unit volume of the medium. The irradiance $E(\lambda)$ is, as always, the flux incident on the volume per unit cross-section area. The total flux

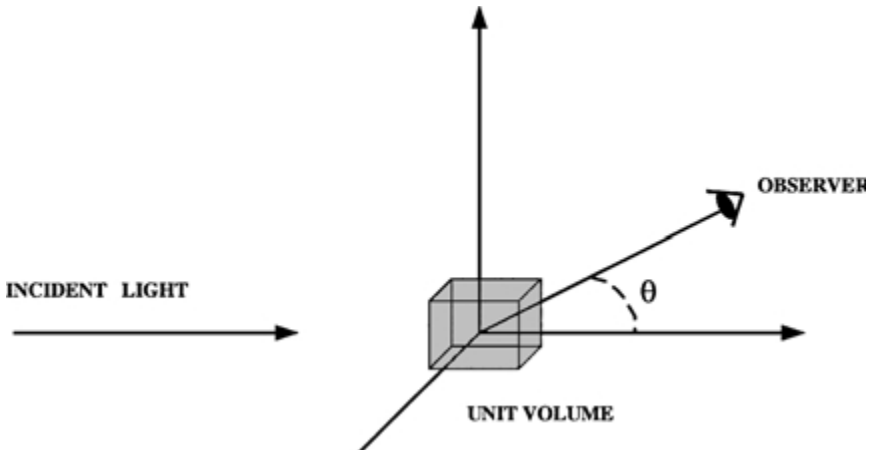

Fig. 2. A unit volume of randomly oriented suspended particles illuminated and observed [7].

Scattered (in all directions) by this volume is obtained by integrating over the entire sphere [7]:

$$\Phi(\lambda) = \beta(\lambda)E(\lambda) \quad (2)$$

where, $\beta(\lambda)$ is the total scattering coefficient. It represents the ability of the volume to scatter flux of a given wavelength in all directions. It is generally assumed that the coefficient $\beta(\lambda)$ is constant homogeneous medium over horizontal paths. To satisfy this constraint, we will restrict ourselves to the case where the observer is at (or close to) ground level and is interested not in the sky but other objects on (or close to) ground level. Also, we will assume that the atmosphere is more or less homogeneous in the scene of interest.

2.1.1 Attenuation

The first mechanism that is relevant to us is the attenuation of a beam of light as it travels through the atmosphere. This causes the radiance of a scene point to fall as its depth from the observer increases. Here, we will summarize the derivation of the attenuation model given in [7], [11]. Consider a collimated beam of light incident on the atmospheric medium, as shown in Fig. 3. The beam is assumed to have unit cross-sectional area. Consider the beam passing through an infinitesimally small sheet (lamina) of thickness dx. The fractional change in irradiance at location x can be written as in [7]:

$$\frac{dE(x,\lambda)}{E(x,\lambda)} = -\beta(\lambda)dx. \tag{3}$$

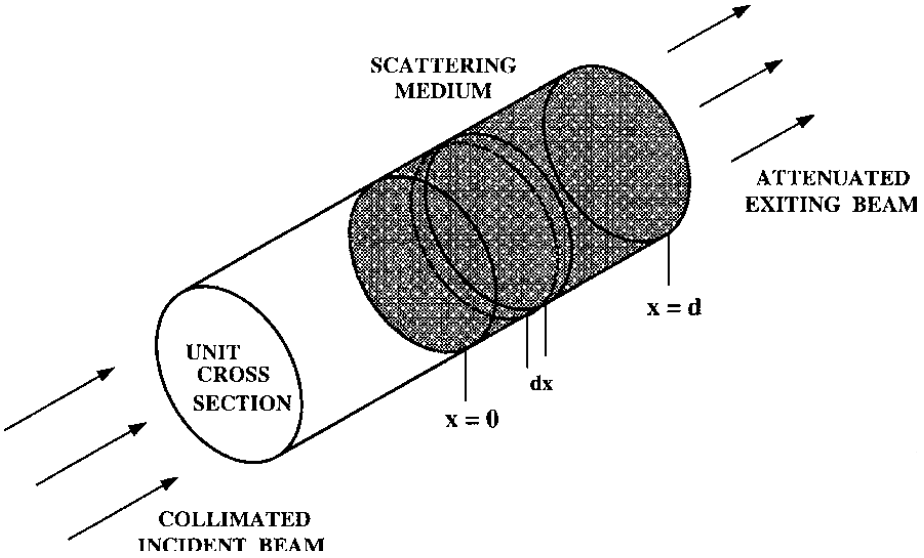

Fig. 3. Attenuation of a collimated beam of light by suspended particles [7].

By integrating both sides between the limits x = 0 and x = d we get the following equation as in [7]:

$$E(d, \lambda) = Eo(\lambda)e^{-\beta(\lambda)d} \tag{4}$$

where, $Eo(\lambda)$ is the irradiance at the source (x =0). This is Bouguer's exponential law of attenuation. At times, attenuation due to scattering is expressed in terms of optical thickness, $T = \beta(\lambda)d$. The utility of Bouguer's law is somewhat limited as it assumes a collimated source of incident energy. This is easily remedied by incorporating the inverse-square law for diverging beams from point sources [7]:

$$E(d,\lambda) = \frac{I_0(\lambda)e^{-\beta(\lambda)d}}{d^2} \tag{5}$$

Where, $Io(\lambda)$ is the radiant intensity of the point source. This is Allard's law. In deriving Allard's law, we have assumed that all scattered flux is removed from the incident

energy. The fraction of energy that remains, is called direct transmission and is given by expression (5).We have ignored the flux scattered in the forward direction (towards the observer) by each particle. Fortunately, this component is small in vision applications since the solid angles subtended by the source and the observer, with respect to each other are small. Finally, in some situations such as heavy fog, the exponential law may not hold due to significant multiple scatterings of light by atmospheric particles. Multiple scattering can also cause blurring in the image of a scene. In other words, the flux scattered out of an atmospheric column (visible to a pixel) enters another column (seen by a neighboring pixel).

2.1.2 Airlight

A second mechanism causes the atmosphere to behave like a source of light. This phenomenon is called airlight [13], [14] and it is caused by the scattering of environmental illumination by particles in the atmosphere. The environmental illumination can have several sources, including, direct sunlight, diffuse skylight and light reflected by the ground. While attenuation causes scene radiance to decrease with pathlength, airlight increases with pathlength. It therefore causes the apparent brightness of a scene point to increase with depth. It is now build upon derivation of airlight [4] as a function of pathlength. Consider the illumination and observation geometry shown in Fig. 3.2.1. The environmental illumination along the observer's line of sight is assumed to be constant but unknown in direction, intensity and spectrum. In effect, the cone of solid angle $d\omega$ subtended by a single receptor at the observer's end, and truncated by a physical object at distance d, can be viewed as a source of airlight. The infinitesimal volume dV at

distance x from the observer may be written as the product of the cross section area, $d\omega$ $x2$, and thickness dx: as in [7]

$$dV = d\omega\, x^2\, dx. \tag{6}$$

Irrespective of the exact type of environmental illumination incident upon dV, its intensity due to scattering in the direction of the observer is [7]:

$$d\, I(x, \lambda) = dV\, k\beta(\lambda) = d\omega x^2\, dx k\beta(\lambda), \tag{7}$$

where, β (λ) is the total scattering coefficient and the proportionality constant k accounts for the exact nature of the illumination and the form of the scattering function.

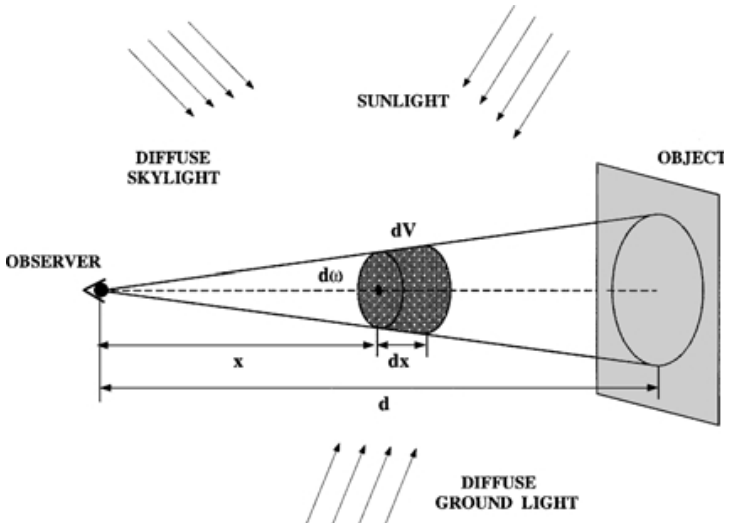

Fig. 4. The cone of atmosphere between an observer and an object scatters environmental illumination in the direction of the observer [7].

If we view element dV as a source with intensity $d\, I(x, \lambda)$, the irradiance it produces at the observer's end, after attenuation due to the medium, is given by [7]

$$dE(x,\lambda) = \frac{dI(x,\lambda)e^{-\beta(\lambda)x}}{x^2}, \tag{8}$$

We can find the radiance of dV from its irradiance as [7]:

$$dL(x,\lambda) = \frac{dE(x,\lambda)}{dw} = \frac{dI(x,\lambda)e^{-\beta(\lambda)x}}{dwx^2}, \tag{9}$$

By substituting (9) we get $dL(x, \lambda) = k\beta(\lambda)e^{-\beta(\lambda)x}\, dx$. Now, the total radiance of the pathlength d from the observer to the object is found by integrating this expression between x=0 and x=d: as in [7]

$$L(d, \lambda) = k(1 - e^{-\beta(\lambda)d}), \tag{10}$$

If the object is at an infinite distance (at the horizon), the radiance of airlight is maximum and is found by setting $d=\infty$ to get $L\infty(\lambda)=k$. Therefore, the radiance of airlight for any given pathlength d is given as [7]:

$$L(d, \lambda) = L\infty(\lambda)\,(1 - e^{-\beta(\lambda)d}), \tag{11}$$

As expected, the radiance of airlight for an object right in front of the observer (d = 0) equals zero. Of great significance to us is the fact that the above expression no longer includes the unknown factor k. Instead, we have the airlight radiance $L\infty(\lambda)$ at the horizon.

2.1.3 Depth of Light Sources from Attenuation

Consider the image of an urban setting taken at night (Fig. 5). Environmental illumination of the scene due to sunlight, skylight and reflected ground light are minimal and hence airlight can be safely ignored. The bright points in the image are mainly

sources of light such as street lamps and windows of lit rooms. On a clear night, these sources are visible to a distant observer in their brightest and clearest forms. As haze or fog sets in, the radiant intensities of the sources diminish due to attenuation. Our goal here is to recover the relative depths of the sources in the scene from two images taken under different (unknown) atmospheric conditions. Since environmental illumination is negligible at night, the image irradiance of a light source in the scene can be expressed using the attenuation model (5) as in [7]:

$$E(d,\lambda) = g\frac{I_0(\lambda)e^{-\beta(\lambda)d}}{d^2} \tag{12}$$

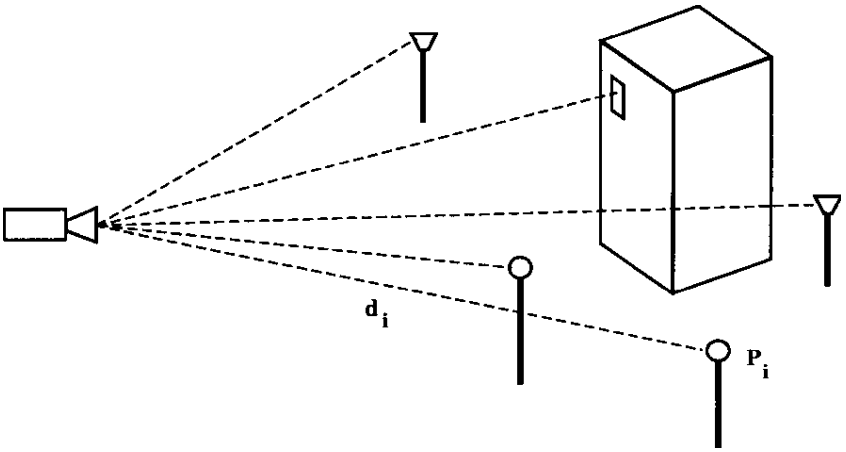

Fig. 5. The relative depths of sources of unknown intensities can be recovered from two images taken under different but unknown atmospheric conditions [7].

where, $Io(\lambda)$ is the radiant intensity of the source, d is the distance between the source and the camera and the constant gain g accounts for the optical parameters (aperture, for instance) of the camera. It is important to note that $\beta(\lambda)$ is the total scattering coefficient and not the angular one. We are assuming here that the lines of sight are not too inclined and hence all lines of sight pass through the same atmospheric conditions. This removes

all dependence on the exact form of the scattering function; the attenuation is determined by a single coefficient $\beta(\lambda)$ that is independent of viewing direction. If the detector of the camera has spectral response $s(\lambda)$, the final image brightness recorded is determined as [7]:

$$E' = \int s(\lambda)E(d,\lambda)d\lambda = \int gs(\lambda)\frac{I_0(\lambda)e^{-\beta(\lambda)d}}{d^2}d\lambda, \tag{13}$$

For the visible light spectrum, the relationship between the scattering coefficient β, and the wavelength λ, is given by the inverse power law (analogous to Rayleigh's law for small air particles) as in [7]:

$$\beta(\lambda) = \frac{Const.}{\lambda^{\gamma}} \tag{14}$$

where $\gamma \in [0, 4]$. Fortunately, for fog and dense haze, $\gamma \approx 0$ [15]. In these cases, β does *not* change appreciably with wavelength. Furthermore, since the spectral bandwidth of the camera is rather limited (visible light range for a gray-scale camera, and even narrower spectral bands when the camera is color), we will assume the scattering coefficient $\beta(\lambda)$ to be constant over this bandwidth. Then, we have the following equation as given by [7]:

$$E' = g\frac{e^{-\beta d}}{d^2}\int s(\lambda)I(\lambda)d\lambda = g\frac{e^{-\beta d}}{d^2}I' \tag{15}$$

Now consider two different weather conditions, say, mild and dense fog. Or, one of the conditions could be clear with $\beta = 0$. In either case we have two different attenuation coefficients, $\beta 1$ and $\beta 2$. If we take the ratio of the two resulting image brightness values, we get the following equation as in [7]:

$$R = \frac{E1'}{E2'} = e^{-(\beta 1 - \beta 2)d}$$

(16)

Using the natural log, we obtain: $R' = \ln R = -(\beta 1 - \beta 2)\, d$. This quantity is independent of the sensor gain and the radiant intensity of the source. In fact, it is nothing but the difference in optical thicknesses (DOT) of the source for two weather conditions. In the atmospheric optics literature, the term DOT is used as a quantitative measure of the "change" in weather conditions. Now, if we compute the DOTs of two different light sources in the scene (Fig. 5) and take their ratio, we determine the relative depths of the two source locations as given in [7]:

$$\frac{Ri'}{Rj'} = \frac{di}{dj} \tag{17}$$

Hence, the relative depths of all sources (with unknown radiant intensities) in the scene can be computed from two images taken under unknown but different haze or fog conditions. Fig. 6 below shows experimental results on the recovery of light sources from night images.

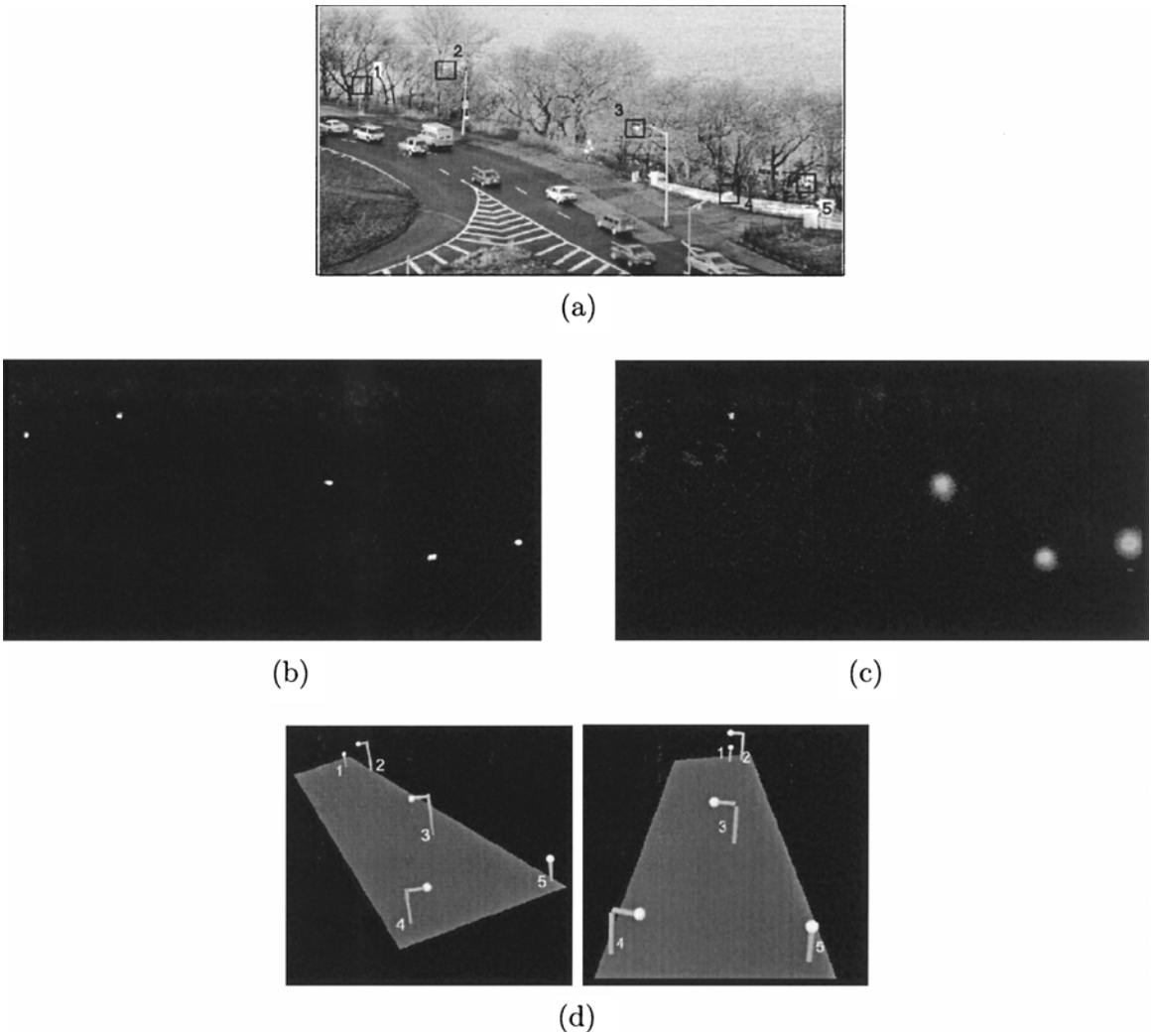

Fig. 6. Relative depths from brightness decay of point sources at night. (a) A scene with five light sources (street lamps). This image is shown only to convey the relative locations of the sources to the reader. (b) An image of the scene taken on a clear night. (c) An image of the scene taken on a foggy night. The three-dimensional coordinates of the five sources were computed from images (b) and (c). (d) Rotated graphical illustrations used to demonstrate the computed lamp coordinates (small bright spheres) [7].

Yitzhaky et al. [14] [34] restore image contrast for a single image that required a blur function. Petterson et al. [15] [34] proposed a method for a single image using direct transmission and the airlight, which is the model proposed by Nayar et al. [8].

Models based on the human visual system (HVS) have also been used for image enhancement [16] [34]. Some of these methods discriminate the edge and non-edge pixels by extracting the edge information of an image [17] [18] [34]. A few HVS based image enhancement model segments an image based upon background intensity and gradient [19] [20] [34].

Thus, due to the deficiency of a broad-spectrum hypothesis of image enhancement, the enhancement task of images is complicated. A successful automatic image enhancement requires an objective criterion for enhancement and an external evaluation of quality i.e. a contrast measure [21] [22] [34].

Recently Pal et al. [41] proposed dark channel prior technique (DCPT) in which they restored the contrast and color of the scene [41] which is a slightly different approach as compared to the proposed approach. Danve et al. [42] proposed fog correction using exponential contrast restoration [42] which is similar to the approach of Pal [41].

2.2 Hilbert Vibration Decomposition

Another technique called Hilbert vibration decomposition (HVD) was developed by Feldman [40] for decomposition of non-stationary and multicomponent dynamic signals. Its main idea is to decompose a signal into a sum of components with slowly-varying instantaneous amplitudes and frequencies [40]:

$$x(t) = \sum_i a_i(t) \cos\left(\int w_i(t) dt\right) \tag{18}$$

where $a_i(t)$ and $w_i(t)$ are the instantaneous amplitude and instantaneous frequency of the i^{th} component. Each mono-component in Eq. (20) is an intrinsic mode of the original

signal with a simple oscillatory waveform. If only one term is needed in Eq. (20) , is called a mono-component signal. Otherwise, it is referred to as a multicomponent signal with a broadband spectrum.

2.2.1 Hilbert Transform

Hilbert transform is one of the integral transform like Laplace and Fourier transform. It is named after David Hilbert, who first introduced it to solve a special case of integral equations in the area of mathematical physics [11]. The Hilbert transform of a function *x(t)* is defined by an integral transform [12]

$$H[x(t)] = \frac{1}{\pi} P \int_{-\infty}^{\infty} \frac{x(\tau)}{t-\tau}\, d\ \tau \tag{19}$$

in which *P* indicates the Cauchy principal value around t = τ. Physically, Hilbert transform is equivalent to a special kind of linear filter, where all the amplitudes of spectral components remain unchanged, but their phases are shifted by Π/2. Mathematically, the Hilbert transform of the original function represents a convolution of *x(t)* and *1/Πt*, which can be written as in [12]:

$$H[x(t)] = x(t) * \left(\frac{1}{\pi t}\right) \tag{20}$$

Note that the Hilbert transform of a time signal *x(t)* is another signal in time domain. If *x(t)* is real valued, *H[x(t)]* is also real valued.

2.2.2 Instantaneous Frequency of the Largest Energy Component

Consider a multicomponent signal with three harmonics as described by Eq. (21). Its analytic function can be derived as given in [12]:

$$z(t) = a_1(t)e^{j\int_0^t \omega_1(\tau)d\tau} + a_2(t)e^{j\int_0^t \omega_2(\tau)d\tau} + a_3(t)e^{j\int_0^t \omega_3(\tau)d\tau} \tag{21}$$

The instantaneous amplitude (IA) and instantaneous frequency (IF) of the analytic signal can be related to individual component parameters by the following equation as given in [12]:

$$a(t) = \left\{ a_1^2(t) + a_2^2(t) + 2a_1(t)a_2(t)\cos\left[\int_0^t \left[\quad \omega_2(\tau) - \omega_1(\tau) \right] d\tau \right] \right\}^{1/2} \qquad (22)$$

The signal envelope *a(t)* consists of a slowly varying part, including the sum of the squared of individual component amplitudes, and a rapidly varying (oscillating) part. The instantaneous frequency also has two parts: a slowly varying part and a rapidly varying asymmetrical oscillating part. The rapidly oscillating part of the instantaneous frequency has an important feature [40] . When the derivatives of both a_1 and a_2 are negligible and a_1 is significantly larger than a_2, the integration of the oscillatory part of the instantaneous frequency in one cycle related to the frequency difference of two components is approximately equal to zero. Therefore, the instantaneous frequency of the largest energy component can be extracted by a low-pass filter. For a more general case of three and more quasi-harmonics in the signal, the instantaneous frequency has a more complicated form. However, low pass filtering can still be used to extract the instantaneous frequency of the largest energy component.

2.3 FPGA versus DSP versus Microprocessor

In this work Field Programmable Gate Array (FPGA) is chosen to analyze the proposed resource efficient single stage pipeline architectures of adaptive image enhancement algorithms because software implementation of these requires processors (microprocessors, Digital Signal Processors (DSPs)) that work at very high clock frequency. At high clock frequency, the power requirement and dissipation are large [23] [36]. Moreover, the specialized image processing programs running on a computer cannot

adequately handle huge amounts of high-resolution images, since their processors are produced for general use [23] [24] [36]. The contemporary DSPs offer enough speed and architectural features for image processing (Direct Memory Access (DMA), multiple cores, vector processing, etc.), but at the cost of high clock rates, power consumption and unit price of the devices. Moreover the algorithms designed for a DSP cannot be highly parallel without using multiple DSPs. One area where DSPs are particularly powerful is the design of floating point systems, while for Application Specific Integrated Circuits (ASICs) and FPGAs, floating point operations are difficult to implement. For the scope of this work, this is not an issue because all the proposed architectures use fixed point operations only. In ASICs the circuit is fixed once fabricated, so it is impossible to modify the function or even optimize it. Further, except in a very large volume commercial application, ASICs are considered too costly for many designs. FPGAs represent reconfigurable computing technology. These (FPGAs) consist of logical blocks and some amount of Random Access Memory (RAM), all of which are wired by a vast array of interconnects. All logic in FPGA can be rewired, or reconfigured with different purposes as many times as a designer likes. Thus, considering availability, cost and design cycle these were chosen for the implementation [36].

Chapter 3

Proposed Weighted Logarithmic Model for Enhancement of Fog Degraded Digital Images

This chapter includes the background and contrast measures in section 3.1, while section 3.2 includes the proposed model and a proposed contrast measure. Section 3.3 includes the computational complexity and illustrates the resource efficiency.

3.1 Background

In this section the initial motivation of the Logarithmic Image Processing (LIP) model and a review of contrast measures is included.

3.1.1 Logarithmic Image Processing (LIP)

In the LIP framework, the images are represented by mappings, called grey tone functions (f) [25] [26] [33] that are defined on the spatial domain and valued in the positive real number set $[0, M)$, called the grey tone range. The transmittance of f at point (x, y) is given by [25] [26] [33]:

$$N_f(x,y) = \frac{\xi_s(x,y)}{\xi_e(x,y)} \tag{23}$$

Where, $\xi_s(x, y)$ is the incoming flux,

$\xi_e(x, y)$ is the outgoing flux,

In this perspective, the grey tone function f is defined by [25] [26] [33]:

$$f(x,y) = M(1 - N_f(x,y)) \tag{24}$$

Eq. (23) and (24) illustrates the physical rationale and its consistency with the transmittance image formation model. The linear space constituted by the set of these grey tone functions ordered with a vector addition denoted $\oplus$ and a scalar multiplication, denoted $\otimes$ are defined in [25] [33]. A mathematical meaning to the opposite and difference between two grey tone functions f and g is given [23] [32] by:

$$\Theta f = \frac{-Mf}{M - f} \tag{25}$$

$$f \ \Theta \ g = M \frac{f - g}{M - g} \tag{26}$$

3.1.2 Contrast Measure

A light that is observed by human eye may be expressed in differential form i.e. either as slightly brighter or much brighter than another light, but it is tough to allocate numerical values to such observations [33]. It is however, expected to evaluate a contrast measure indirectly in terms of the minimum change in illumination which can be distinguished as a change in brightness.

If L is the uniform background luminance observed by a human eye, and ΔL is the increase or decrease in that luminance, then the measure of the contrast defined [27] [33] by:

$$C_w = \frac{\Delta L}{L} \tag{27}$$

is considered a measure of the perceptive power of the eye. This description of the relation between the discriminable threshold ΔL and the original luminance L is known as the Weber-Fechner law.

For simple patterns, the Michelson contrast measure [28] [33] is used to measure the contrast of a periodic pattern such as a sinusoidal grating and is defined as:

$$C_M = \frac{L_{\max} - L_{\min}}{L_{\max} + L_{\min}} \tag{28}$$

Eqs. (29) and (30) depicts the variability and deviation from a common ground. Fixed measurement of contrast using Eq. (30) is not appropriate because a pair of points of extreme brightness or darkness can determine the contrast of the whole image. For example, if a single over illuminated point or an especially under illuminated point is added to an average contrast image, the value of the Michelson contrast would increase significantly, but the apparent contrast may be reduced [27] [33].

The definition of a local band limited contrast in the frequency domain defined in [27] [33] provides a local contrast measure for every band that depends not only on the local energy at that band but also on the local background luminance as it varies from place to place in the image:

$$C(x, y) = \frac{a(x, y)}{l(x, y)} \tag{29}$$

Where, $a(x, y)$ - Filtered image

$l(x, y)$ - Luminance mean image.

Eq. (29) is applicable to complex images and finds the contrast in the frequency domain. Weber's law based contrast measure is defined in [31] [33], for an image I , divided into $k_1 \times k_2$ blocks with center (k, l) of size $M_1 \times M_2$:

$$EME_{k_1,k_2}(\Phi) = \frac{1}{k_1 k_2} \sum_{l=1}^{k1} \sum_{k=1}^{k2} 20 \ln \frac{I^w_{\max;k,l}(\Phi, par)}{I^w_{\min;k,l}(\Phi, par) + c} \tag{30}$$

where, Φ is a given transform, $I^{w}_{\max;k,l}$, $I^{w}_{\min;k,l}$ are the maximum and minimum luminance values in a block of the image, and c is a small constant equal to 0.0001 to avoid dividing by 0. This measure of enhancement is used to find the average ratio of maximum to minimum intensities in decibels. Another method of enhancement measure defined is based upon the concept of entropy [31] [33]

$$EMEE_{k_1,k_2}(\Phi) = \frac{1}{k_1 k_2}\sum_{l=1}^{k1}\sum_{k=1}^{k2}\mu\left(\frac{I^{w}_{\max;k,l}(\Phi, par)}{I^{w}_{\min;k,l}(\Phi, par)+c}\right)\times \ln\frac{I^{w}_{\max;k,l}(\Phi, par)}{I^{w}_{\min;k,l}(\Phi, par)+c} \tag{31}$$

This is known as the measure of enhancement by entropy, or EME using entropy. The measures that are based on the Michelson contrast (Eq. (28)) are AME and AMEE defined in [31] [33]. These gives the relationship between the spread and the sum of the two luminance values found in a small block.

$$AME = \left(\frac{1}{k_1 k_2}\sum_{l=1}^{k_1}\sum_{k=1}^{k_2} 20\ln\frac{I^{w}_{\max;k,l} - I^{w}_{\min;k,l}}{I^{w}_{\max;k,l} + I^{w}_{\min;k,l} + c}\right) \tag{32}$$

$$AMEE = \frac{1}{k_1 k_2}\sum_{l=1}^{k_1}\sum_{k=1}^{k_2}\mu\left[\frac{I^{w}_{\max;k,l} - I^{w}_{\min;k,l}}{I^{w}_{\max;k,l} + I^{w}_{\min;k,l} + c}\right]^{\mu}\times\ln\left[\frac{I^{w}_{\max;k,l} - I^{w}_{\min;k,l}}{I^{w}_{\max;k,l} + I^{w}_{\min;k,l} + c}\right]^{\mu} \tag{33}$$

Next section describes the proposed method and a region based logarithmic contrast measure (LRCM) for finding the optimal parameters of the proposed method.

3.2 Proposed Weighted Logarithmic Model for Enhancement of Fog Degraded Images

The following approach pertains at the outset to images obtained in the perspective of transmittance image formation LIP model:

Let G be a set of weather degraded images [33]:

$$G = \{D_1, D_2, ...D_n\} \tag{34}$$

Where D_n, . Weather degraded images/frame as captured from the silicon sensor based digital camera [30] at a time instant t and location l as depicted in Fig. 7 [33].

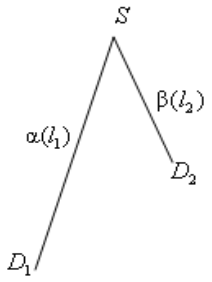

Fig. 7 Illustration of location parameters and capture points of the degraded images (D_1, D_2) with respect to a scene point (S).

The sensitivity curve for human and silicon sensors as shown in Fig. 8 [30] [33] evidently depicts a very low strength of silicon sensors sensitivity [30] [33] in the human visual range as compared to human sensitivity, whereas beyond the range of human sensitivity, silicon sensitivity has significant strength.

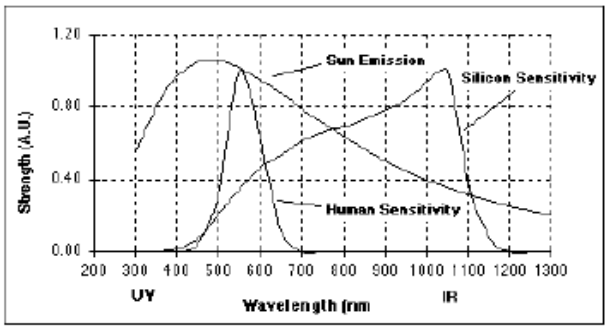

Fig. 8 Sensitivity Curve

We attempt to define a spatial domain transformation function (T) as a function of grey tones of degraded images and their respective location parameters to enhance and increase the information content of the weather degraded image captured from a silicon sensor based digital camera. This corresponds to the findings that the transmittance of a

scene point gets modulated and it increases with increase in distance [7] [31] [33]. T is defined as in [33]:

$$T = F\left\{\alpha(l_1), \beta(l_2), D_n\right\} \tag{35}$$

For a set of two images and location parameters $\alpha(l_1)$ and $\beta(l_2)$ using both the conventional operators $+, \times$ and LIP primitives $\oplus, \otimes$, T_s and T_L are defined as [33]:

$$D_s = T_s\left\{(\alpha(l_1), \beta(l_2), D_1, D_2)\right\} = \alpha(l_1) \times D_1 + \beta(l_2) \times D_2 - \alpha(l_1)\beta(l_2) \times \frac{D_1 D_2}{M} \tag{36}$$

$$D_L = T_L\left\{(\alpha(l_1), \beta(l_2), D_1, D_2)\right\} = \alpha(l_1) \otimes D_1 + \beta(l_2) \otimes D_2 - \alpha(l_1)\beta(l_2) \otimes \frac{D_1 D_2}{M} \tag{37}$$

Where, D_s and D_L are spatial domain transform images having distance information of the grey tone functions of both D_1 and D_2.

The resultant enhanced images $E_{s,D1}$, $E_{L,D1}$ with respect to D_s and D_L is obtained by spatially transforming the degraded image D_1 (corresponding to location l_1) using [33]:

$$E_{s,D1} = T_s\left\{(D_s, D_1)\right\} \tag{38}$$

$$E_{L,D1} = T_L\left\{(D_L, D_1)\ \right\} \tag{39}$$

Fig. 9(a) [33] shows the block diagram of the proposed method.

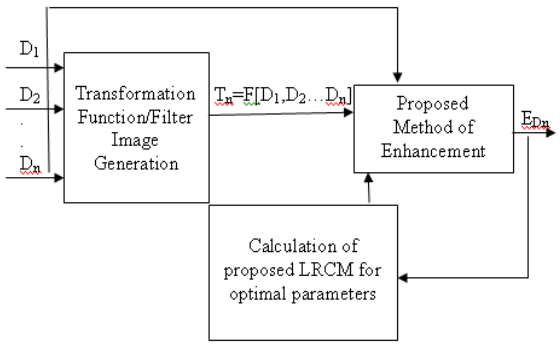

Fig. 9(a) Block Diagram of the Proposed Model [33].

3.2.1 Logarithmic Region Contrast Measure (LRCM)

For finding the optimal location parameters $\alpha(l_1)$ and $\beta(l_2)$ a region based logarithmic contrast measure (LRCM) is presented [33]. The defined measure is comprised of logarithmic subtraction and summation. It computes the contrast measure for a smallest discrete region (spatial domain) within the image, as compared to previously defined measures that calculate the same for each block of a divided image. The presented measure does not posses the disadvantage of range dependence while the contrast measures defined in Eqs. (25)-(28) are range dependent that change itself based on the maximum and minimum range [27] [33].

$$\text{LRCM} = 20\ln\left\{\sum_m\sum_n\left(\frac{I(m,n)\Theta}{\frac{1}{4}\oplus\sum_{i,j=0}^{1}I(m\pm i,n\pm j)}\right)\right\} \tag{40}$$

3.3 Computational Complexity Analysis and Illustration of its Resource Efficient Single Stage Pipeline Architecture.

The evident implementation details of each conventional image enhancement method are describes in chapter 6. Here, in this section, we provide a computational analysis of our proposed method [34]. The proposed model calculates the spatial domain transformation function that computes one addition, one subtraction, two multiplications, one division and three LIP multiplications for each grey tone as shown in fig. 9(b) which in turn depicts Eq. 37 of which the resource utilization summary is presented in Table 2. The feedback in fig.9(b) depicts Eq. 39. The order of finding the transformation function is $O(n)$. Similarly, the order of obtaining the enhanced image is also $O(n)$. Thus, the complexity for the overall method for a set of two degraded images is found to be $O(n)$ [32].

Table 2
Resource Utilization Summary

Resource	Utilization	Available	Utilization %
LUT	75	53200	0.14
FF	50	106400	0.05
IO	23	200	11.5
BUFG	1	32	3.13

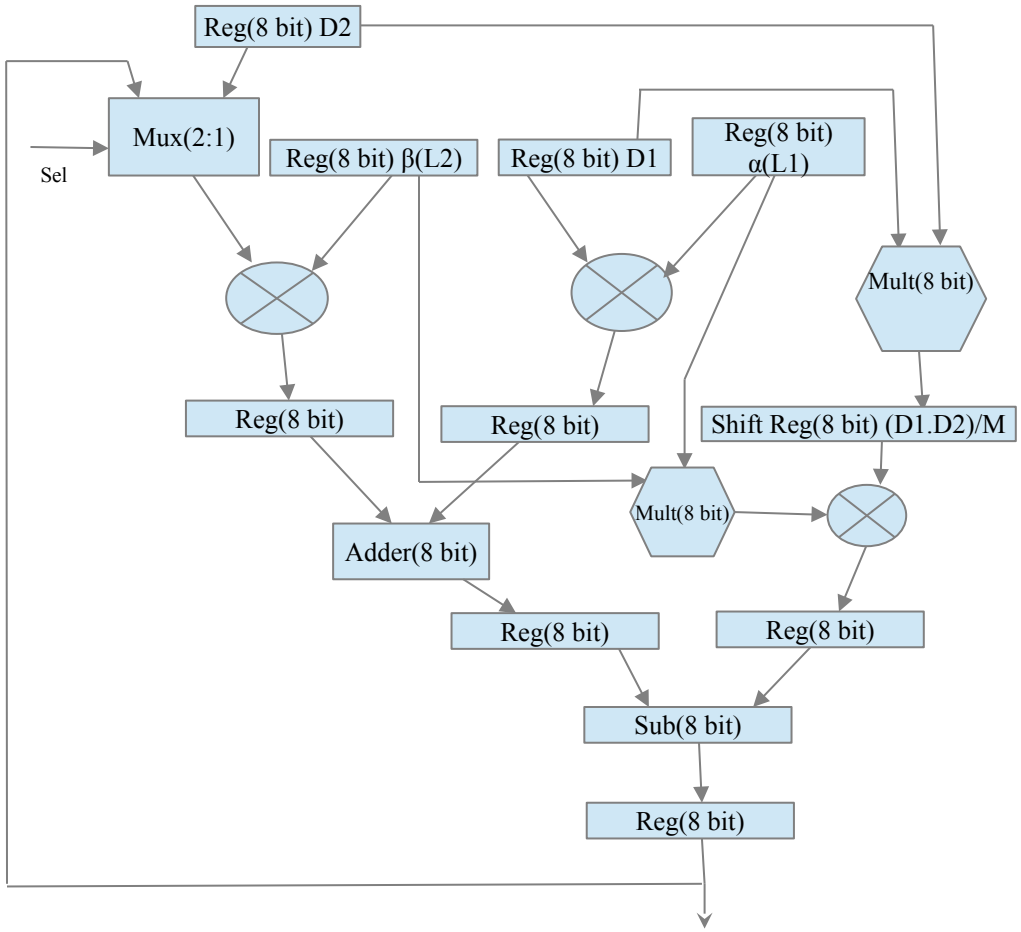

Fig. 9(b) Architecture of the Proposed Weighted Logarithmic Model

3.4. Simulation Results, Comparison of the Proposed Weighted Logarithmic Model and Comparison of the Proposed Contrast Measure

In this section, we present the simulation results of the proposed image enhancement method onto two sets of experimental image data of on road weather degraded images (Distant Vehicle and Letter Board). We compare the results of the proposed method using the basic LIP model, method using conventional multiplicative parameters and the result of the method using logarithmic multiplicative parameters. We also compare the enhancement results of the proposed method with the result of histogram equalization.

For finding the optimum parameters; we use the presented measure LRCM and compare the same with those found using AMEE. Fig. 10 and Fig. 11 [33] shows the results for two sets of experimental data of on road weather degraded images and their LRCM values. Table 3-4 [33] compares the values of the contrast measures while increasing the location parameter $\alpha(l_1)$ for image data set of distant vehicle and letter board.

Table 3
Comparison of measures for increasing $\alpha(l_1)$ and $\beta(l_2) > 1$
Distant vehicle image data set

Distant Vehicle					
Alpha	**AME**	**AMEE**	**EME**	**EMEE**	**LRCM**
0.2	0.1057	0.1435	0.2089	10.5041	10.2748
0.3	0.1064	0.1478	0.209	10.5491	10.8162
0.4	0.1017	0.1562	0.2092	10.5691	10.8383
0.5	0.1101	0.1718	0.2095	10.6038	10.7129
0.6	0.1124	0.1886	0.2098	10.6463	10.8212
0.7	0.1147	0.2069	0.2101	10.6996	11.0472

It evidently indicates that measure value increases with increase in $\alpha(l_1)$ (corresponding to degraded image D_1). Tables 5-6 [33] compares the values of the measures while decreasing the location parameter $\beta(l_2)$ (corresponding to degraded image D_2) for distant vehicle and letter board.

The values shown in Table 5 and 6 [33] indicate a decrease in measure values with decrease in the value of location parameter $\beta(l_2)$.

Table 4
Comparison of measures for increasing $\alpha(l_1)$ and $\beta(l_2) > 1$
Letter board image data set

Letter Board					
Alpha	**AME**	**AMEE**	**EME**	**EMEE**	**LRCM**
0.2	0.0946	0.0909	0.208	6.9267	10.7181
0.3	0.0976	0.1032	0.2082	6.9795	10.7668
0.4	0.1012	0.1196	0.2085	7.0484	10.8848
0.5	0.1043	0.1359	0.2088	7.1165	11.0242
0.6	0.1072	0.1529	0.2091	7.189	11.2057
0.7	0.1097	0.1691	0.2094	7.2665	11.2055

Table 5
Comparison of measures for decreasing $\beta(l_2)$ and $\alpha(l_1) < 1$
Distant vehicle image data set

Distant Vehicle					
Beta	**AME**	**AMEE**	**EME**	**EMEE**	**LRCM**
1.5	0.1147	0.2069	0.2101	10.7023	11.0472
1.4	0.1133	0.1954	0.2099	10.6703	10.9047
1.3	0.112	0.1855	0.2097	10.6388	10.8632
1.2	0.1102	0.1724	0.2095	10.6125	10.8006
1.1	0.1086	0.1617	0.2093	10.587	10.5732
1	0.1071	0.1522	0.2091	10.5639	10.3789

Fig. 12(b) and 12(c) [33] shows the results of enhancement of distant vehicle image data set with certain randomly chosen parameter values and with optimal parameter values respectively.

Table 6
Comparison of measures for decreasing $\beta(l_2)$ and $\alpha(l_1) < 1$
Letter board image data set

Letter Board					
Beta	**AME**	**AMEE**	**EME**	**EMEE**	**LRCM**
1.5	0.1097	0.1691	0.2094	7.2665	11.2055
1.4	0.1091	0.1652	0.2093	7.2458	11.2553
1.3	0.1082	0.159	0.2092	7.2158	11.2425
1.2	0.1072	0.1526	0.2091	7.1875	11.0915
1.1	0.1057	0.1439	0.2089	7.15	10.9561
1	0.1049	0.1392	0.2088	7.1303	10.8452

It is clearly evident that the image enhanced with the optimal parameters is visually better than the other. Fig. 13(b) and Fig. 13(c) [33] show the results of letter board data set with similar outcome. Fig. 12(d), Fig. 13(d) [33] shows the plot between LRCM and parameters for the purpose of choosing an optimal value as their local maxima. The optimal values are then compared with the values obtained from the plot between AMEE and parameters; Fig. 12(e), Fig. 13(f). Fig. 13(e) [33] shows the result of the proposed enhancement method with the parameters found as the local maxima of Fig. 13(f) [33]. It is thus illustrated that we obtained similar optimal values for the distant vehicle data set when using both LRCM as well as AMEE measure, while the values found from both the measures differ for the letter board data set.

The original degraded images in Fig. 10(a), (e) and Fig. 11(a), (e) [33] are images that are captured by a conventional silicon sensor camera (Sony DSC-W210) [33].

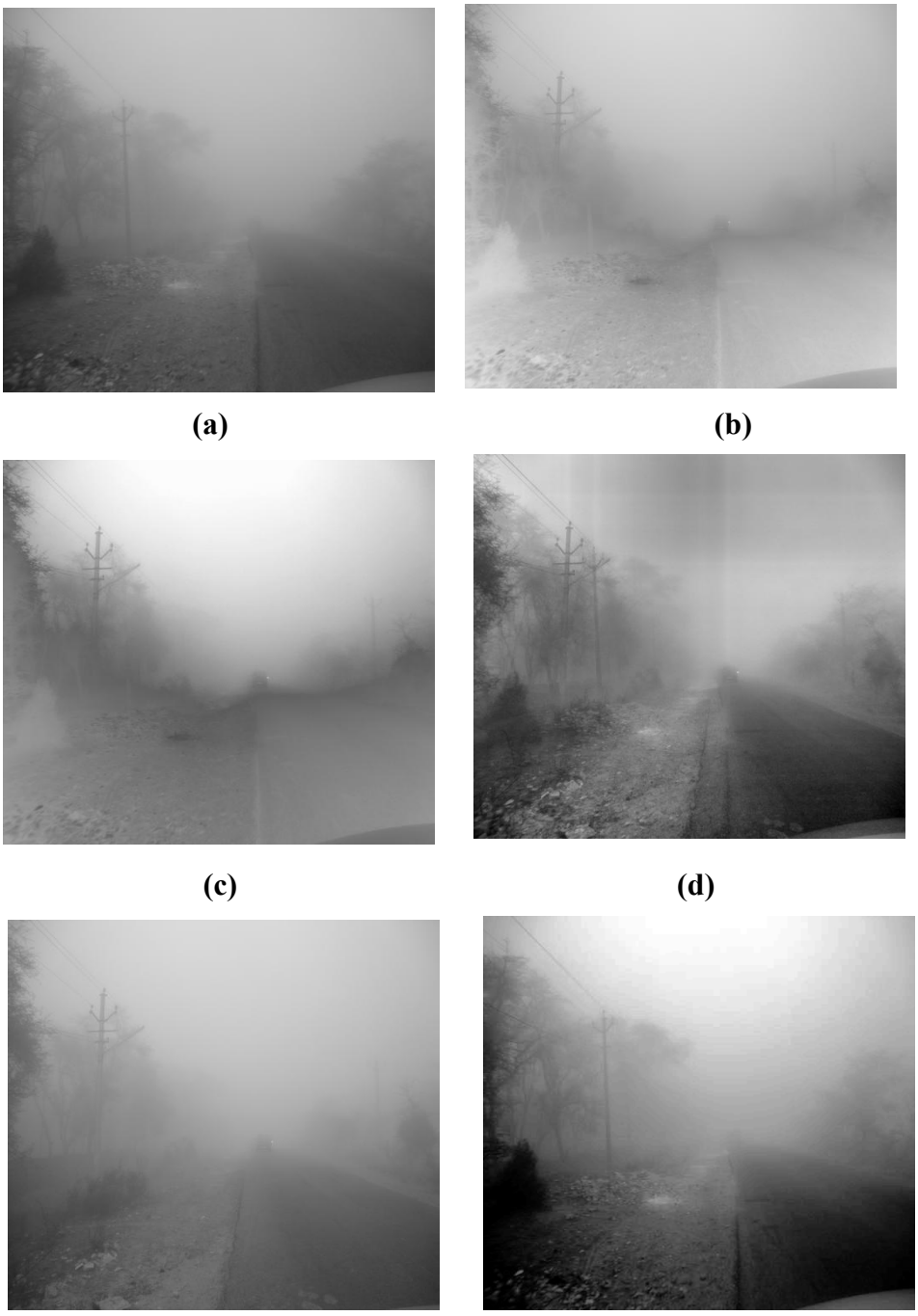

(a) **(b)**

(c) **(d)**

(e) **(f)**

Fig 10. (a) Degraded Image D1 (LRCM=10.6295) (b) Result of method using basic LIP model (LRCM=9.6831) (c) Result of method using conventional multiplicative parameters (LRCM=10.9504) (d) Result of method using optimal logarithmic multiplicative parameters (LRCM=11.0153) (e) Degraded Image D2 (LRCM=10.6536) (f) Result of Histogram Equalization (LRCM=11.0074)[33]

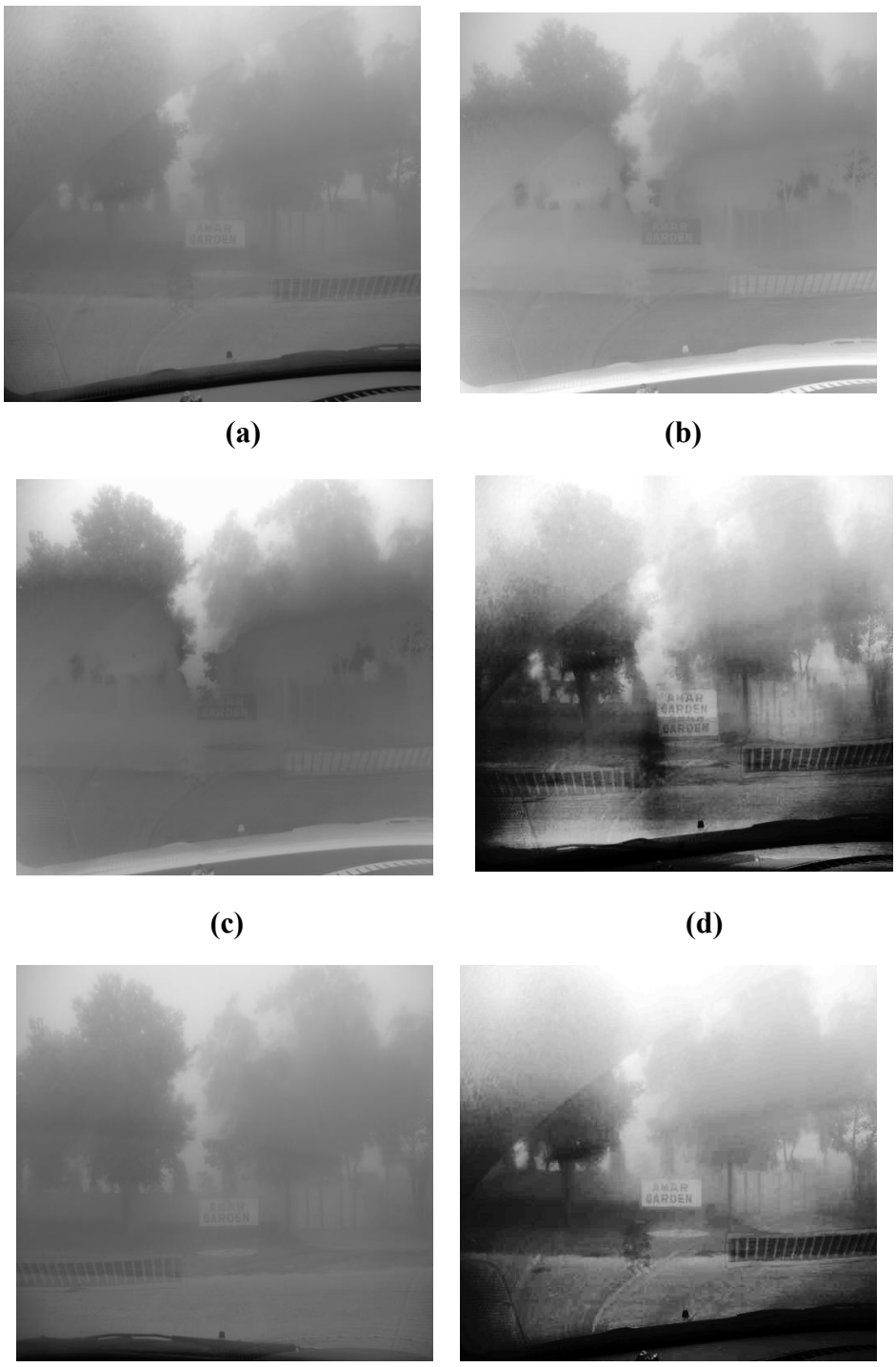

Fig 11. (a) Degraded Image D1 (LRCM=10.9512) (b) Result of method using basic LIP model (LRCM=10.8415) (c) Result of method using conventional multiplicative enhancement parameters (LRCM=11.4146) (d) Result of method using optimal logarithmic multiplicative location enhancement parameters (LRCM=11.5099) (e) Degraded Image D2 (LRCM=11.0056) (f) Result of Histogram Equalization (LRCM=11.5052)[33]

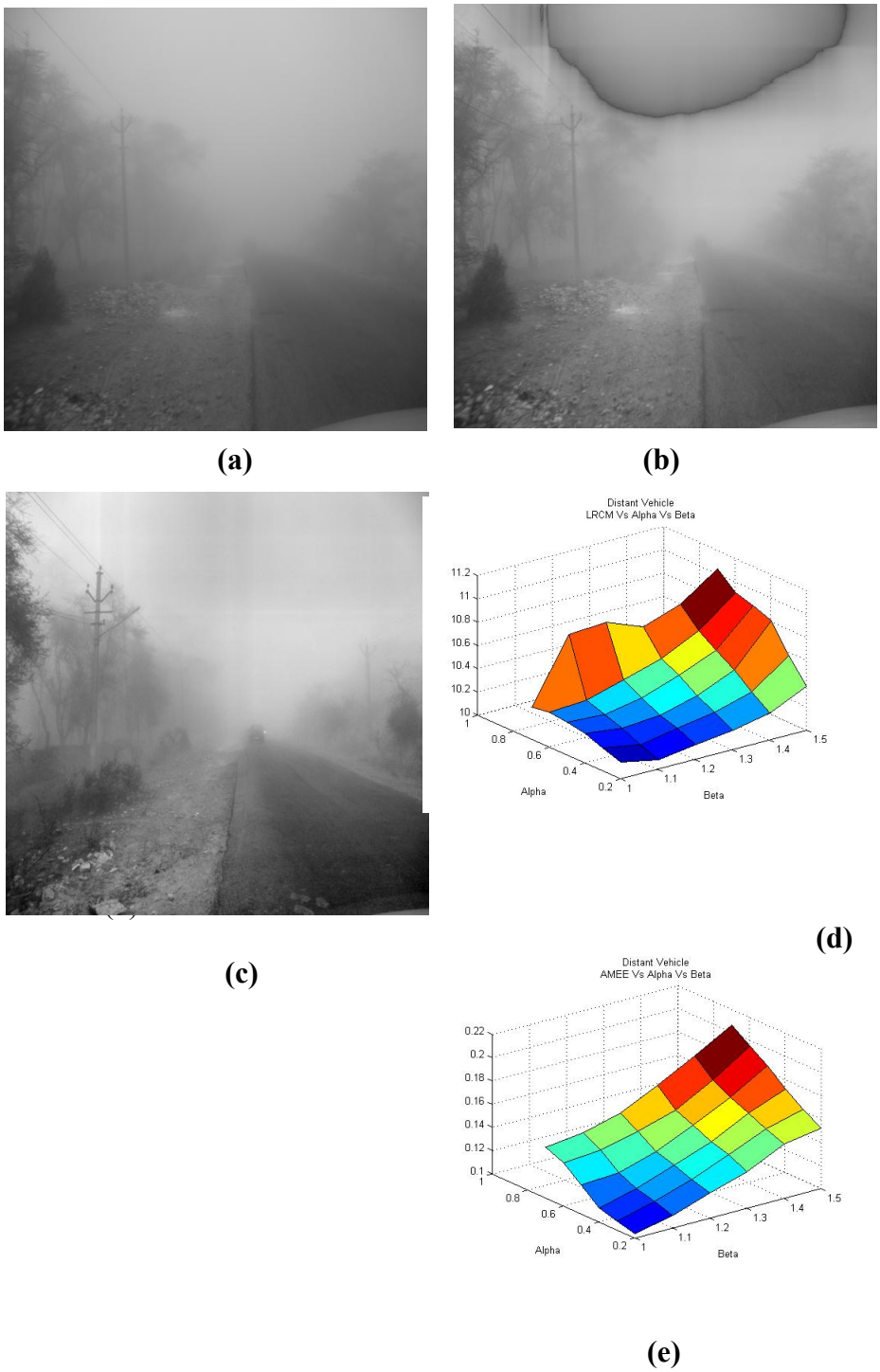

Fig 12. (a) Degraded Image D1 (LRCM=10.6295) (b) Result of enhancement with logarithmic location enhancement parameter $\alpha(l_1)$ =0.2, $\beta(l_2)$ =1.5 (LRCM=10.2748) (c) Result of enhancement with optimal logarithmic location enhancement parameter $\alpha(l_1)$ =0.7, $\beta(l_2)$ =1.5 (LRCM=11.0153) chosen from local maxima of LRCM Vs Alpha Vs Beta (d) LRCM Vs Alpha Vs Beta (e) AMEE Vs Alpha Vs Beta[33]

(a)

(b)

(c)

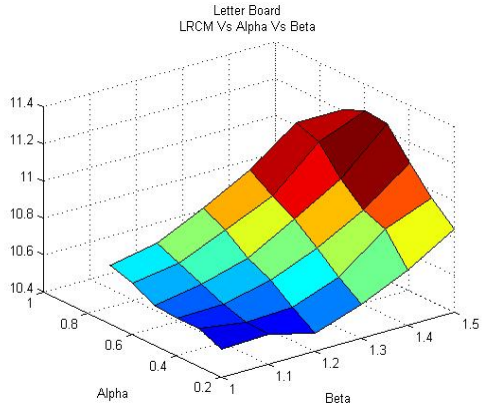

(d)

(e)

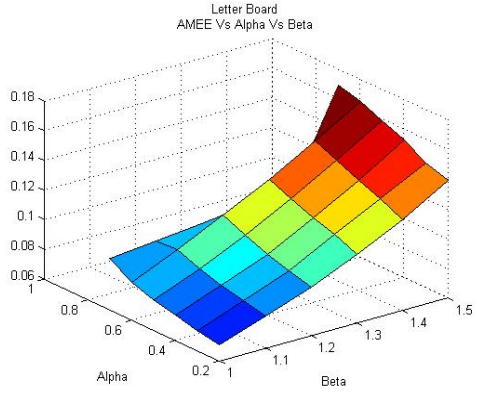

(f)

Fig 13. (a) Degraded Image D1 (LRCM=10.9512) (b) Result of enhancement with logarithmic location enhancement parameter $\alpha(l_1)$ =0.3, $\beta(l_2)$ =1.5 (LRCM=10.7668) (c) Result of enhancement with optimal logarithmic location enhancement parameter $\alpha(l_1)$ =0.6, $\beta(l_2)$ =1.4 (LRCM=11.2553) chosen from local maxima of LRCM Vs Alpha Vs Beta (d) LRCM Vs Alpha Vs Beta (e) Result of enhancement with location enhancement parameter $\alpha(l_1)$ =0.7, $\beta(l_2)$ =1.5 (=11.2055) chosen from local maxima of AMEE Vs Alpha Vs Beta (f) AMEE Vs Alpha Vs Beta[33]

Fig. 15 shows the result for HVD Based enhancement method. It is clearly visible from Figs. 15a-f that as we increase the value of α the low frequency components move towards the brighter side while reducing the overall contrast and thereby improving the visibility of low frequency components which was obtained after removing the high frequency components. Response of HVD with different levels of decomposition (2,3,4 and 5) was also carried out, and the result was found to be similar as in Fig 15f . It is also illustrated from Table 7 that as we increase the value of α the overall information content reduces which commensurate with the fact that we have removed the high frequency components from the fog degraded image and then applying a factor on the remaining low frequency components of the image which in turn depicts the low energy components. AWE is the measure of enhancement based on Weber's law with entropy while EWE is the measure of enhancement based on Weber's law without entropy.

Table 7. Contrast Measure based on Weber's law and Entropy with increasing value of parameter α.

Outdoor Scene		
α	**AWE**	**EWE**
1.1	10.8033	0.2131
1.2	10.7870	0.2126
1.3	10.7461	0.2118
1.4	10.6968	0.2110
1.5	10.6406	0.2103

3.5. HVD based Enhancement of Fog Degraded Digital Images

In the proposed Hilbert Vibration Decomposition (HVD) based image enhancement algorithm of fog degraded image as shown in Fig. 14, the degraded image D is converted into a column vector D_C. The column vector D_C is then decomposed using discreet version of HVD, as given by Eq. (41).

where A_{Dm} is Instantaneous Amplitude (IA) and W_{Dm} is the Instantaneous Frequency (IF) of m^{th} element of D_C. The first, second and third element of the vector, i.e. W_{DC1} , W_{DC2} and W_{DC3} are obtained.

$$D_c(n) = \sum_{m=1}^{3} A_{D_m}(n) \cos\left(\sum_{m=1}^{3} W_{D_m}(n)\right) \tag{41}$$

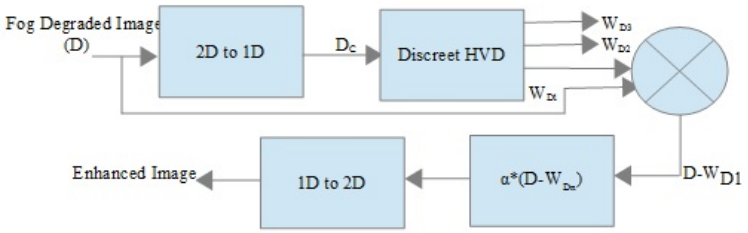

Fig. 14 Block diagram of the HVD based enhancement.

The Instantaneous Frequency (IF) components W_{D1} , W_{D2} and W_{D3} having first, second and third highest frequency element are converted into images, respectively. The image formed by W_{D1} vector corresponds to the highest frequency elements of the fog degraded image which give most of the spatial frequency information, while image formed by W_{D2} element is the second highest frequency element giving lower spatial frequency information of the fog degraded image as compared with first frequency element. We now include the factor to improve the remaining low frequency element which in turn improves the details while reducing the overall contrast or energy element

of the image. Further the above process is mathematically expressed by Eq. (42) and (43) given below:

$$E_1 = D - W_{D1} \tag{42}$$

The final enhanced image E_2 by the proposed method from E_1 (Low frequency components) is given by:

$$E_2 = \alpha\left(D - W_{D1}\right) \tag{43}$$

Fig. 15 [33]

a Fog degraded digital image
b Proposed Method with HVD(3 Components) & α=1.1
c Proposed Method with HVD(3 Components) & α=1.2
d Proposed Method with HVD(3 Components) & α=1.3
e Proposed Method with HVD(3 Components) & α=1.4
f Proposed Method with HVD(3 Components) & α=1.5

Chapter 4

Conventional Linear Image Enhancement Techniques Made Adaptive to Specific Medical Images and their Architectures

This chapter includes the description and simulation of conventional linear image enhancement techniques that are made adaptive to specific medical images. Further in its subsections single stage pipeline architectures of each algorithm is also included. In section 4.5 the proposed enhancement processor is included followed by illustration of the proposed enhancement processor embedded onto an existing medical image sensing system in section 4.6. Section 4.7 includes the result and comparison of individual techniques.

4.1 Adaptive Contrast Stretching Technique

The concept of contrast stretching comprises of the piecewise linear transformation. Generally, the low-contrast images are a result of poor illumination or lack of dynamic range in the imaging sensor. The basic idea behind this algorithm is to increase the dynamic range of the grey levels in the image being processed, that will in turn enhance the visibility of the image. Fig. 16 [1] [4] [34] [36] shows the nature of the transformation function. Here selection of the points (a_1, b_1) and (a_2, b_2) plays a crucial role in application of this algorithm, as they decide the degree of contrast enhancement. Here, u (Alpha in Fig. 18), v (Beta in Fig. 18) and w (Gamma in Fig. 18) are adaptive parameters that represents the slope of the linear function.

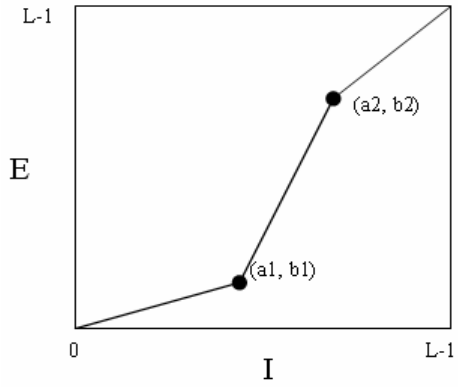

Fig. 16 Contrast stretching function [4][36]

Fig. 17 (a)-(b) [34] [36] shows the CT scan image of a liver and result of adaptive contrast stretching algorithm respectively. The shown results were obtained using the following parameter values [34] [36]: u=1.2, v=1.2, w=1.5, b_1=0.2, b_2=0.3, a_1=0.3, a_2=0.6. On visual inspection we can detect the position of tumor which is present in the CT scan image of a liver. These parameter values are made adaptive depending upon the degree of contrast enhancement required for specific medical images.

4.1.1 Simulation Results on CT Scan of a Liver

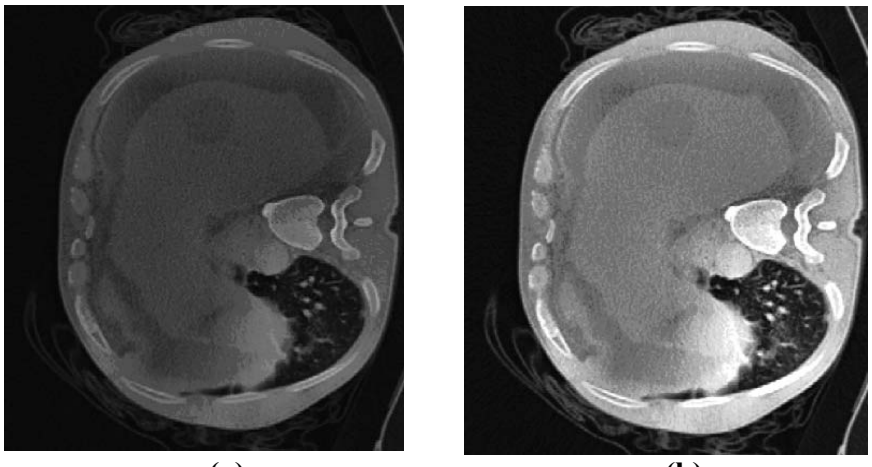

(a) **(b)**

Fig 17. (a) CT scan image of a liver (original image) (b) Enhanced image after applying contrast stretching technique [36]

4.1.2 Single Stage Pipeline Architecture of Adaptive Contrast Stretching Technique

The proposed architecture as shown in Fig. 18 depicts the adaptive contrast stretching algorithm. Initially the pixel that is stored in the input register is compared using an 8 bit comparator in order to find the range, in which the pixel lies. If the pixel lies between 0 and a_1, a_1 and a_2 and a_2 and L-1 then the outputs c_2, c_1 and c_0 of the comparator becomes high respectively. Output c_2, triggers the multiplication of input pixel with a constant u (8 bit). Further the outputs c_1 and c_0 of the comparator are connected as select lines of a 4:1 multiplexer in order to select the values of b_1 and b_2 that is to be subtracted from the input pixel I. c_1 and c_0 are also acting as select lines of another 4:1 multiplexer as shown in the figure that decides whether the input values of the multiplier will be v or w, which are constants stored in respective registers. The output of this multiplexer and that of the subtracter are then multiplied. This multiplier has two possible outputs i.e. $v*(I - a_1)$ and $w*(I - a_2)$. A 4:1 multiplexer is used here that selects the constants either b_1 or b_2 which is further added to the output of the above multiplier. We now obtain the output of the adder as either $(b_1 + w(I-a_1))$ or $(b_2 + v(I-a_2))$. Here, we connect a 2:1 multiplexer in order to select the final transformed output, which is either of the first multiplier (v*I) or of the adder. This final pixel value is then stored in the output register. Each pixel of the image is then transformed by this pipelined hardware [34] [35] [36].

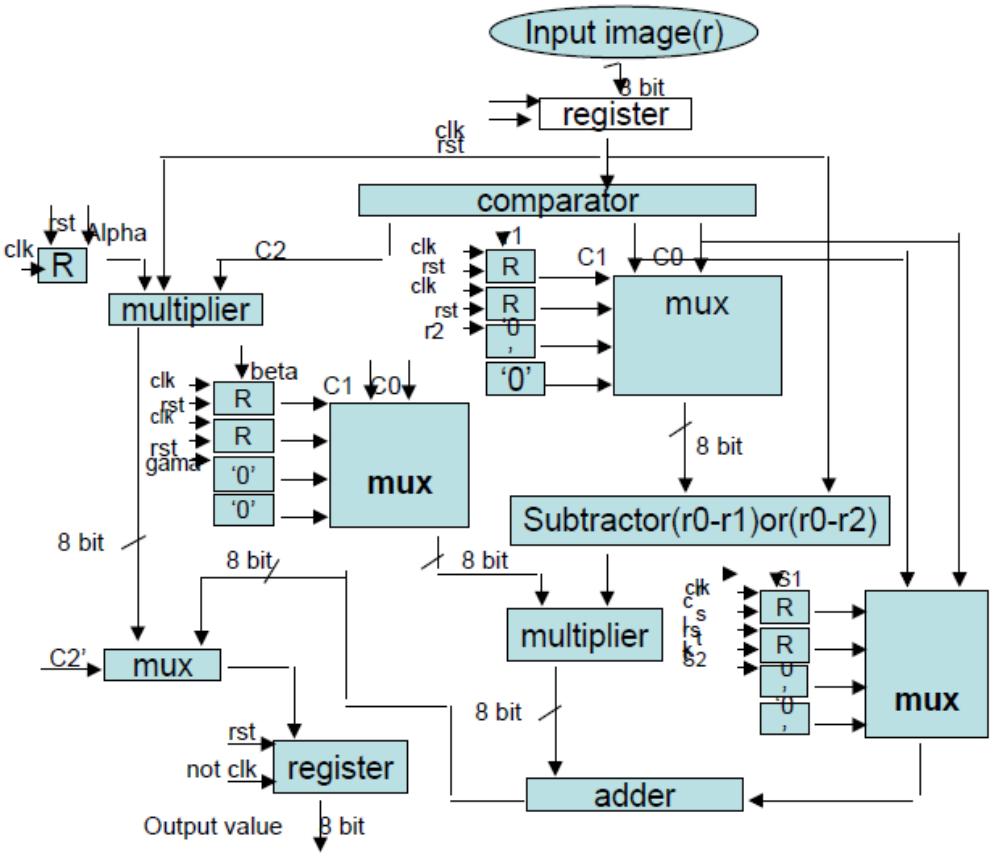

Fig 18. Single Stage Pipeline Architecture of Adaptive Contrast Stretching Technique [36]

4.2 Adaptive Image Negative Technique

The negative of an image with grey levels in the range between $[0, L-1]$ is obtained by using the transformation as shown in Fig. 18 [1] [4] [34] [36],

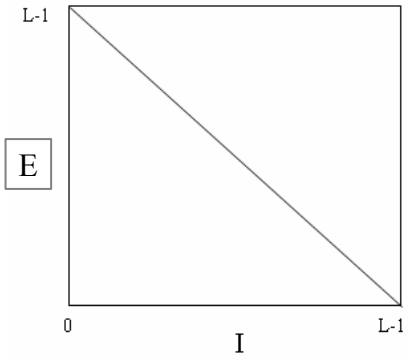

Fig. 19 Negative Function [4][36]

Here, grey level intensity of the white pixel (L) is specific to the image. It is made adaptive for inverting the intensity levels of an image to transform it into a photographic negative.

4.2.1 Simulation Results on Mammogram

Mammogram is a type of medical image where we require to find a region of microcalcification (typically white region). It represents presence of breast cancer, as shown in Fig. 20 (a)-(b) [1] [4] [34] [36].

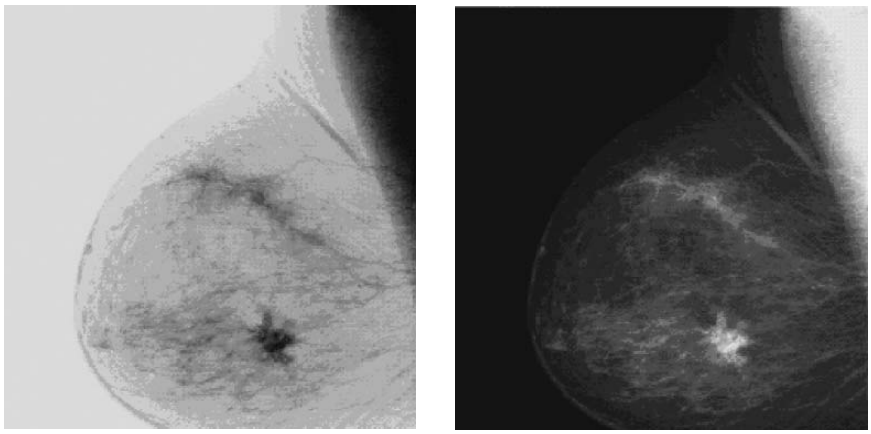

(a) **(b)**

Fig 20. (a) Mammogram Scan (original image) (b) Enhanced image after applying image negative technique [4][36]

4.2.2 Single Stage Pipeline Architecture of Adaptive Image Negative Technique

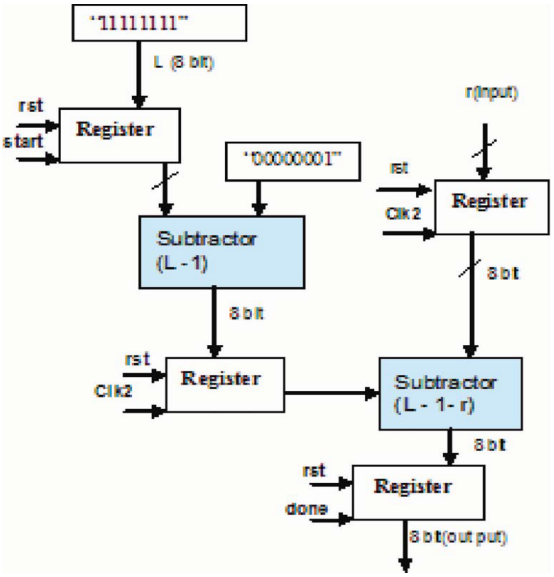

Fig. 21 Single Stage Pipeline Architecture of Adaptive Image Negative Technique [36]

Fig. 21 [34] [36] shows the architecture of image negative algorithm. Here, the input pixel value of an image is subtracted from the maximum grey value (L) less 1. The value of L, depending upon the input image is stored in the register from which "1" and input pixel I is further subtracted.

4.3 Logarithmic Transformation Technique

The general form of the log transformation enhancement is given by [1] [4] [34] [36],

$$E = C^{*}Log\left(1+I\right) \tag{44}$$

This transformation is made adaptive to the constant parameter (C=1.5) to map a narrow range of low grey level values in the input image into a wider range of output levels. The opposite is true for higher values of input levels. We would use a transformation of this type to expand the values of dark pixels in an image while compressing the higher-level

values. An important characteristic of this algorithm is that it compresses the dynamic range of images with large variations in pixel values.

4.3.1 Simulation Result on Fluorescein Angiography

After applying log transformation to the original image of fluorescein angiography of a retina as shown in Fig. 22(a). The dynamic range of the pixels in the image increases, which in turn increases the visibility of the hole as well as retinal nerves, as shown in Fig. 22(b) i.e. the enhanced image of fluorescein angiography.

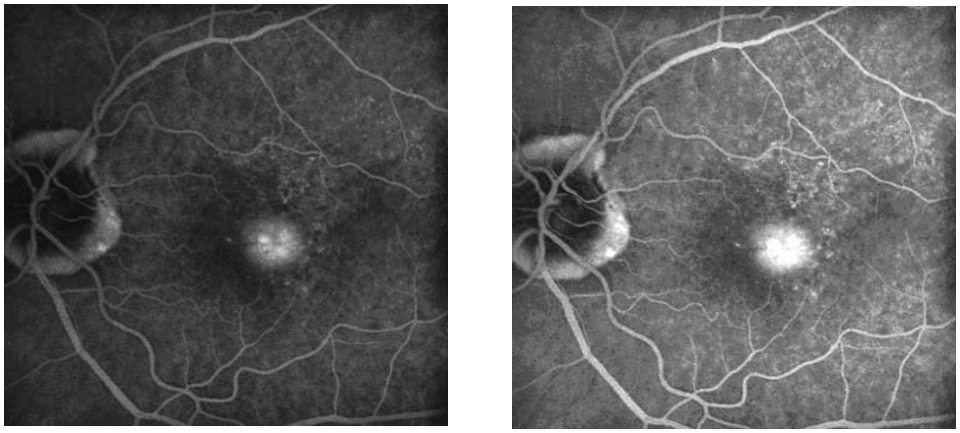

(a) **(b)**

Fig 22. (a) Fluorescein Angiography (original image) (b) Enhanced image after applying Logarithmic Transformation Technique [36]

4.3.2 Single Stage Pipeline Architecture of Logarithmic Transformation Technique

Fig. 23 shows the architecture of the log transformation, in which the input pixel of an image is initially stored in the register. We use an 8 bit adder that adds 1 to it. The next block evaluates the logarithmic of the adder output that is further multiplied by a constant C (8 bits), and final transformed pixel S (8 bit) is then stored in the output register.

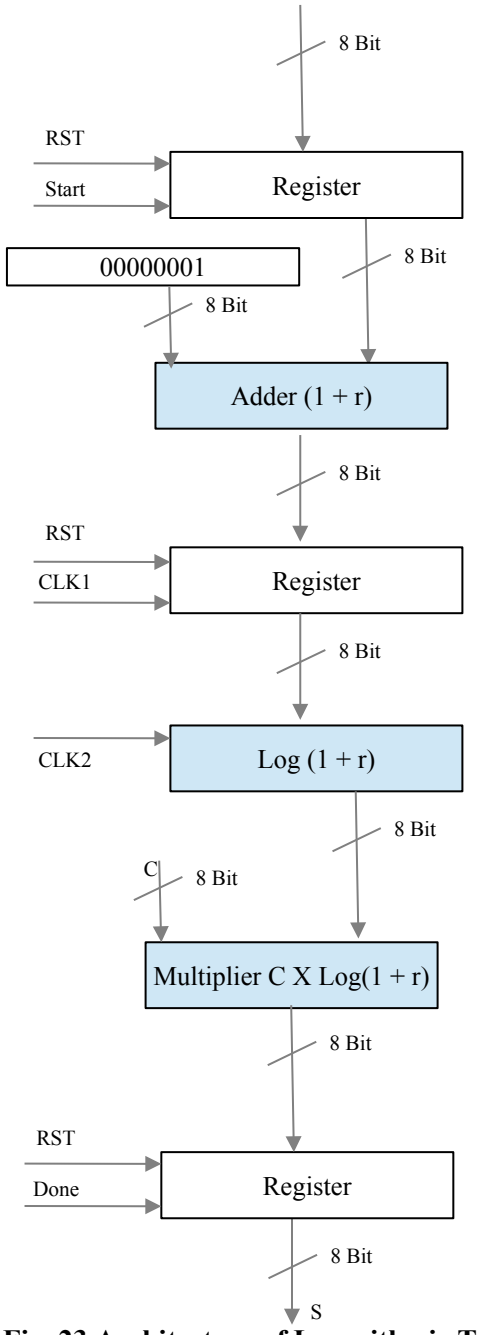

Fig. 23 Architecture of Logarithmic Transformation [36]

4.4 Histogram Equalization Technique

The histogram of a digital image with grey levels in the range [0, L-1] is a discrete function $h(r_k) = n_k$, where r_k is the k^{th} grey level and n_k is the number of pixels in the

image having grey level r_k. It is a common practice to normalize a histogram by dividing each of its values by the total number of pixels in the image, denoted by n. Thus, a normalized histogram is given by $P(r_k) = n_k/n$ for k = 0, 1… L-1, provides an estimate of the probability of occurrence of grey level r_k. Note that the sum of all components of a normalized histogram is equal to 1.

4.4.1 Simulation Result on CT Scan of Brain

The result of histogram equalization on a CT scan image (Fig. 24(a)) of brain is depicted in Fig. 24(b). It is observed that it improves the visibility and detect ability of the disease called obscuration of the lentiform nucleus, which is one of the early signs of acute cerebral artery infraction (ACAI), in CT brain images. In ACAI disease the blood goes through in our brain with very high speed, in this condition any vein in our brain can be damaged [37] [38]. This is shown in Fig. 23(a) by dark black spots, whereas Fig. 23(b) shows the enhanced image.

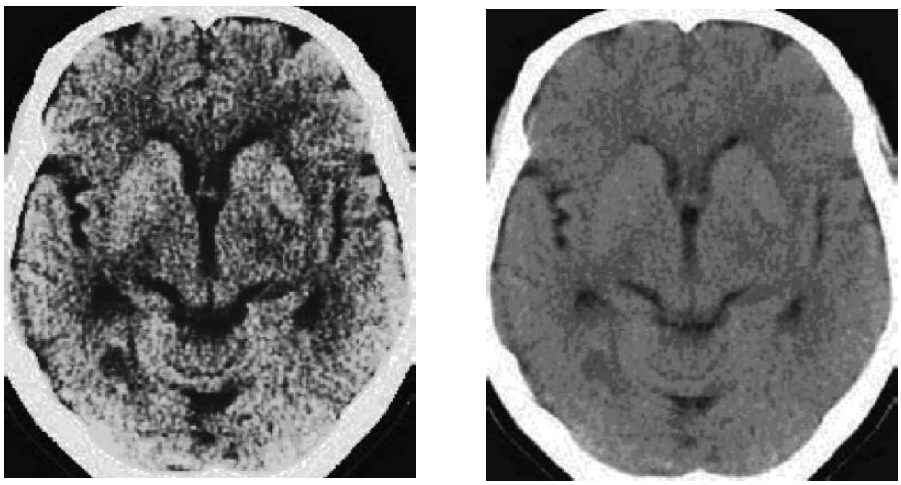

Fig 24. (a) CT Scan of Brain (original image) (b) Enhanced image after applying Histogram Equalization Technique [36]

4.4.2 Architecture of Histogram Equalization

Fig. 25 below shows the architecture of histogram equalization. There are 256 asynchronous counters [36] as a replacement to the 256 locations look up table RAM as described in [39]. Each counter is responsible for two tasks. The first task is to calculate the number of the occurrences of the pixel grey levels that range from 0 to 255. The second task is to simultaneously accumulate the current grey level statistics with the statistics of all pixels whose values are less than the current pixel value. The result of this accumulation process is the final value of the histogram equalisation. Since histogram equalisation calculation is performed during the phase of computing the histogram, this adds to saving the total time of computation.

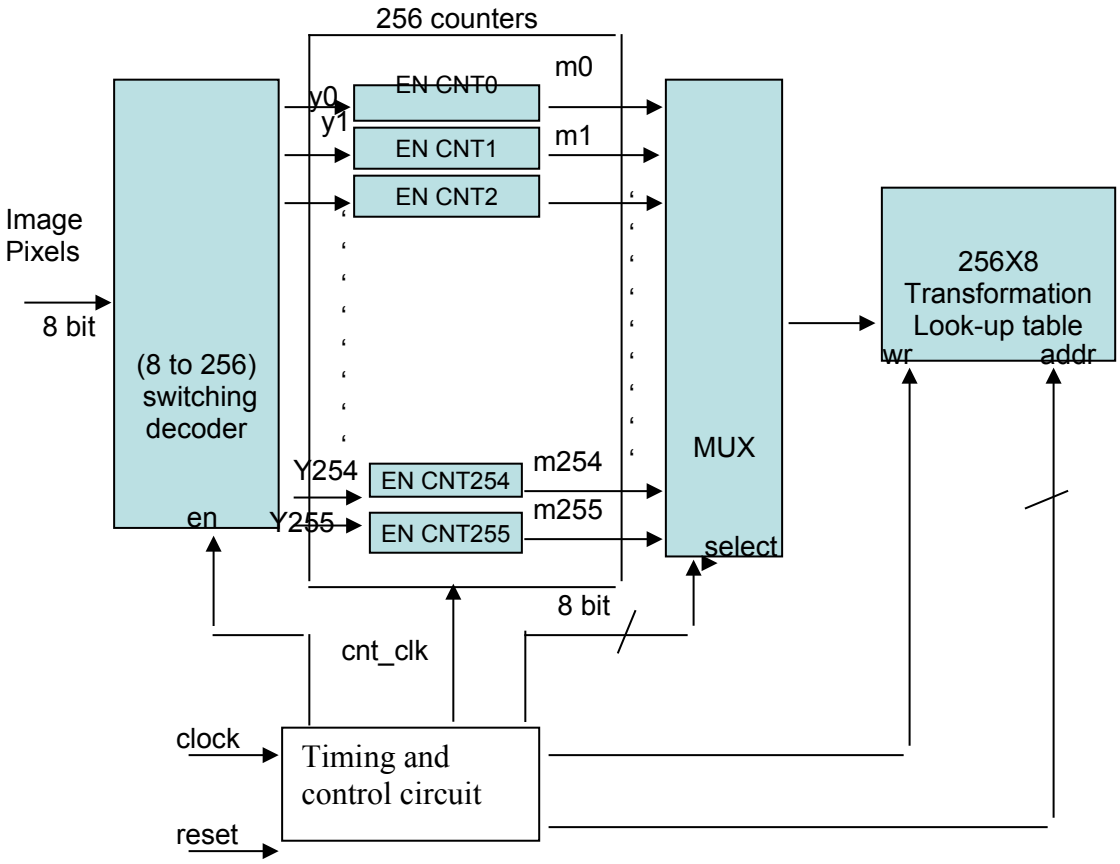

Fig. 25 Architecture of Histogram Equalization [36] [39]

4.4.2.1 Control FSM of Histogram Equalization

The Control FSM of histogram equalization is shown in Fig. 26. Here the architecture is pipelined at each stage to a total of 12 states. In State1 the input pixel value is loaded in an input register. In State2 and State3 the decoder is activated and it performs its function as described in the previous section. In State5 the decoder output enables the respective counter that is assigned to the current pixel. In State6 and State7 the counters are incremented and State8 is used to check whether all the input image pixels are processed, if not then this process is repeated for all pixels of the input image. In State9 multiplexer is enabled in order to select a location in the transformation look up table (memory). State10 is used to increment the select signal of the multiplexer by 1 from 0 to 255. In State11 the address of the look up table is incremented. This address is of the look up table at which the output of multiplexer (value of the histogram as output of counters) is stored. This address is then incremented by 1. In State12 it is checked whether all pixels of the transformed image have been read out: If yes, then completion of the process is indicated through a signal else the address is further incremented.

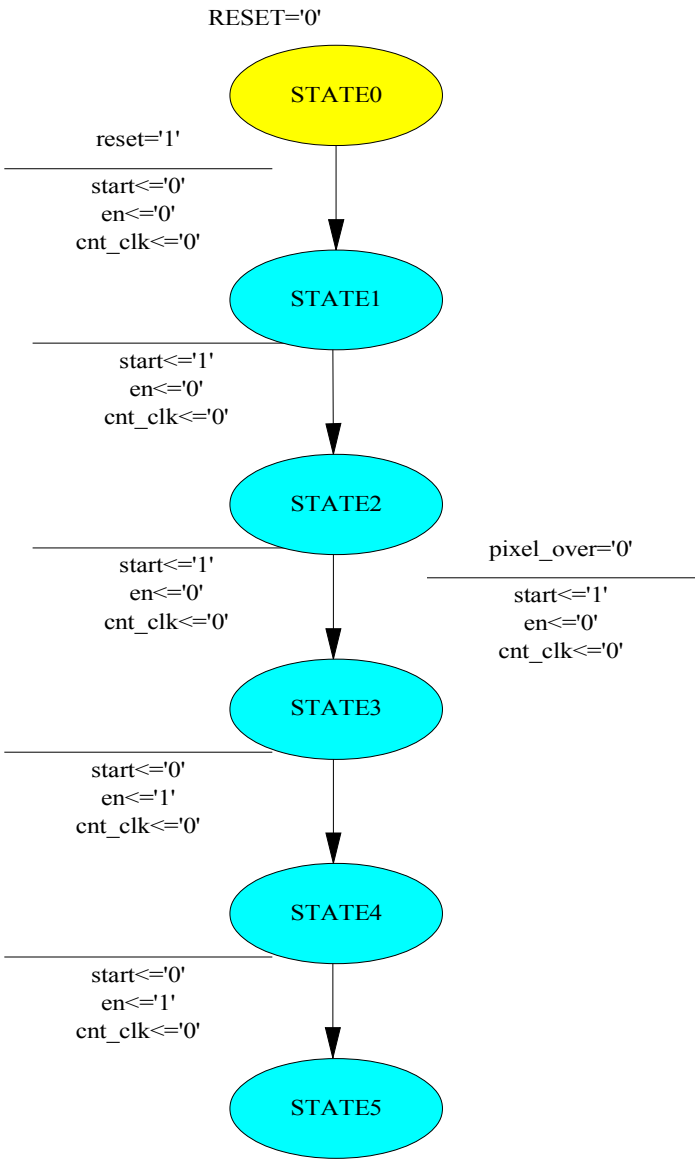
RESET='0'
STATE0
reset='1'
start<='0'
en<='0'
cnt_clk<='0'
STATE1
start<='1'
en<='0'
cnt_clk<='0'
STATE2
start<='1'
en<='0'
cnt_clk<='0'
pixel_over='0'
start<='1'
en<='0'
cnt_clk<='0'
STATE3
start<='0'
en<='1'
cnt_clk<='0'
STATE4
start<='0'
en<='1'
cnt_clk<='0'
STATE5

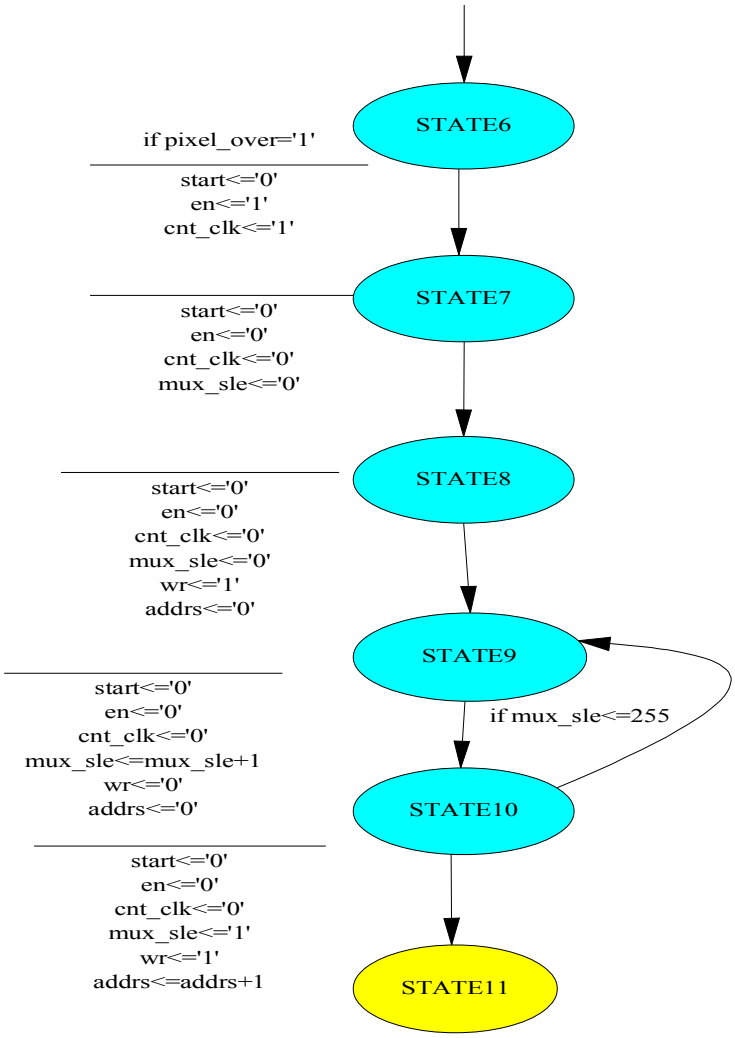

Fig. 26 Control FSM[36]

4.5 Proposed Enhancement Processor with Resource and Delay Optimization

Fig. 27 [36] shows the proposed combined architecture of all the three enhancement algorithms, Image negative, log ratio and contrast stretching. It can choose any one algorithm out of the three mentioned on the basis of the select0-select1 bus. The proposed architecture is highly optimized in space as depicted by Table 8; the number of subtractor is reduced to 25% of what could be utilized in individual architectures. Also

there is a 50% reduction in the multipliers which makes the processor highly optimized in terms of resource and pipeline results in delay optimisation.

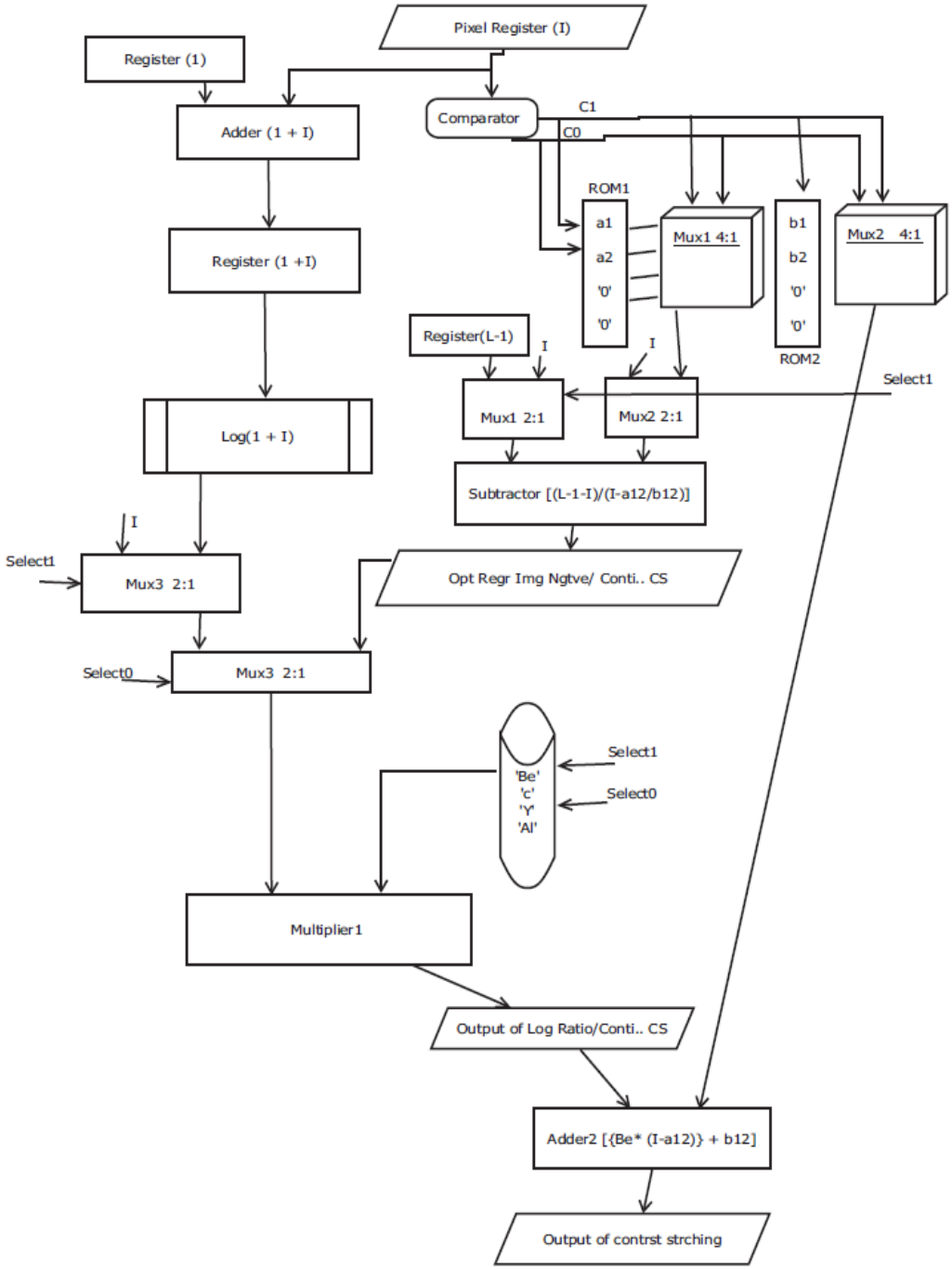

Fig. 27 Architecture of the Proposed Enhancement Processor with Resource and Delay Optimization [36]

Table 8. Illustration of Resource Optimization

Architectures	Subtractor	Multiplier	Adder
Contrast Stretching	1	2	1
Image Negative	2	0	0
Log Ratio	1	0	1
Total	**4**	**2**	**2**
Processor	**1**	**1**	**2**

4.6 Proposed Enhancement Processor Embedded onto an existing Medical Image Sensing System

An additional feature that increases the versatility of the proposed processor such that it can be embedded onto an existing medical image processing system as shown in Fig. 28 [36], is its added ability to select any one enhancement process out of the many (in this case three) on the fly that is during the operation of the image processing system.

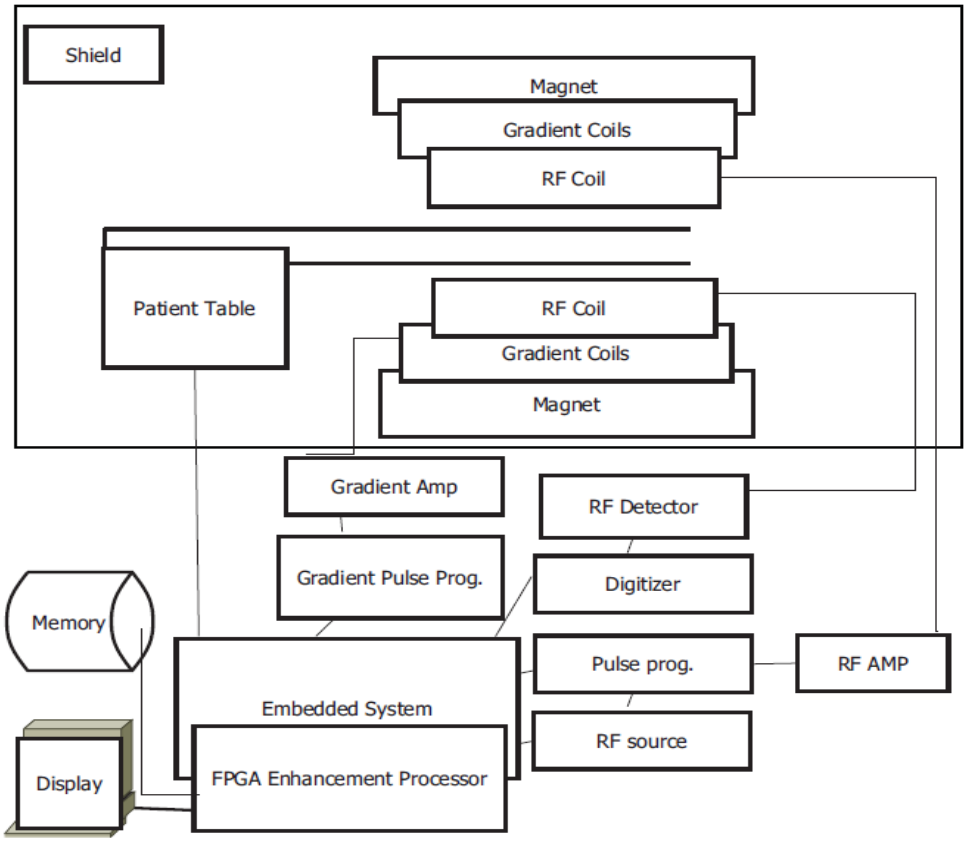

Fig. 28 An existing medical image sensing system with the proposed enhancement processor embedded within it. [36]

4.7 Comparison of the Individual Enhancement Techniques

In this section a comparison between each enhancement algorithm on the basis of the resources utilized in terms of slices and their maximum operating frequency is presented.

Table 9 Resource Utilization and Maximum Operating Frequency of the Proposed Architectures

Algorithms	**No. of Slices**	**Max. Frequency (MHz)**	**Min. Period (ns)**
Contrast Stretching	26/3584 (0.8%)	66.988	14.928
Image Negative	14/3584 (0.5%)	299.312	3.341
Log Transformation	**19/3584 (0.5%)**	**355.114**	**2.816**
Histogram Equalization	1741/3584 (48%)	226.552	4.414

High operating frequency of each image enhancement algorithm when considered individually is depicted in Table 9. This is the effect of single stage pipelining that is increasing the throughput of each algorithm.

Chapter 5

Conclusions and Future Work

A new weighted LIP model based image enhancement method was presented. Two location based parameters with LIP multiplication are used in the method which produces results that are better than the method without parameters; the method using parameters with conventional multiplication and global histogram equalization. This was illustrated both by observing the enhanced results as well as their contrast measure values. The method that used location based parameters with LIP multiplication provided the maximum value of the contrast measure and hence increased information. A novel region based contrast measure called LRCM was presented and compared with other traditional measures. The presented measure was used for finding the optimum parameters for the proposed method. It was found that the presented measure commensurate with a conventional measure in one case while it outperforms for the other out of the experiments carried out on two data sets.

The proposed resource efficient-single stage pipelined VLSI architectures provides a constant, strictly defined latency and throughput of the image enhancement path, which fulfills the main condition of real-time imaging systems. The cost of the proposed implementations is relatively low. Implementing the algorithms is well supported by widespread design tools (VHDL compilers, libraries, etc.). In future issues like power consumption and size of the device may encourage us to embed the processor into the existing medical image sensing unit and existing digital camera framework specially for on road fog degraded images. The possibility of implementing the selected

processor in FPGA provides the means for implementing the required low level and additional high level procedures (image enhancement, pattern recognition, etc.).

References

[1] R. C. Gonzales and R. E. Woods, *Digital Image Processing*. Prentice- Hall, 2002.

[2] M. Jourlin and J. C. Pinoli, Logarithmic image processing: The mathematical and physical framework for the representation and processing of transmitted images, Adv. Imag. Electron Phys., vol. 115, pp. 129–196, (2001).

[3] I.E. Gordan, Theories of Visual Perception, Wiley, New York, (1989).

[4] R.C. Gonzales and P. Wintz, Digital Image Processing, Addison-Wesley, (1987).

[5] A.K. Jain, Fundamentals of Digital Image Processing, Prentice Hall, (1989).

[6] H. Shvayster and S. Peleg, Pictures as elements in a vector space, in: Proc. IEEE Conf. Comput. Vision Pattern Recogn, Washington, June (1983), pp. 442-446.

[7] S.G. Narasimhan and S.K. Nayar, Vision and the Atmosphere, Int'l J. Computer Vision, vol. 48, pp. 233-254, (2002).

[8] S.G. Narasimhan and S.K. Nayar, Interactive Deweathering of an Image Using Physical Models, Proc. IEEE Workshop Color & Photometric Methods in Computer Vision, (2003).

[9] S.G. Narasimhan, C. Wang, and S.K. Nayar, All the Images of an Outdoor Scene, Proc. European Conf. Computer Vision, pp. 148-162, (2002).

[10] Y.Y. Schechner, S.G. Narasimhan, and S.K. Nayar, Polarization-Based Vision through Haze, Applied Optics, vol. 42, pp. 511-525, (2003).

[11] Korpel, A., "Gabor: Frequency, Time, and Memory," Applied Optics, 1982, Vol 132, pp. 3624-3632.

[12] Titchmarsh, E. C., "Introduction to the Theory of Fourier Integral," Oxford UniversityPress, 1950, 394 pp.

[13] J.P. Oakley and B.L. Satherley, Improving Image Quality in Poor Visibility Conditions Using a Physical Model for Contrast Degradation, IEEE Trans. Image Processing, vol. 7, pp. 167-179, (1998).

[14] Y. Yitzhaky, I. Mor, A. Lantzman, and N. S. Kopeika, Direct method for restoration of motion-blurred images, J. Opt. Soc. Am. , Vol. 15, No. 6, June (1998).

[15] R.T. Tan, Nikhlas Petersson and Lars Petersson, Visibility enhancement for roads with foggy or hazy scenes, Proc. IEEE Intelligent Vehicles Symposium, June

(2007).

[16] J. Dusek and K. Roubik, Testing of new models of the human visual system for image quality evaluation, in Proc. IEEE 7th Int. Symp. Signal Process. Appl., Jul. (2003), vol. 2, pp. 621–622.

[17] K.K. Sharma et al., Contrast Enhancement Algorithm for fog-degraded images, Proceedings of Third National Conference on Vision, Pattern Recognition, Image Processing and Graphics, pp. 62, Nov. (2010).

[18] M. K. Kundu and S. K. Pal, Thresholding for edge detection using human psychovisual phenomena, Pattern Recognit. Lett. vol. 4, no. 6, pp. 433–441, Dec. (1986).

[19] R. A. Nobakht and S. A. Rajala, An image coding technique using a human visual system model and image analysis criteria, in Proc. IEEE Int. Conf. Acoust., Speech, Signal Process., Apr. (1987), vol. 12, pp. 1358–1361.

[20] G. Buchsbaum, An analytical derivation of visual nonlinearity, IEEE Trans. Biomed. Eng., vol. BME-27, no. 5, pp. 237–242, May (1980).

[21] C. Munteanu and A. Rosa, Gray-scale image enhancement as an automatic process driven by evolution, IEEE Trans. Syst., Man, Cybern., vol. 34, no. 2, pp. 1292–1298, Apr. (2004).

[22] D.J. Granrath, The role of human visual models in image processing, Proc. IEEE 69, pp.552-561, May. (1981).

[23] Marek Wnuk, "Remarks on Hardware Implementation of Image Processing Algorithms", *Int. J. Appl. Math. Comput. Sci.,2*008, Vol. 18, No. 1, 105–110

[24] Hitendra Gupta and K.K. Sharma, "FPGA Implementation of Visible Watermarking Processor"*, Proceedings of 13th IEEE/VSI VLSI Design and Test Symposium*, July 2009.

[25] M. Jourlin and J. C. Pinoli, A Model for logarithmic image processing, J. Microsc., vol. 149, pp. 21–35, Jan (1988).

[26] J. C. Pinoli, The logarithmic image processing model: Connections with human brightness perception and contrast estimators, Journal of Mathematical Imaging and Vision, 7, pp. 341–358, (1997).

[27] E. Peli, Contrast in complex images, J. Opt. Soc. Amer. A, vol. 7, pp. 2032–2040, (1990).

[28] A. A. Michelson, Studies in Optics. Chicago, IL: Univ. Chicago Press, (1927).

[29] June 4, 2013) The camera technical [Online].
Available: http://www.maxmax.com/camera_technical.

[30] Bradley S. Carlson, Comparison of Modem CCD and CMOS Image Sensor Technologies and Systems for Low Resolution Imaging, IEEE Sensors Conference (2002).

[31] S. S. Agaian, K. Panetta, and A. M. Grigoryan, A new measure of image enhancement, presented at the IASTED Int. Conf. Signal Processing Communication, Marbella, Spain, Sep. 19–22, (2000).

[32] S. Agaian, B. Silver, and K. Panetta, Transform coefficient histogram based image enhancement algorithms using contrast entropy, IEEE Transactions on Image Processing, vol. 16, no. 3, pp. 741–758, March (2007).

[33] Hitendra Gupta, K.K. Sharma and S.D. Joshi, "A Weighted Logarithmic Model based Enhancement of Weather Degraded Images", *International Journal of Signal Processing, Image Processing and Pattern Recognition (IJSIP),* Vol.6, No.6 (2013), pp.229-244, http://dx.doi.org/10.14257/ijsip.2013.6.6.22.

[34] Hitendra Gupta, K.K. Sharma and S.D. Joshi, "VLSI Architecture and FPGA Implementation of Image Enhancement Algorithms", CD *Proceedings of 15th IEEE/VSI VLSI Design and Test Symposium*, July 2011.

[35] S. Cadambi, J. Weener, S.C. Goldstein, H. Schmit, D.E. Thomas, "Managing Pipeline-Reconfigurable FPGAs", *Proceedings of the 1998 ACM/SIGDA 6th international symposium on Field Programmable Gate Arrays*, pp. 55-64.

[36] Hitendra Gupta, Kamalesh Kumar Sharma & Shiv Dutt Joshi (2015), "Resource Efficient FPGA Implementation of Adaptive Image Enhancement Algorithms", *IETE Journal of Research*, 61:4, 429-439, DOI: 10.1080/03772063.2015.1009397

[37] Du-Yih Tsai1, Noriyuki Takahashi1, and Yongbum Lee, "An Adaptive Enhancement Algorithm for CT Brain Images, "*Proceedings of the 2005 IEEE Engineering in Medicine and Biology 27th Annual Conference Shanghai, China, September, 2005.*

[38] Joanna M. Wardlaw FRCP, FRCR, MD Orell Mielke, MD, "Early Signs of Brain Infarction at CT: Observer Reliability and outcome after Thrombolytic Treatment —Systematic Review1*" Radiology*, May 2005, 235, 444-453.

[39] A. M. Alsuwailemm, “A novel FPGA based realtime histogram equalization circuit for infrared image enhancement,” J. Act.Passive Electron. Devices, Vol. 3, no. 3 4, pp. 311321, 2008.

[40] Feldman, M., “Consider High Harmonics for Identification of Non-linear Systems by Hilbert Transform,” Mechanical Systems and Signal Processing, 2007, Vol 7, pp.943-958.

[41] Pal T., “Visibility Enhancement of Fog Degraded Image Sequences on SAMEER TU Dataset Using Dark Channel Strategy,” IEEE 9th International Conference on Computing, Communication and Networking Technologies, 2018.

[42] Danve S. et. al, “Fog correction using exponential contrast restoration,” IEEE 4th International Conference on Computing Communication Control and Automation, 2018.

Appendix A

A.1 RTL Synthesis

A.1.1 Contrast Stretching Transformation

```
=========================================================================
                                Final Report
=========================================================================
Final Results
RTL Top Level Output File Name     : main1.ngr
Top Level Output File Name         : main1
Output Format                      : NGC
Optimization Goal                  : Speed
Keep Hierarchy                     : NO

Design Statistics
# IOs                   : 18

Cell Usage :
# BELS                  : 59
#      GND               : 1
#      INV               : 2
#      LUT2              : 1
#      LUT2_D            : 1
#      LUT2_L            : 1
#      LUT3              : 8
#      LUT3_L            : 2
#      LUT4              : 28
#      LUT4_D            :2
#      LUT4_L            : 7
#      MUXF5             :5
#      VCC               :1
# Flip-Flops/Latches     :17
#      FDC               :17
# Clock Buffers          :1
#      BUFGP             :1
# IO Buffers             :17
#      IBUF              : 9
#      OBUF              : 8
# MULTs                  : 2
#      MULT18X18S        :  2
=========================================================================
      ======
```

Device utilization summary:

Selected Device : 3s400pq208-4

Number of Slices:	26	out of	3584	0%
Number of Slice Flip Flops:	17	out of	7168	0%
Number of 4 input LUTs:	52	out of	7168	0%
Number of IOs:	18			
Number of bonded IOBs:	18	out of	141	12%
Number of MULT18X18s:	2	out of	16	12%
Number of GCLKs:	1	out of	8	12%

Partition Resource Summary:

No Partitions were found in this design.

Minimum period: 14.928ns (Maximum Frequency: 66.988MHz)
Minimum input arrival time before clock: 1.825ns
Maximum output required time after clock: 7.165ns
Maximum combinational path delay: No path found

RTL Schematic

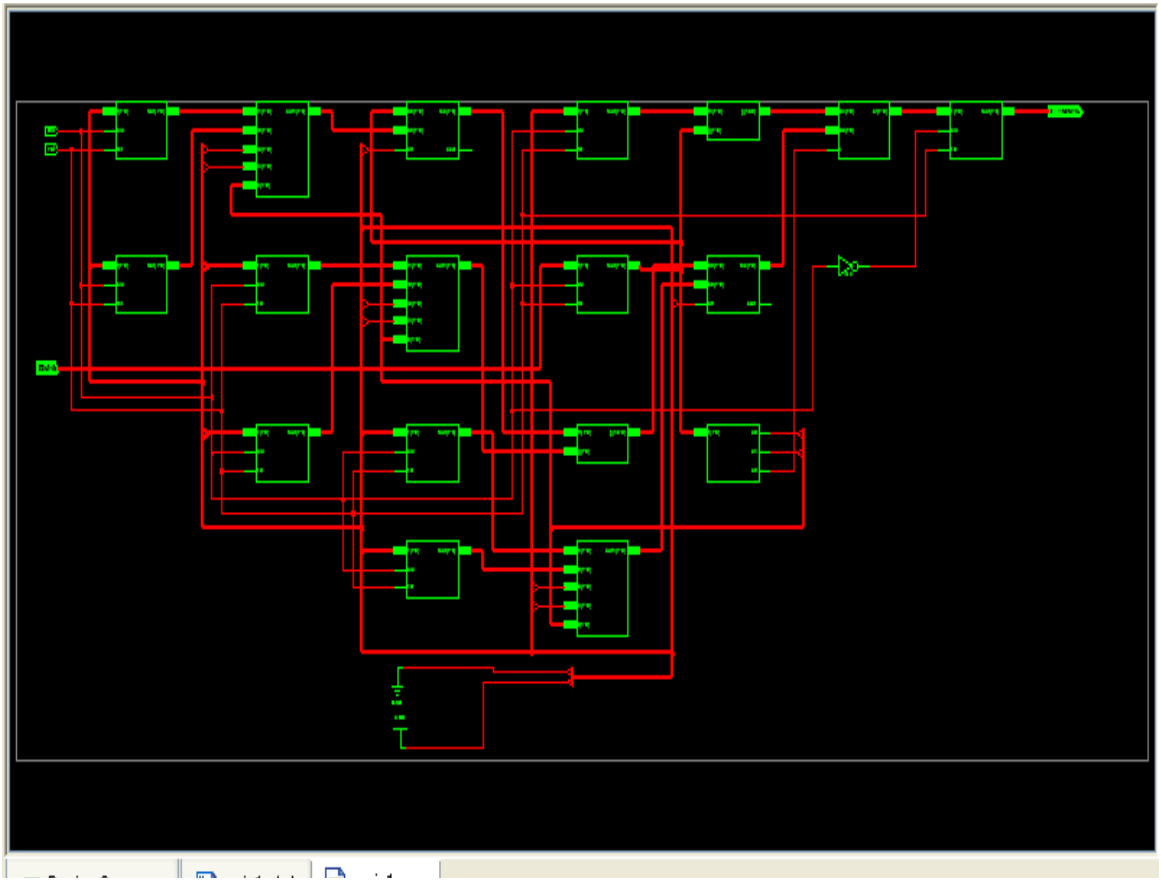

Fig A.1

A.1.1.1 Adder/subtractor

```
=========================================================================
                            Final Report
=========================================================================
Final Results
RTL Top Level Output File Name     : addsub1.ngr
Top Level Output File Name         : addsub1
Output Format                      : NGC
Optimization Goal                  : Speed
Keep Hierarchy                     : NO

Design Statistics
# IOs                   : 26

Cell Usage :
# BELS                  : 16
#      LUT2              : 1
#      LUT3              : 1
#      LUT4              : 14
# IO Buffers            : 26
#      IBUF              : 17
#      OBUF              : 9
=========================================================================
Device utilization summary:
---------------------------

Selected Device : 3s400pq208-4

 Number of Slices:              9  out of   3584     0%
 Number of 4 input LUTs:        16  out of   7168     0%
 Number of IOs:                 26
 Number of bonded IOBs:         26  out of    141    18%

---------------------------
  Partition Resource Summary:
---------------------------

  No Partitions were found in this design.

     Speed Grade: -4

   Minimum period: No path found
   Minimum input arrival time before clock: No path found
```

Maximum output required time after clock: No path found
Maximum combinational path delay: 19.420ns

RTL Schematic

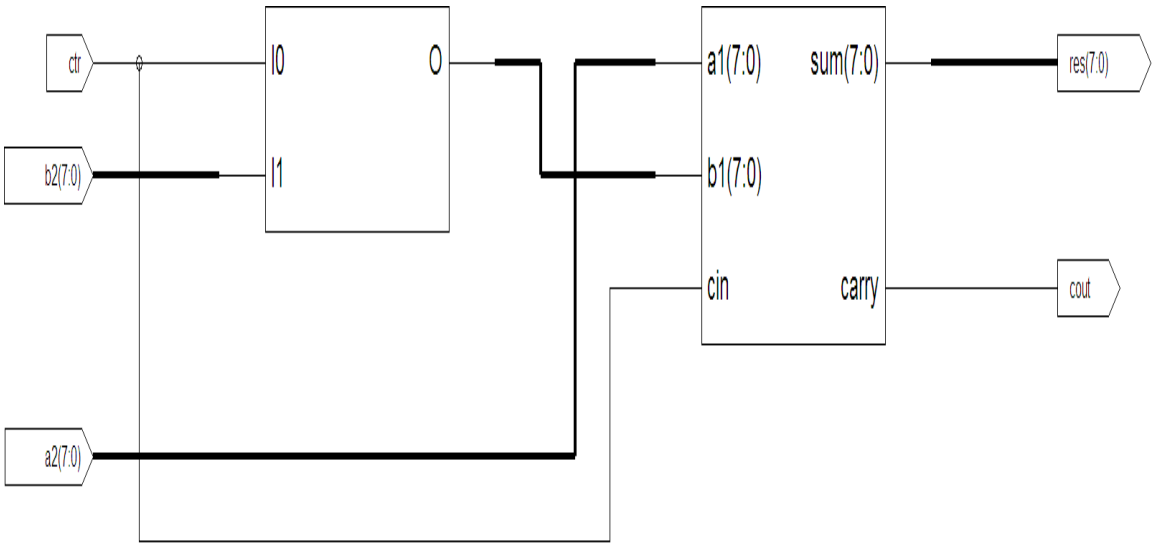

Fig A.2

A.1.1.2 8 bit comparator:

```
==========================================================================
                                Final Report
==========================================================================
Final Results
RTL Top Level Output File Name     : comparator.ngr
Top Level Output File Name         : comparator
Output Format                      : NGC
Optimization Goal                  : Speed
Keep Hierarchy                     : NO

Design Statistics
# IOs                   : 11

Cell Usage :
# BELS                  : 5
#      LUT2              : 1
#      LUT4              : 2
```

```
#      MUXF5                : 1
#      VCC                  : 1
# IO Buffers                : 11
#      IBUF                 : 8
#      OBUF                 : 3
=========================================================================
Device utilization summary:
---------------------------

Selected Device : 3s400pq208-4

 Number of Slices:              2 out of   3584     0%
 Number of 4 input LUTs:        3 out of   7168     0%
 Number of IOs:                 11
 Number of bonded IOBs:         11 out of    141     7%

---------------------------
 Partition Resource Summary:
---------------------------

 No Partitions were found in this design.

---------------------------
   Speed Grade: -4

   Minimum period: No path found
   Minimum input arrival time before clock: No path found
   Maximum output required time after clock: No path found
   Maximum combinational path delay: 10.970ns
```

RTL Schematic:

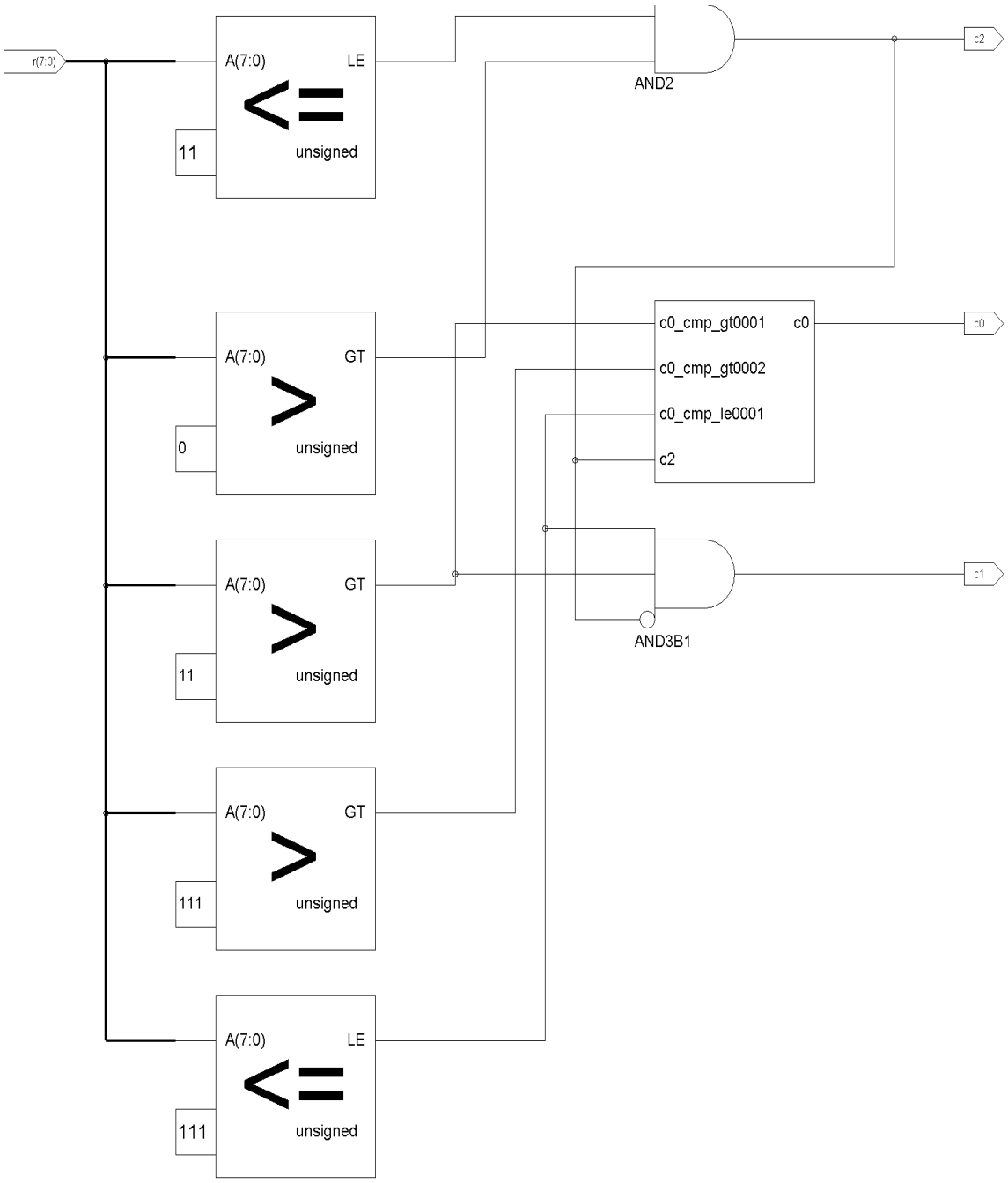

Fig A.3

A.1.1.3 Multiplier(8 bit):

```
=========================================================================
                            Final Report
=========================================================================
Final Results
RTL Top Level Output File Name     : multiplier1.ngr
Top Level Output File Name         : multiplier1
Output Format                      : NGC
Optimization Goal                  : Speed
Keep Hierarchy                     : NO

Design Statistics
# IOs                   : 33

Cell Usage :
# BELS                  : 2
#      GND               : 1
#      VCC               : 1
# Clock Buffers         : 1
#      BUFGP             : 1
# IO Buffers            : 32
#      IBUF              : 16
#      OBUF              : 16
# MULTs                 : 1
#      MULT18X18S        : 1
=========================================================================
      ======

 Device utilization summary:

 Selected Device : 3s400pq208-4

 Number of Slices:              0  out of   3584     0%
 Number of IOs:                 33
 Number of bonded IOBs:         33  out of    141    23%
 Number of MULT18X18s:          1  out of     16     6%
 Number of GCLKs:               1  out of      8    12%

---------------------------
 Partition Resource Summary:
---------------------------

 No Partitions were found in this design.
```

Speed Grade: -4

Minimum period: No path found
Minimum input arrival time before clock: 3.732ns
Maximum output required time after clock: 7.761ns
Maximum combinational path delay: No path found

RTL Schematic

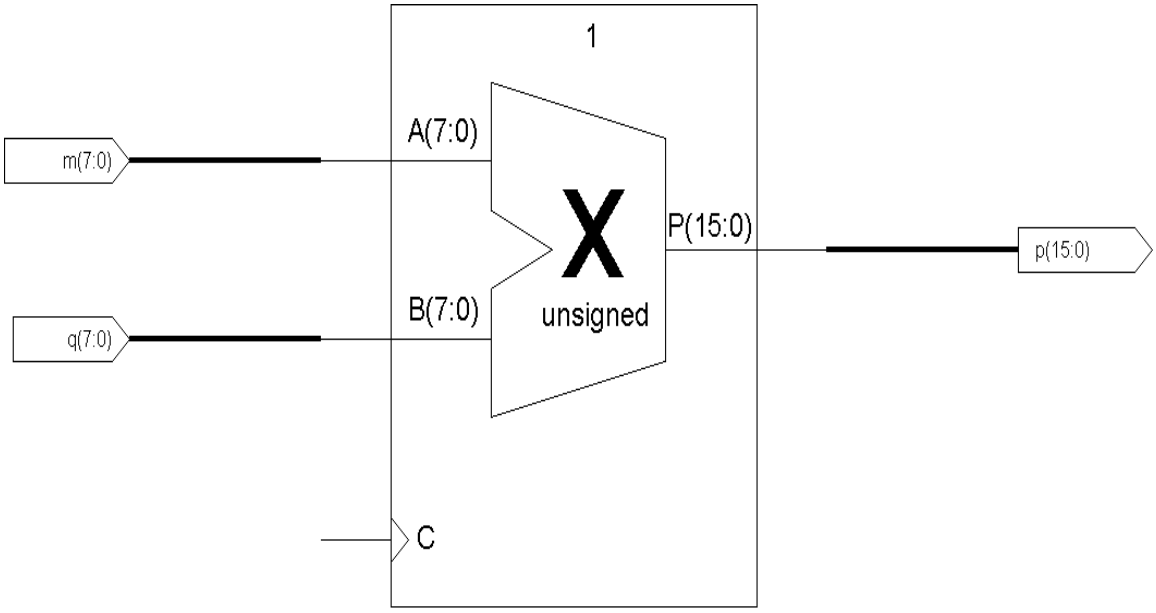

Fig A.4

A.1.1.4 MUX 4:1:

```
=========================================================================
                            Final Report
=========================================================================
Final Results
RTL Top Level Output File Name     : mux4to1.ngr
Top Level Output File Name         : mux4to1
Output Format                      : NGC
Optimization Goal                  : Speed
Keep Hierarchy                     : NO

Design Statistics
# IOs                   : 42

Cell Usage :
# BELS                  : 24
#      LUT3              : 16
#      MUXF5             :  8
# IO Buffers            :  42
#      IBUF              :  34
#      OBUF              :  8
=========================================================================
    ==========

 Device utilization summary:
---------------------------

 Selected Device : 3s400pq208-4

 Number of Slices:              8  out of   3584     0%
 Number of 4 input LUTs:        16  out of   7168     0%
 Number of IOs:                 42
 Number of bonded IOBs:         42  out of    141    29%

---------------------------
 Partition Resource Summary:
---------------------------

 No Partitions were found in this design.

 Timing Summary:
---------------
  Speed Grade: -4
```

Minimum period: No path found
Minimum input arrival time before clock: No path found
Maximum output required time after clock: No path found
Maximum combinational path delay: 9.753ns

RTL Schematic

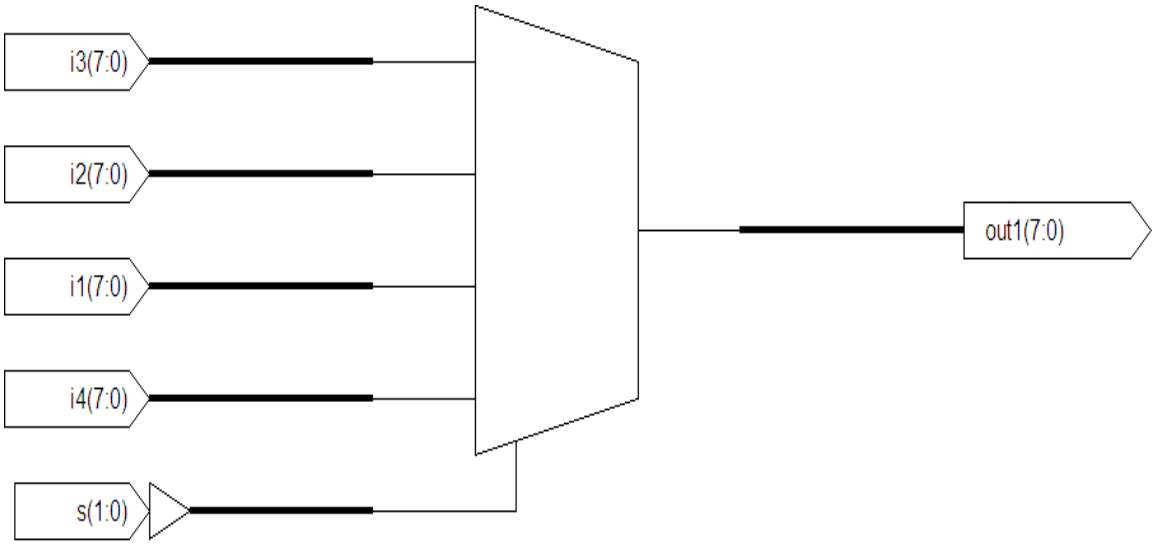

Fig A.5

A.1.1.5 MUX 2:1

```
=========================================================================
                            Final Report
=========================================================================
Final Results
RTL Top Level Output File Name     : mux2t01.ngr
Top Level Output File Name         : mux2t01
Output Format                      : NGC
Optimization Goal                  : Speed
Keep Hierarchy                     : NO

Design Statistics
# IOs                   : 25

Cell Usage :
# BELS                  : 8
```

```
#      LUT3                        : 8
# IO Buffers                       : 25
#      IBUF                        : 17
#      OBUF                        : 8
=========================================================================
```

Device utilization summary:

Selected Device : 3s400pq208-4

Number of Slices:	4	out of 3584	0%
Number of 4 input LUTs:	8	out of 7168	0%
Number of IOs:	25		
Number of bonded IOBs:	25	out of 141	17%

Timing Summary:

Speed Grade: -4

Minimum period: No path found

Minimum input arrival time before clock: No path found

Maximum output required time after clock: No path found

Maximum combinational path delay: 9.239ns

RTL Schematic

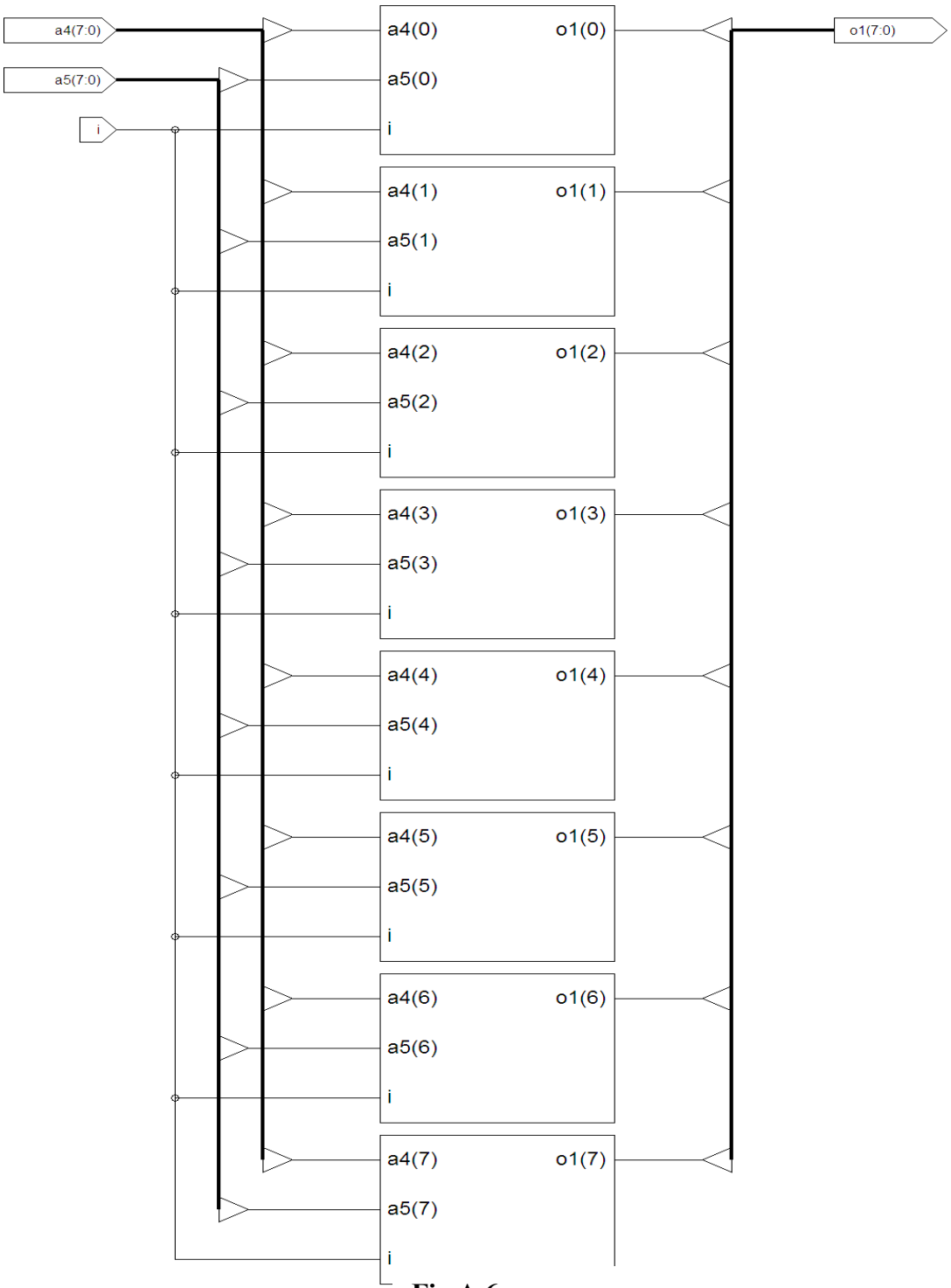

Fig A.6

A.1.1.6 Adder 8 bit:

==========

Final Report

==========

Final Results
RTL Top Level Output File Name : adder1.ngr
Top Level Output File Name : adder1
Output Format : NGC
Optimization Goal : Speed
Keep Hierarchy : NO

Design Statistics
IOs : 26

Cell Usage :
BELS : 16
LUT3 : 16
IO Buffers : 26
IBUF : 17
OBUF : 9

==========

Device utilization summary:

Selected Device : 3s400pq208-4

Number of Slices: 9 out of 3584 0%
Number of 4 input LUTs: 16 out of 7168 0%
Number of IOs: 26
Number of bonded IOBs: 26 out of 141 18%

Timing Summary:

Speed Grade: -4

Minimum period: No path found
Minimum input arrival time before clock: No path found
Maximum output required time after clock: No path found
Maximum combinational path delay: 20.394ns

RTL Schematic

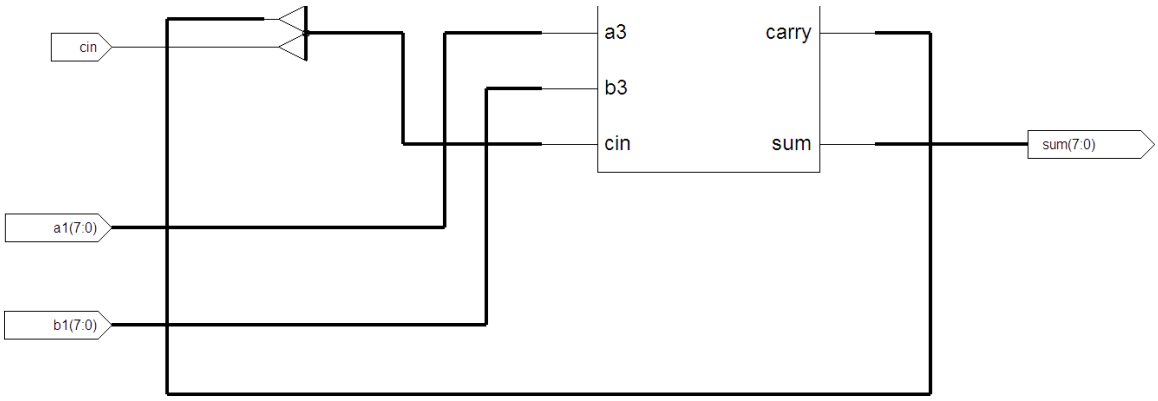

Fig A.7

A.1.2 Image Negative:

```
================================================================================
                                Final Report
================================================================================
Final Results
RTL Top Level Output File Name     : main_2.ngr
Top Level Output File Name         : main_2
Output Format                      : NGC
Optimization Goal                  : Speed
Keep Hierarchy                     : NO

Design Statistics
# IOs                              : 18

Cell Usage :
# BELS                             : 28
#      INV                         : 3
#      LUT2                        : 4
#      LUT3                        : 2
#      LUT4                        : 16
#      MUXF5                       : 2
#      VCC                         : 1
# Flip-Flops/Latches               : 23
#      FDC                         : 22
#      FDCE                        : 1
# Clock Buffers                    : 1
#      BUFGP                       : 1
# IO Buffers                       : 17
```

```
#      IBUF                : 9
#      OBUF                : 8
=========================================================================
```

Device utilization summary:

Selected Device : 3s400pq208-4

Number of Slices:	14	out of 3584	0%
Number of Slice Flip Flops:	7	out of 7168	0%
Number of 4 input LUTs:	25	out of 7168	0%
Number of IOs:	18		
Number of bonded IOBs:	18	out of 141	12%
IOB Flip Flops:	16		
Number of GCLKs:	1	out of 8	12%

Timing Summary:

Speed Grade: -4

Minimum period: 3.341ns (Maximum Frequency: 299.312MHz)
Minimum input arrival time before clock: 1.825ns
Maximum output required time after clock: 7.165ns
Maximum combinational path delay: No path found

RTL Schematic:

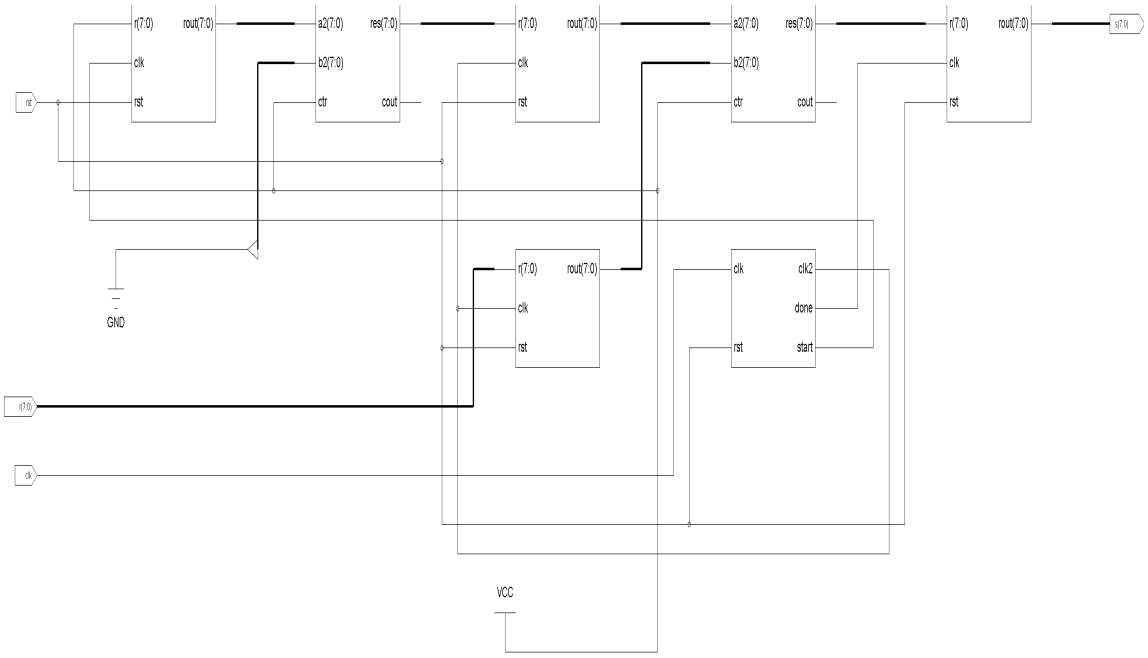

Fig A.8

A.1.2.1 Control path of image negative:

```
==========================================================================
                                Final Report
==========================================================================
Final Results
RTL Top Level Output File Name     : control_m2.ngr
Top Level Output File Name         : control_m2
Output Format                      : NGC
Optimization Goal                  : Speed
Keep Hierarchy                     : NO

Design Statistics
# IOs                   : 5

Cell Usage :
# BELS                  : 8
#      INV               : 2
```

```
#      LUT2                : 2
#      LUT3                : 1
#      LUT4                : 3
# FlipFlops/Latches        : 4
#      FDC                 : 3
#      FDCE                : 1
# Clock Buffers            : 1
#      BUFGP               : 1
# IO Buffers               : 4
#      IBUF                : 1
#      OBUF                : 3
=========================================================================
```

Device utilization summary:

Selected Device : 3s400pq208-4

Number of Slices:	4	out of	3584	0%
Number of Slice Flip Flops:	4	out of	7168	0%
Number of 4 input LUTs:	8	out of	7168	0%
Number of IOs:	5			
Number of bonded IOBs:	5	out of	141	3%
Number of GCLKs:	1	out of	8	12%

Speed Grade: -4

Minimum period: 3.341ns (Maximum Frequency: 299.312MHz)
Minimum input arrival time before clock: No path found
Maximum output required time after clock: 9.121ns
Maximum combinational path delay: No path found

RTL Schematic:

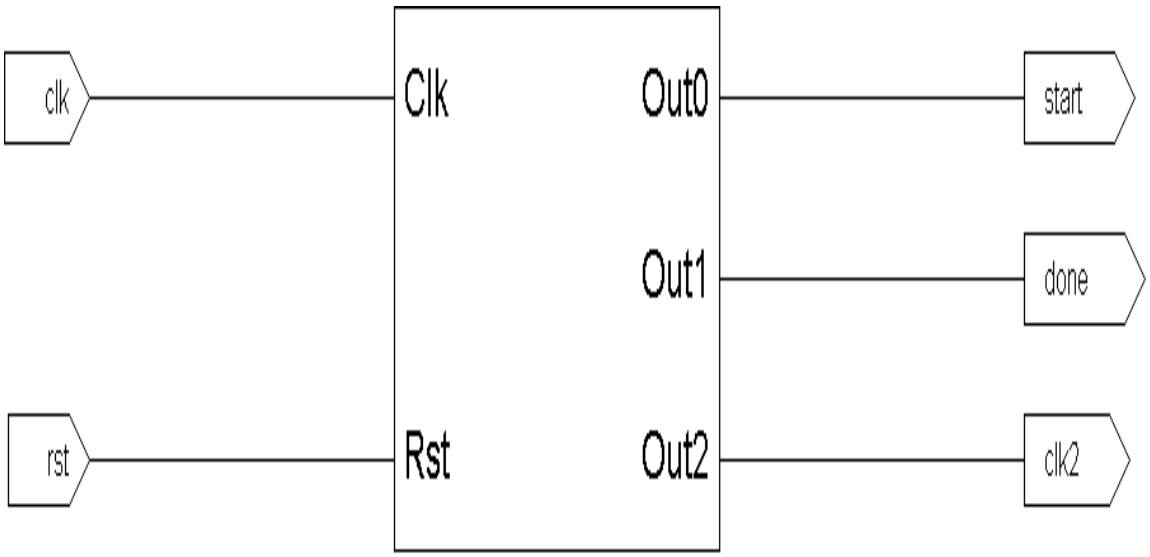

Fig A.9

A.1.3 Log transformation:

```
=========================================================================
                                Final Report
=========================================================================
Final Results
RTL Top Level Output File Name     : main_3.ngr
Top Level Output File Name         : main_3
Output Format                      : NGC
Optimization Goal                  : Speed
Keep Hierarchy                     : NO

Design Statistics
# IOs                              : 37

Cell Usage :
# BELS                             : 29
#      GND                         : 1
#      INV                         : 2
#      LUT2                        : 3
```

```
#      LUT3                 : 4
#      LUT4                 : 16
#      MUXF5                : 3
# FlipFlops/Latches         : 19
#      FDC                  : 19
# Clock Buffers             : 3
#      BUFGP                : 3
# IO Buffers                : 34
#      IBUF                 : 10
#      OBUF                 : 24
=========================================================================
      ==========

Device utilization summary:
---------------------------

Selected Device : 3s400pq208-4

 Number of Slices:              14  out of   3584     0%
 Number of Slice Flip Flops:    8  out of   7168     0%
 Number of 4 input LUTs:        25  out of   7168     0%
 Number of IOs:                 37
 Number of bonded IOBs:         37  out of    141    26%
 IOB Flip Flops:                11
 Number of GCLKs:               3  out of      8    37%

---------------------------
Partition Resource Summary:
---------------------------

  No Partitions were found in this design.


   Timing Summary:
---------------
   Speed Grade: -4

   Minimum period: No path found
   Minimum input arrival time before clock: 3.195ns
   Maximum output required time after clock: 13.766ns
   Maximum combinational path delay: 9.513ns
```

RTL Schematic:

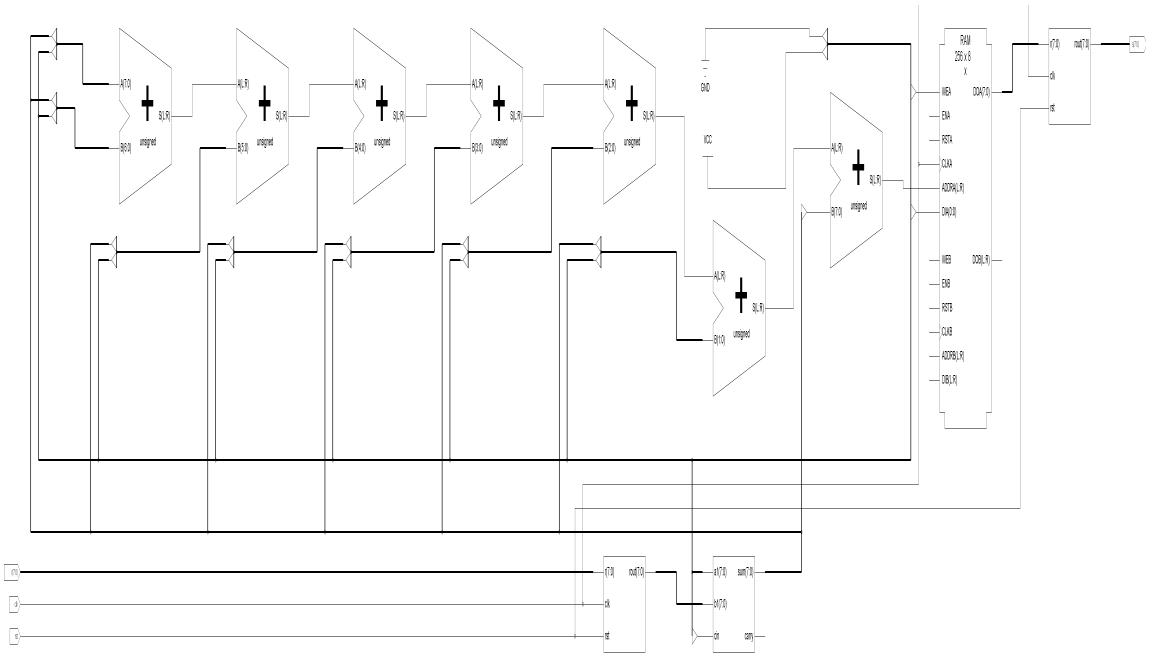

Fig A.10

Log Transformation:

```
=========================================================================
                Final Report
          ==============================================================

Final Results
RTL Top Level Output File Name     : log_final.ngr
Top Level Output File Name         : log_final
Output Format                      : NGC
Optimization Goal                  : Speed
Keep Hierarchy                     : NO

Design Statistics
# IOs                  : 34

Cell Usage :
# BELS                 : 37
#      GND              : 1
```

```
#      INV                 : 2
#      LUT2                : 4
#      LUT3                : 7
#      LUT4                : 22
#      MUXF5               : 1
# FlipFlops/Latches        : 23
#      FDC                 : 23
# Clock Buffers            : 1
#      BUFGP               : 1
# IO Buffers               : 33
#      IBUF                : 9
#      OBUF                : 24
=========================================================================
```

Device utilization summary:

Selected Device : 3s400pq208-4

Number of Slices:	19	out of	3584	0%
Number of Slice Flip Flops:	12	out of	7168	0%
Number of 4 input LUTs:	35	out of	7168	0%
Number of IOs:	34			
Number of bonded IOBs:	34	out of	141	24%
IOB Flip Flops:	11			
Number of GCLKs:	1	out of	8	12%

Partition Resource Summary:

No Partitions were found in this design.

Timing Summary:
Speed Grade: -4

Minimum period: 2.816ns (Maximum Frequency: 355.114MHz)
Minimum input arrival time before clock: 1.825ns
Maximum output required time after clock: 14.953ns
Maximum combinational path delay: No path found

RTL Schematic:

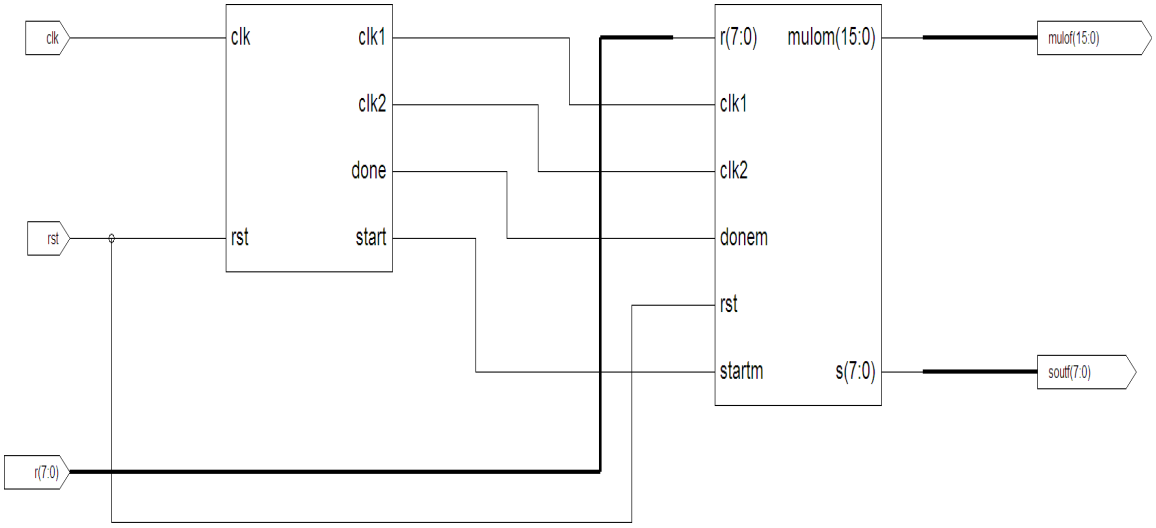

Fig A.3.1

A.1.3.1 Logarithmic Block:

==========

Final Report

==========

Final ResultsFinal
RTL Top Level Output File Name : logt_rom.ngr
Top Level Output File Name : logt_rom
Output Format : NGC
Optimization Goal : Speed
Keep Hierarchy : NO

Design Statistics
IOs : 17

Cell Usage :
BELS : 18
GND : 1
LUT2 : 1
LUT3 : 2
LUT4 : 12
MUXF5 : 2
IO Buffers : 17
IBUF : 9
OBUF : 8

==========

Device utilization summary:

Selected Device : 3s400pq208-4

Number of Slices:	9 out of 3584	0%
Number of 4 input LUTs:	15 out of 7168	0%
Number of IOs:	17	
Number of bonded IOBs:	17 out of 141	12%

Speed Grade: -4

Minimum period: No path found
Minimum input arrival time before clock: No path found
Maximum output required time after clock: No path found
Maximum combinational path delay: 14.129ns

RTL Schematic:

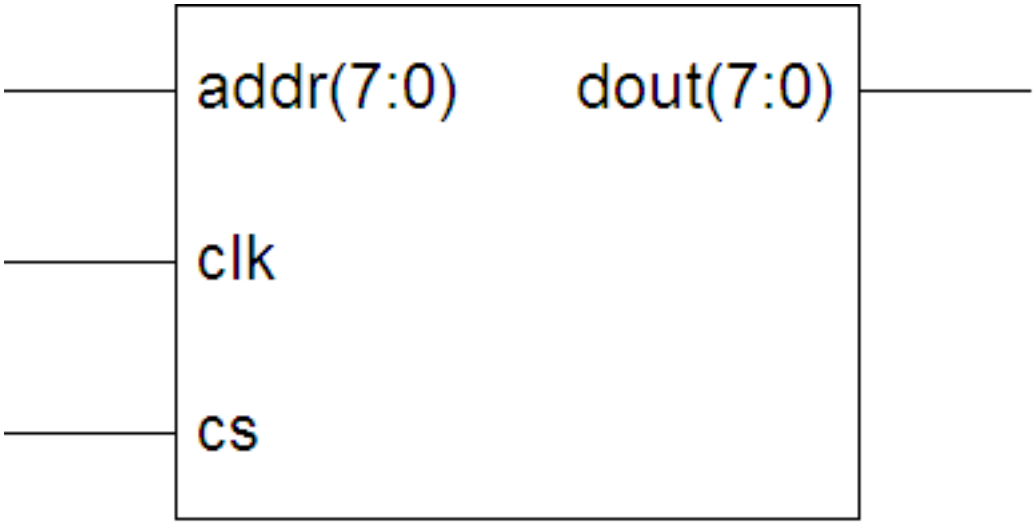

Fig A.11

A.1.3.2 Control path of log-transformation:

```
=========================================================================
                            Final Report
=========================================================================
Final Results
RTL Top Level Output File Name     : control_2.ngr
Top Level Output File Name         : control_2
Output Format                      : NGC
Optimization Goal                  : Speed
Keep Hierarchy                     : NO

Design Statistics
# IOs                              : 6

Cell Usage :
# BELS                             : 9
#      INV                         : 1
#      LUT2                        : 1
#      LUT3                        : 2
#      LUT4                        : 5
# FlipFlops/Latches                : 4
#      FDC                         : 4
# Clock Buffers                    : 1
#      BUFGP                       : 1
# IO Buffers                       : 5
#      IBUF                        : 1
#      OBUF                        : 4
=========================================================================
Device utilization summary:
---------------------------

Selected Device : 3s400pq208-4

 Number of Slices:                5  out of   3584     0%
 Number of Slice Flip Flops:      4  out of   7168     0%
 Number of 4 input LUTs:          9  out of   7168     0%
 Number of IOs:                   6
 Number of bonded IOBs:           6  out of    141     4%
 Number of GCLKs:                 1  out of      8    12%

---------------------------
   Timing Summary:
---------------
```

Speed Grade: -4

Minimum period: 2.816ns (Maximum Frequency: 355.114MHz)
Minimum input arrival time before clock: No path found
Maximum output required time after clock: 9.138ns
Maximum combinational path delay: No path found

RTL Schematic:

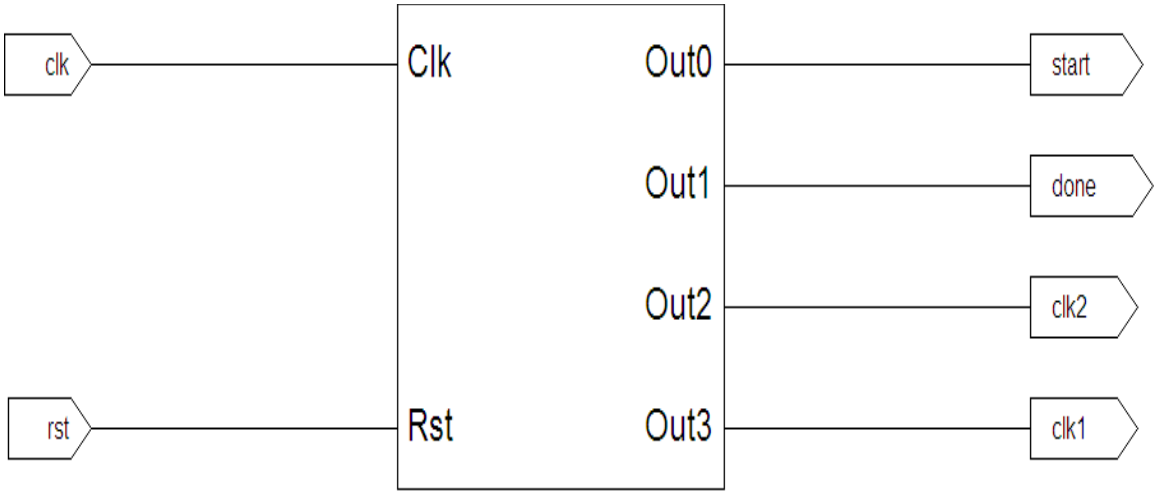

Fig A.12

A.1.4 Histogram Equalization:

```
==========================================================================
                                Final Report
==========================================================================
Final Results
RTL Top Level Output File Name     : hist_4.ngr
Top Level Output File Name         : hist_4
Output Format                      : NGC
Optimization Goal                  : Speed
Keep Hierarchy                     : NO

Design Statistics
# IOs                              : 18

Cell Usage :
# BELS                             : 8009
#      GND                         : 1
#      INV                         : 261
#      LUT1                        : 1792
#      LUT2                        : 13
#      LUT3                        : 1087
#      LUT4                        : 285
#      MUXCY                       : 1792
#      MUXF5                       : 529
#      MUXF6                       : 264
#      MUXF7                       : 128
#      MUXF8                       : 64
#      VCC                         : 1
#      XORCY                       : 1792
# FlipFlops/Latches                : 2068
#      FDC                         : 12
#      FDCE                        : 2048
#      LD                          : 8
# Clock Buffers                    : 2
#      BUFG                        : 1
#      BUFGP                       : 1
# IO Buffers                       : 17
#      IBUF                        : 9
#      OBUF                        : 8
==========================================================================
Device utilization summary:
---------------------------
```

Selected Device : 3s400pq208-4

Number of Slices:	1741	out of 3584	48%
Number of Slice Flip Flops:	2052	out of 7168	28%
Number of 4 input LUTs:	3438	out of 7168	47%
Number of IOs:	18		
Number of bonded IOBs:	18	out of 141	12%
IOB Flip Flops:	16		
Number of GCLKs:	2	out of 8	25%

Timing Summary:

Speed Grade: -4

Minimum period: 4.414ns (Maximum Frequency: 226.552MHz)
Minimum input arrival time before clock: 1.825ns
Maximum output required time after clock: 7.078ns
Maximum combinational path delay: No path found

RTL Schematic:

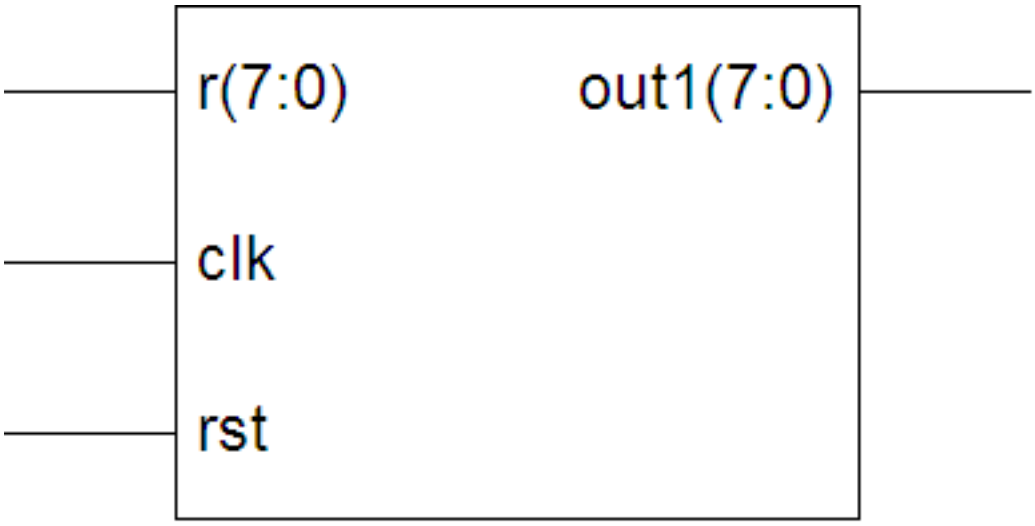

Fig A.13

A.1.4.1 Decoder 8 to 256:

```
==========================================================================
                                  Final Report
==========================================================================
Final Results
RTL Top Level Output File Name     : decoder8to256.ngr
Top Level Output File Name         : decoder8to256
Output Format                      : NGC
Optimization Goal                  : Speed
Keep Hierarchy                     : NO

Design Statistics
# IOs                              : 265

Cell Usage :
# BELS                             : 304
#      LUT2                        : 11
#      LUT3                        : 22
#      LUT4                        : 271
# IO Buffers                       : 265
#      IBUF                        : 9
#      OBUF                        : 256
==========================================================================
Device utilization summary:
---------------------------

Selected Device : 3s400pq208-4

 Number of Slices:              175  out of   3584     4%
 Number of 4 input LUTs:        304  out of   7168     4%
 Number of IOs:                 265
 Number of bonded IOBs:         265  out of    141   187% (*)

Timing Summary:
---------------
Speed Grade: -4

   Minimum period: No path found
   Minimum input arrival time before clock: No path found
   Maximum output required time after clock: No path found
   Maximum combinational path delay: 14.730ns
```

RTL Schematic:

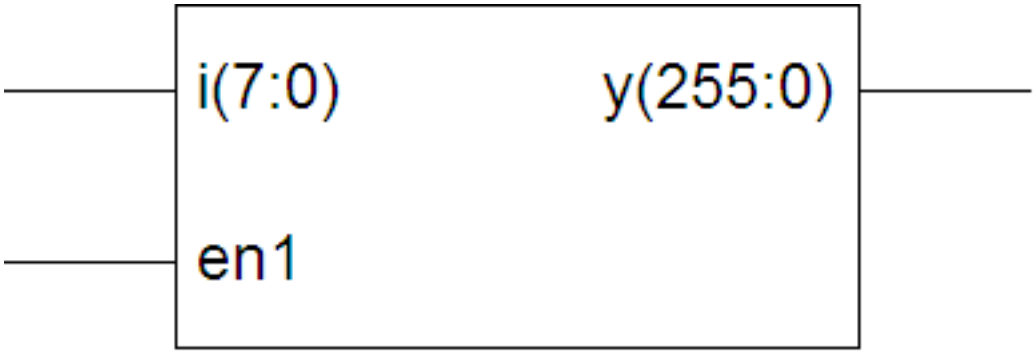

Fig A.14

A.1.4.2 Counter 8 bit:

```
==========================================================================
                                Final Report
==========================================================================
Final Results
RTL Top Level Output File Name     : counter8.ngr
Top Level Output File Name         : counter8
Output Format                      : NGC
Optimization Goal                  : Speed
Keep Hierarchy                     : NO

Design Statistics
# IOs                              : 11

Cell Usage :
# BELS                             : 25
#      GND                         : 1
#      INV                         : 2
#      LUT1                        : 7
#      MUXCY                       : 7
#      VCC                         : 1
#      XORCY                       : 7
# FlipFlops/Latches                : 8
#      FDCE                        : 8
# Clock Buffers                    :1
#      BUFGP                       :1
```

```
# IO Buffers                  : 10
#      IBUF                   : 2
#      OBUF                   : 8
=========================================================================
Device utilization summary:
---------------------------

Selected Device : 3s400pq208-4

 Number of Slices:              4  out of   3584     0%
 Number of Slice Flip Flops:    8  out of   7168     0%
 Number of 4 input LUTs:        9  out of   7168     0%
 Number of IOs:                11
 Number of bonded IOBs:        11  out of    141     7%
 Number of GCLKs:               1  out of      8    12%


  Timing Summary:
---------------
  Speed Grade: -4

   Minimum period: 4.414ns (Maximum Frequency: 226.552MHz)
   Minimum input arrival time before clock: 2.506ns
   Maximum output required time after clock: 7.241ns
   Maximum combinational path delay: No path found

  Timing Detail:
--------------
  All values displayed in nanoseconds (ns)
```

RTL Schematic:

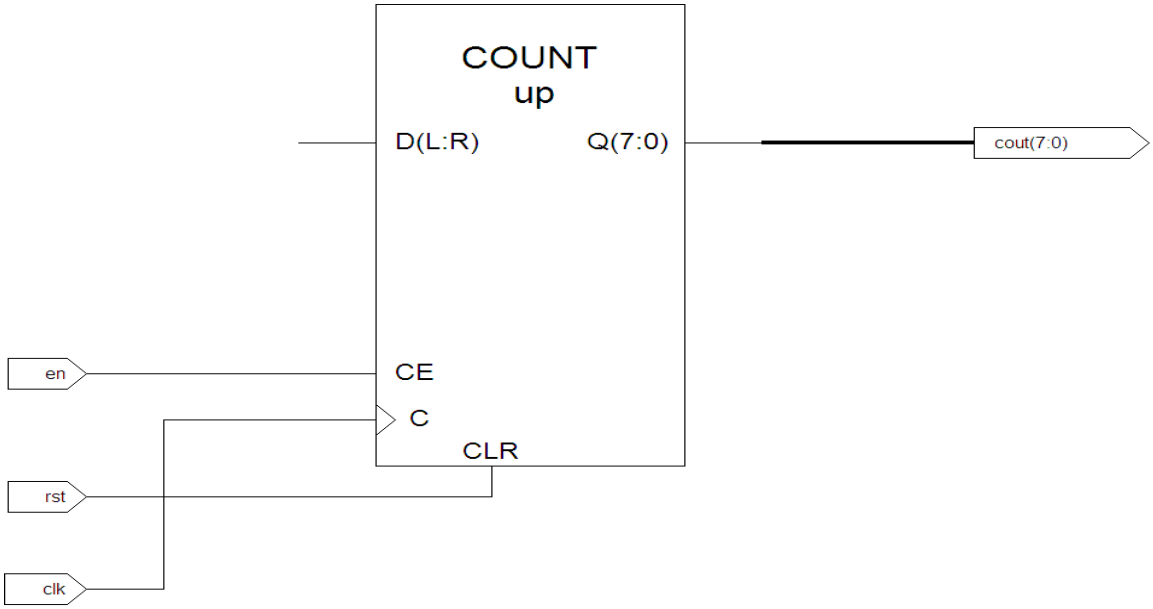

Fig A.15

A.1.4.3 MUX 256:1

```
=========================================================================
                            Final Report
=========================================================================
Final Results
RTL Top Level Output File Name     : mux256_1.ngr
Top Level Output File Name         : mux256_1
Output Format                      : NGC
Optimization Goal                  : Speed
Keep Hierarchy                     : NO

Design Statistics
# IOs                              : 2064

Cell Usage :
# BELS                             : 2043
#      BUF                         : 3
#      LUT3                        : 1056
#      MUXF5                       : 528
#      MUXF6                       : 264
```

```
#      MUXF7                : 128
#      MUXF8                : 64
# IO Buffers                : 2064
#      IBUF                 : 2056
#      OBUF                 : 8
=========================================================================
Device utilization summary:
---------------------------

Selected Device: 3s400pq208-4

 Number of Slices:              528 out of   3584    14%
 Number of 4 input LUTs:        1056 out of   7168    14%
 Number of IOs:                 2064
 Number of bonded IOBs:         2064 out of    141   1463% (*)


  Timing Summary:
---------------
   Speed Grade: -4

   Minimum period: No path found
   Minimum input arrival time before clock: No path found
   Maximum output required time after clock: No path found
   Maximum combinational path delay: 19.600ns

  Timing Detail:
--------------
  All values displayed in nanoseconds (ns)
```

RTL Schematic:

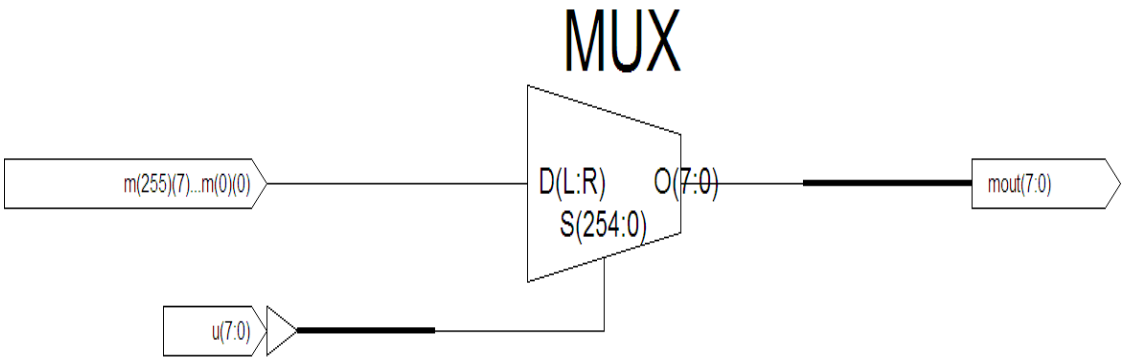

Fig A.16

A.1.4.4 RAM 256:

```
==========================================================================
                                Final Report
      ==========================================================================
Final Results
RTL Top Level Output File Name     : ram256_8.ngr
Top Level Output File Name         : ram256_8
Output Format                      : NGC
Optimization Goal                  : Speed
Keep Hierarchy                     : NO

Design Statistics
# IOs                              : 26

Cell Usage :
# FlipFlops/Latches                : 8
#      LDE                         : 8
# Clock Buffers                    : 1
#      BUFGP                       : 1
# IO Buffers                       : 17
#      IBUF                        : 9
#      OBUF                        : 8

Device utilization summary:
---------------------------
```

Selected Device : 3s400pq208-4

Number of Slices:	0	out of 3584	0%
Number of Slice Flip Flops:	8	out of 7168	0%
Number of IOs:	26		
Number of bonded IOBs:	18	out of 141	12%
IOB Flip Flops:	8		
Number of GCLKs:	1	out of 8	12%

Timing Summary:

Speed Grade: -4

Minimum period: No path found
Minimum input arrival time before clock: 2.506ns
Maximum output required time after clock: 7.078ns
Maximum combinational path delay: No path found

Timing Detail:

All values displayed in nanoseconds (ns)

RTL Schematic:

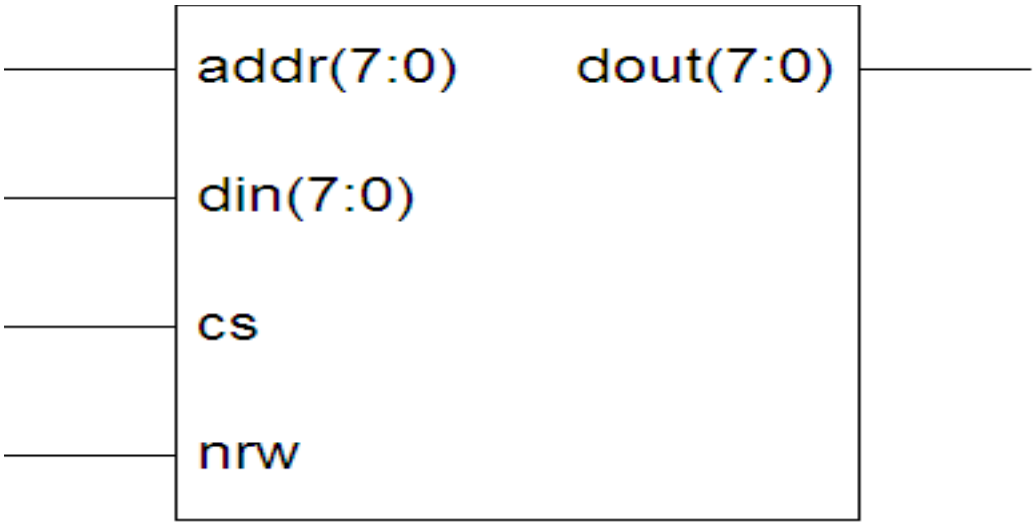

Fig A.17

A.1.4.5 Control path of histogram Equalization:

```
=========================================================================
                            Final Report
=========================================================================
Final Results
RTL Top Level Output File Name     : control_4.ngr
Top Level Output File Name         : control_4
Output Format                      : NGC
Optimization Goal                  : Speed
Keep Hierarchy                     : NO

Design Statistics
# IOs                              : 22

Cell Usage :
# BELS                             : 36
#      GND                         : 1
#      INV                         : 1
#      LUT2                        : 3
#      LUT3                        : 11
#      LUT4                        : 17
#      MUXF5                       : 3
# FlipFlops/Latches                : 4
#      FDC                         : 4
# Clock Buffers                    : 1
#      BUFGP                       : 1
# IO Buffers                       : 21
#      IBUF                        : 1
#      OBUF                        : 20
=========================================================================
 Device utilization summary:
---------------------------

 Selected Device : 3s400pq208-4

 Number of Slices:              18  out of   3584     0%
 Number of Slice Flip Flops:    4  out of   7168     0%
 Number of 4 input LUTs:        32  out of   7168     0%
 Number of IOs:                 22
 Number of bonded IOBs:         22  out of    141    15%
 Number of GCLKs:               1  out of      8    12%

  Timing Summary:
```

Speed Grade: -4

Minimum period: 2.896ns (Maximum Frequency: 345.304MHz)
Minimum input arrival time before clock: No path found
Maximum output required time after clock: 26.023ns
Maximum combinational path delay: No path found

Timing Detail:

All values displayed in nanoseconds (ns)

RTL Schematic:

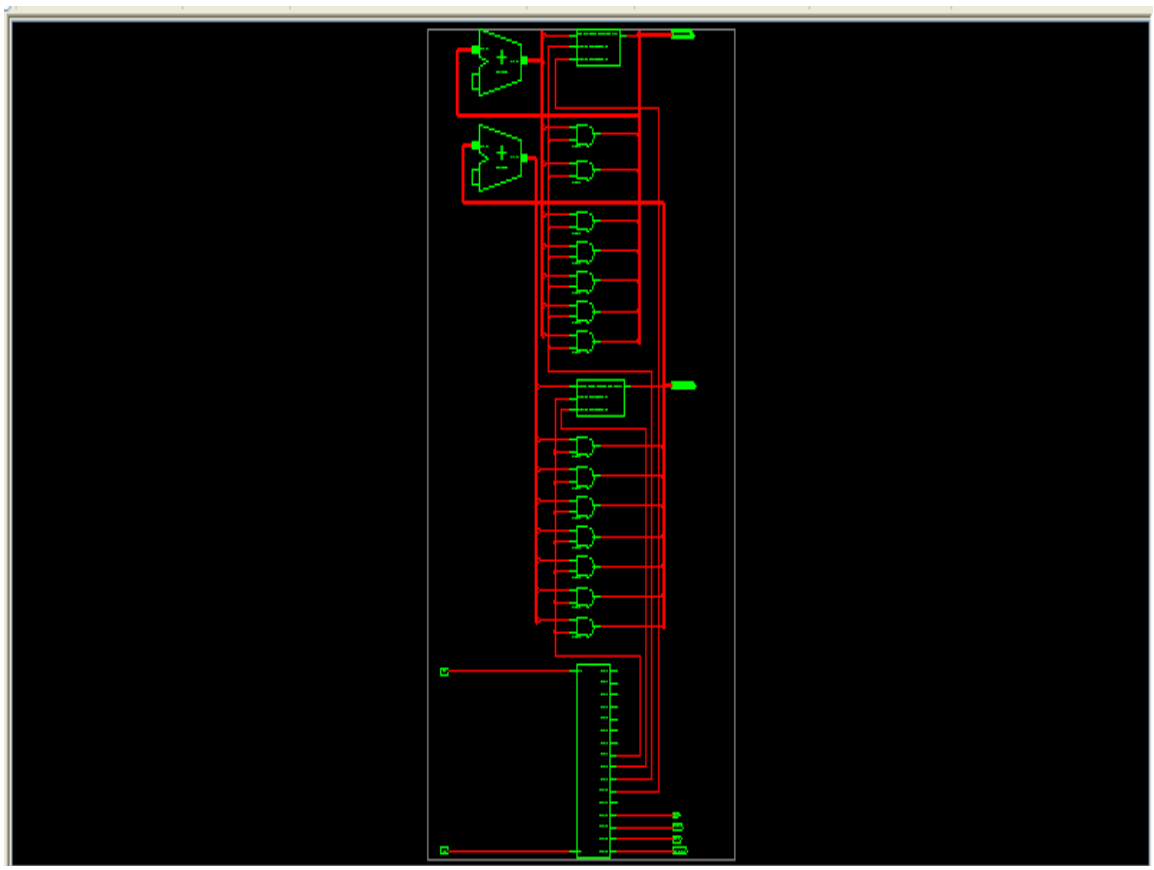

Fig A.18

Appendix B

B.1 simulation results of enhancement algorithms

B.1.1 Contrast stretching enhancement algorithm:

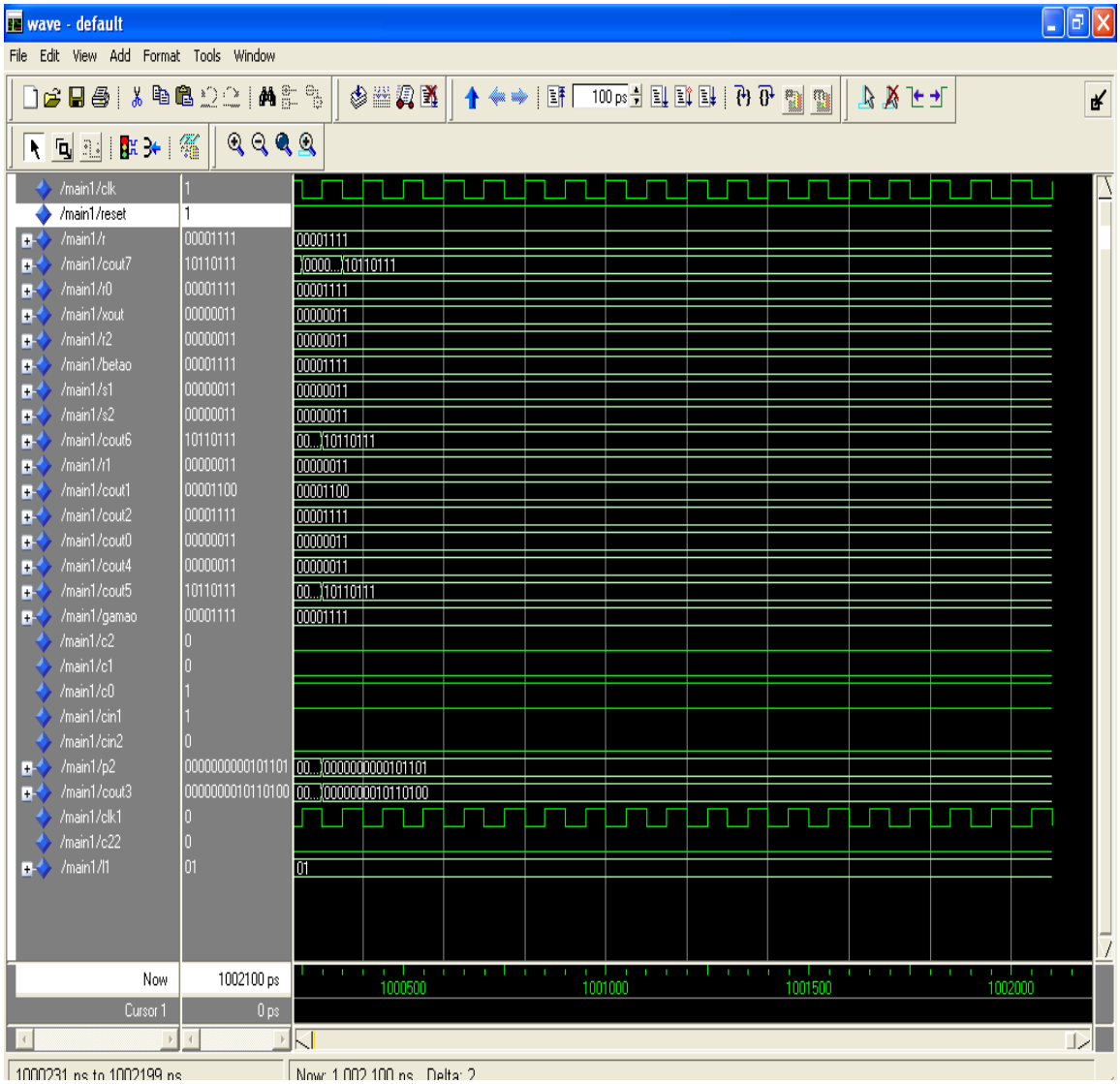

Fig B.1

B.1.1.1 Adder/subtractor:

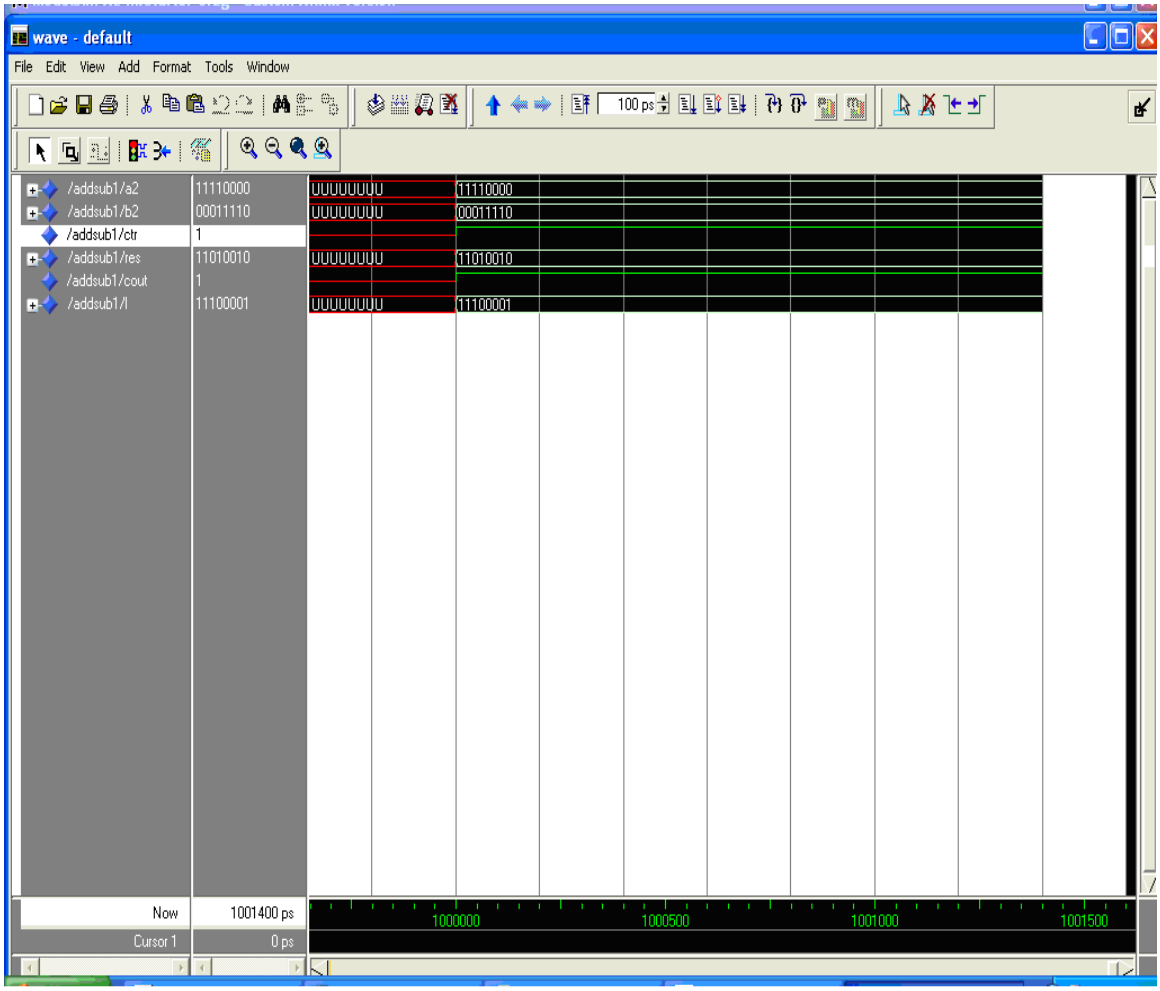

Fig B.2

B.1.1.2 Multiplier:

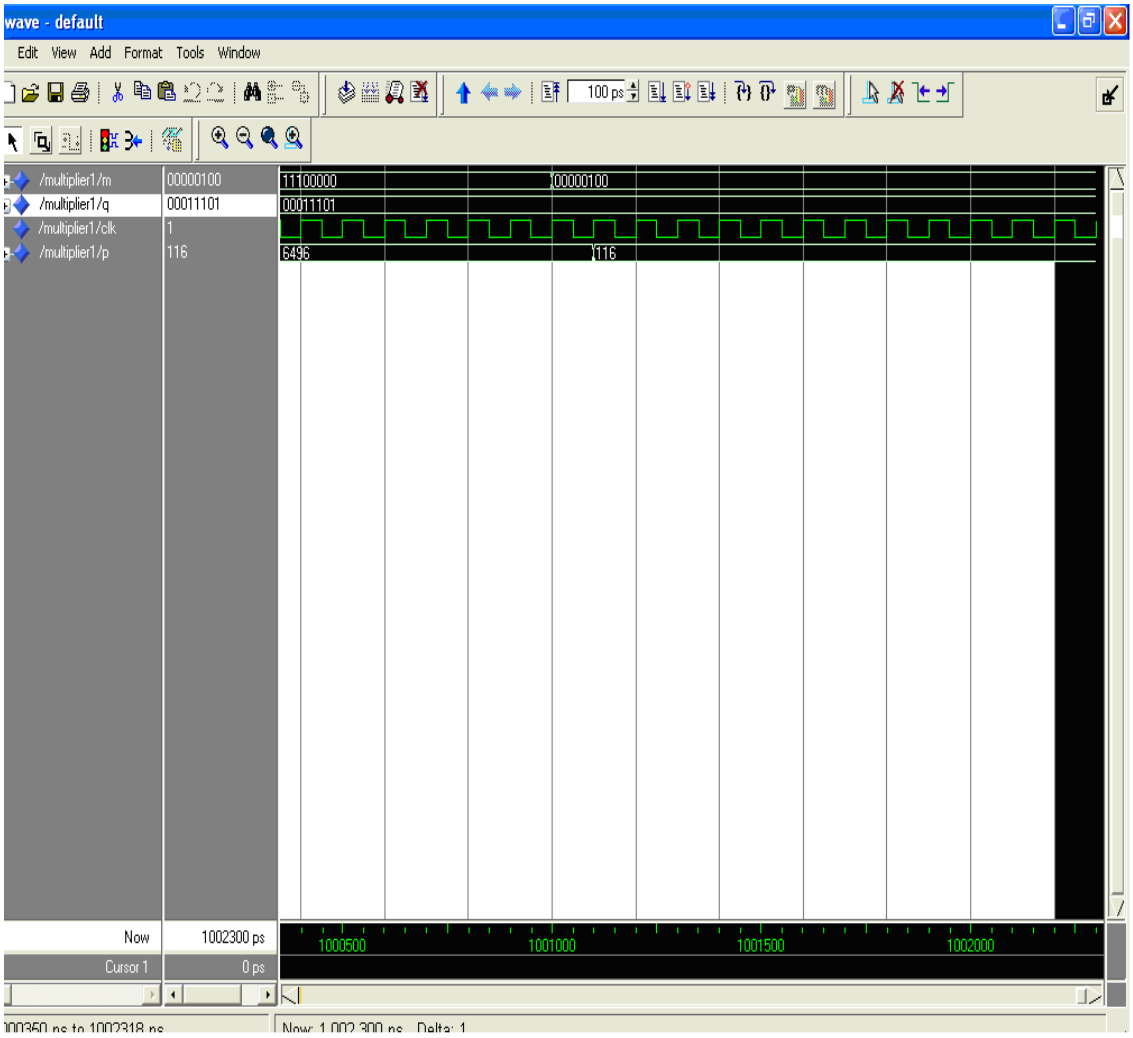

Fig B.3

B.1.1.3 Mux4 :1

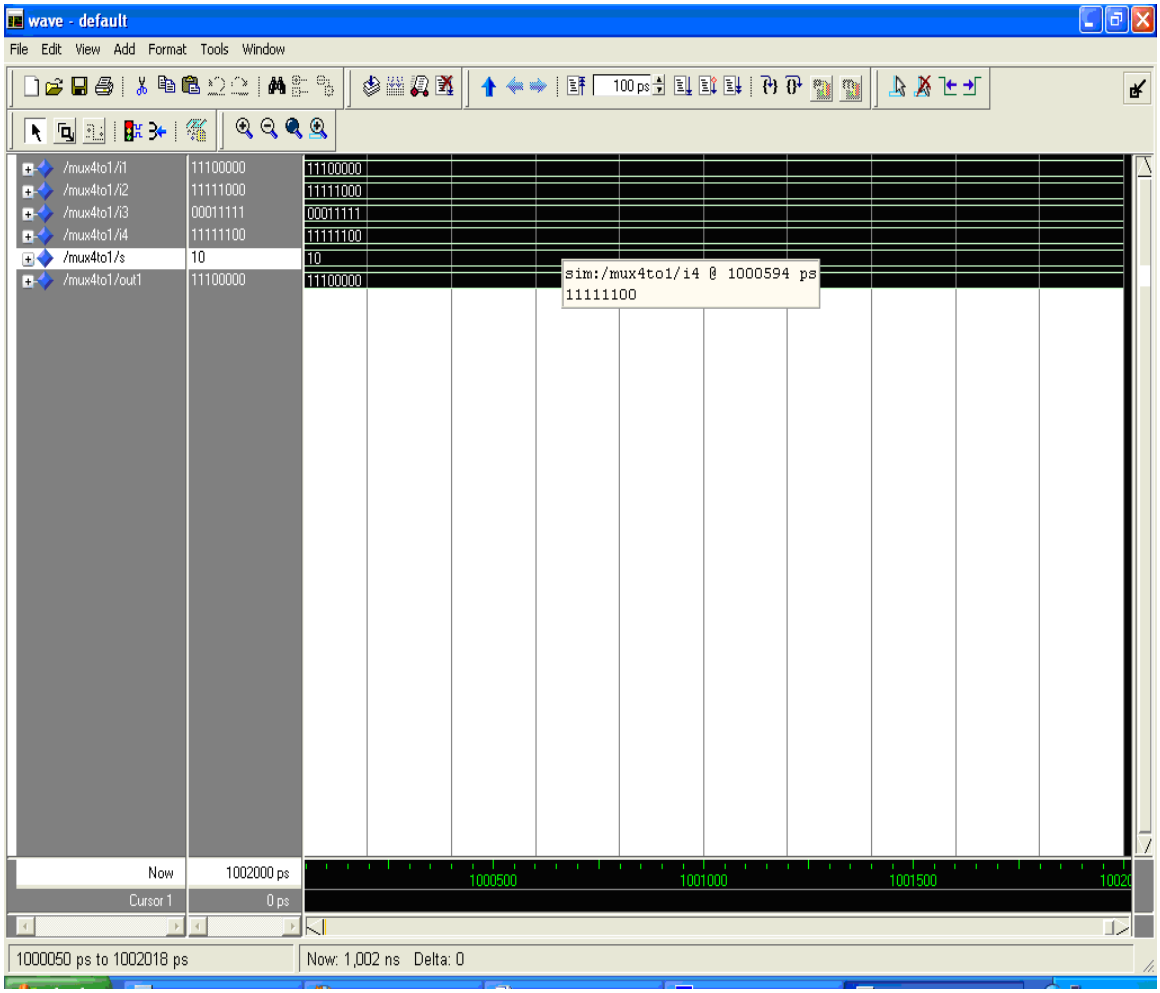

Fig B.4

B.1.1.4 Mux2 : 1

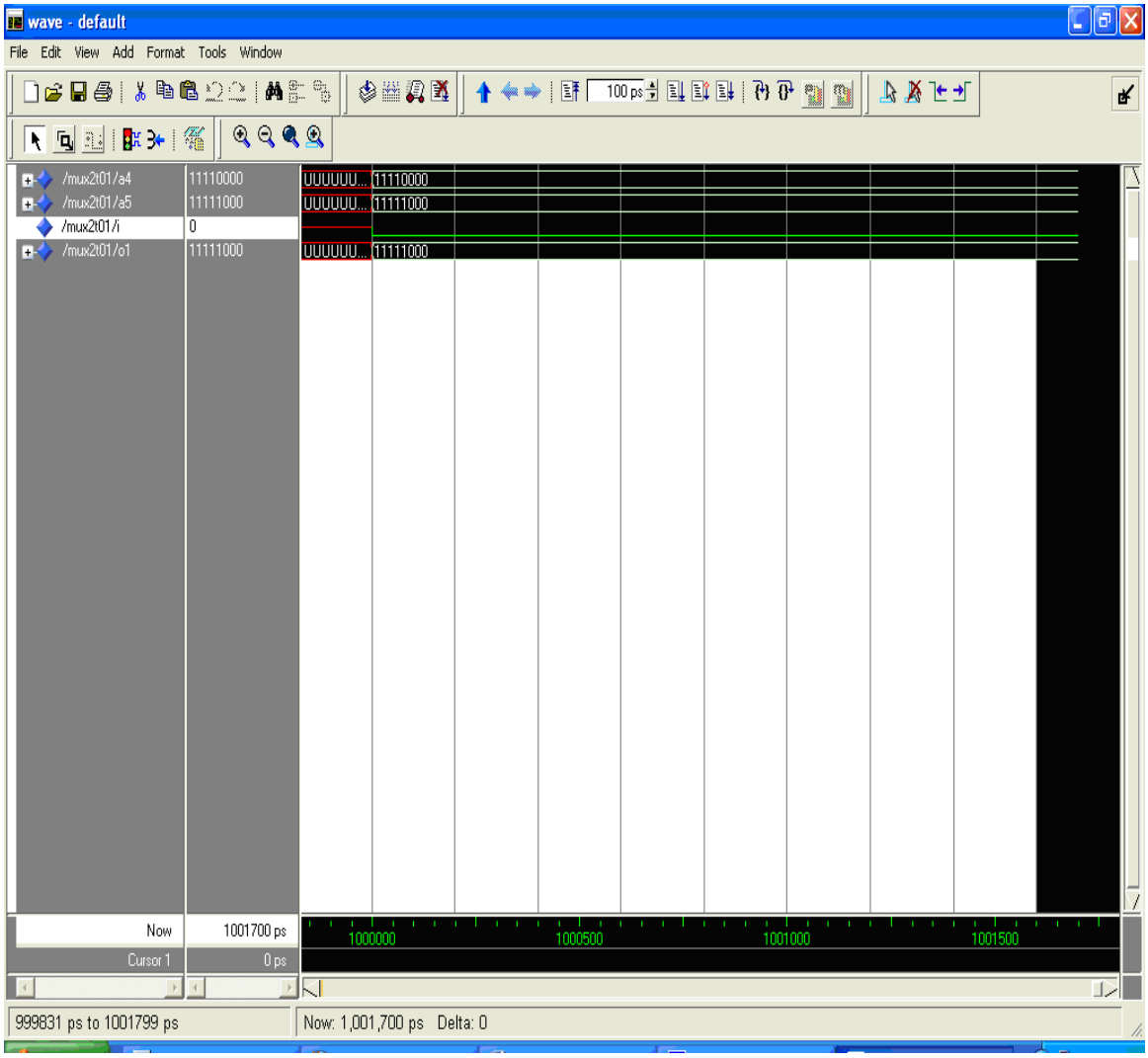

Fig B.5

B.1.1.5 Comparator:

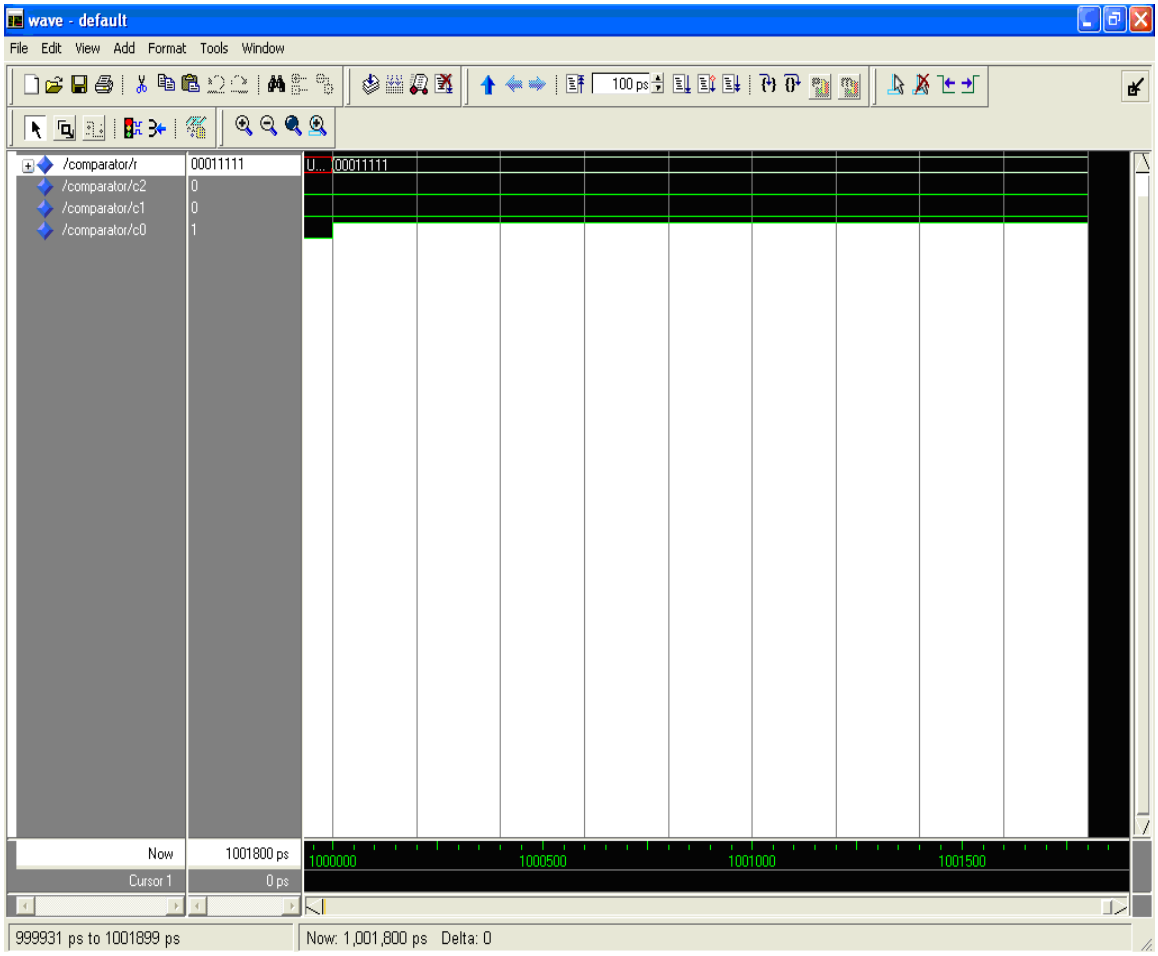

Fig B.6

B.1.1.6 Adder(8 bit):

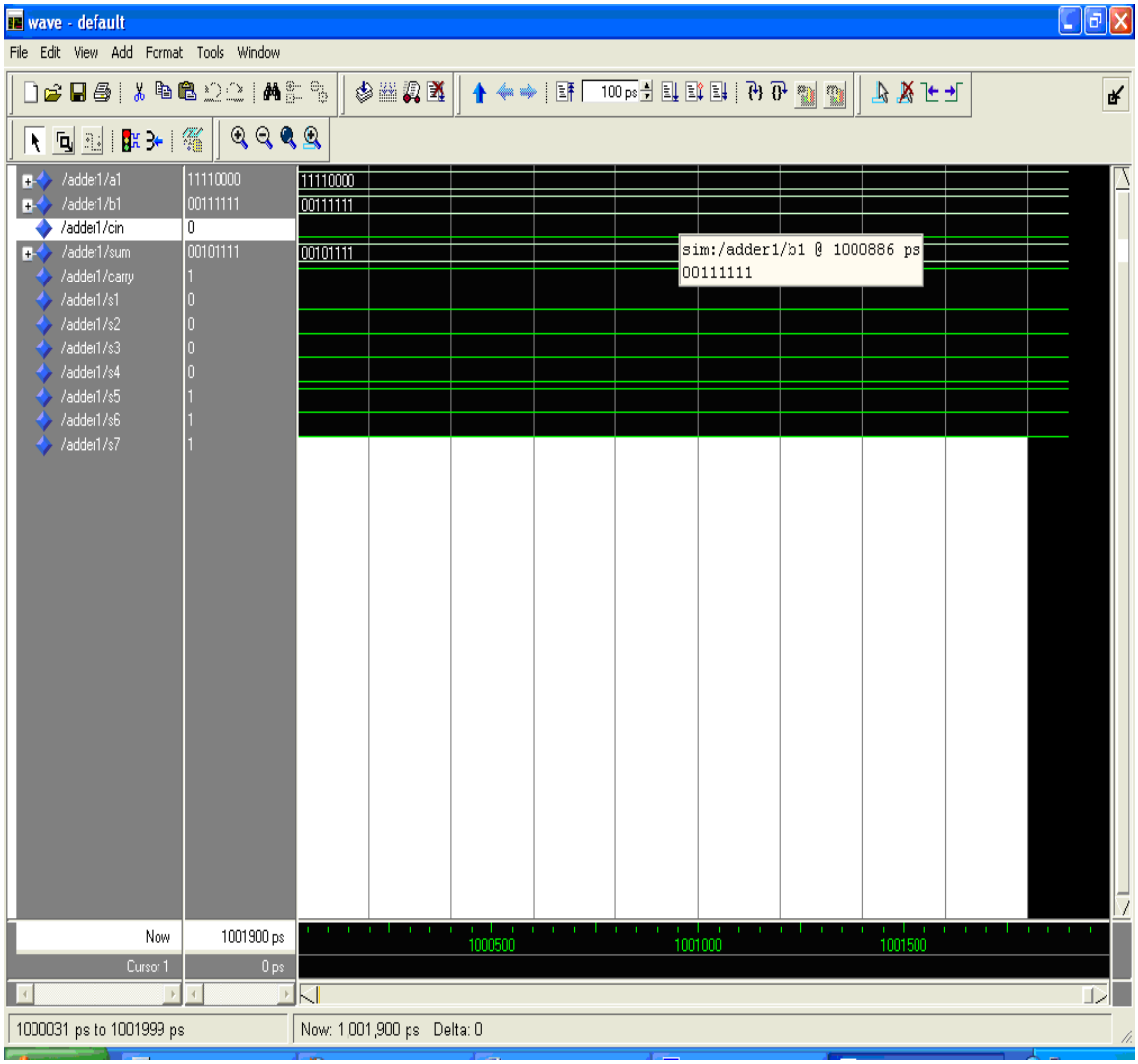

Fig B.7

B.1.2 Image Negative transformation:

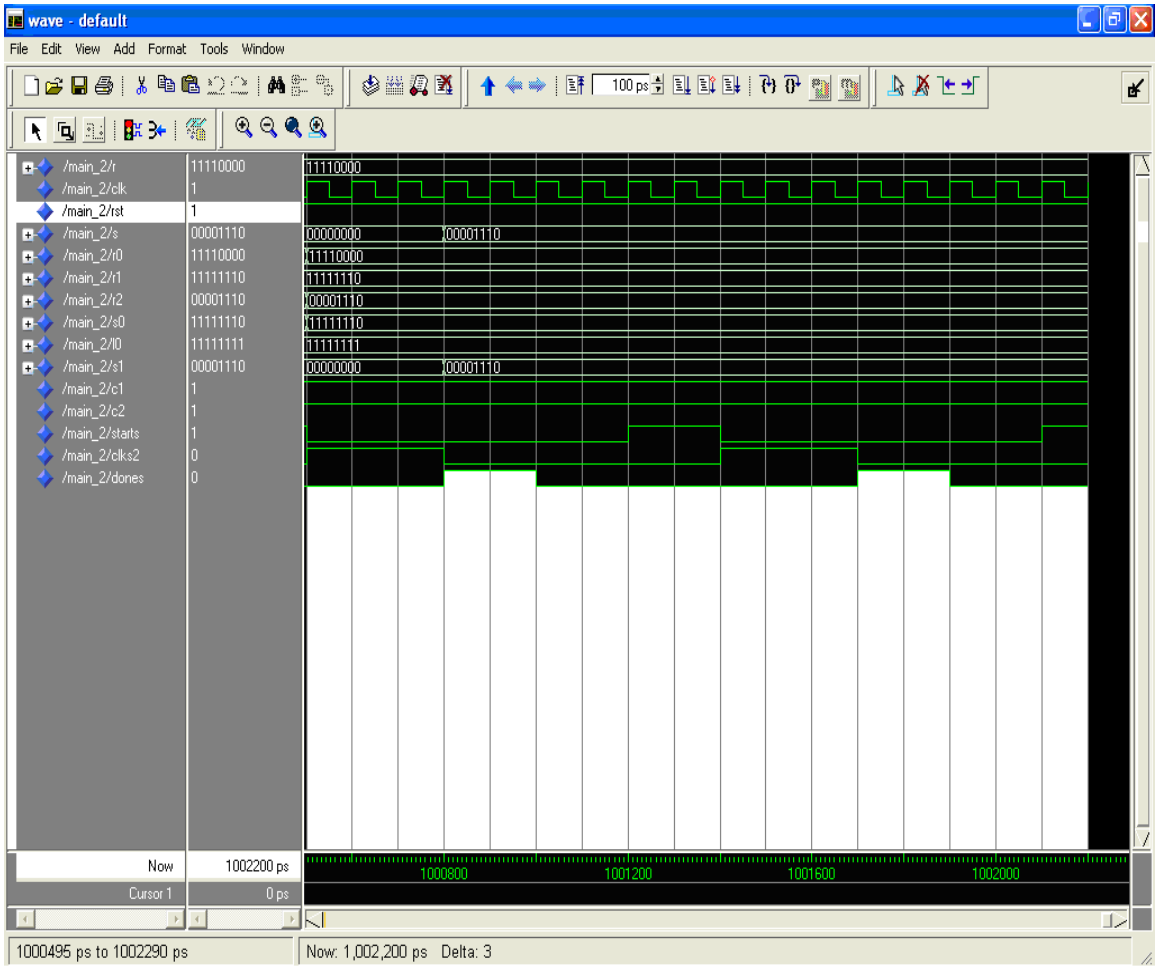

FigB.8

B.1.2.1 Control path of image negative transformation:

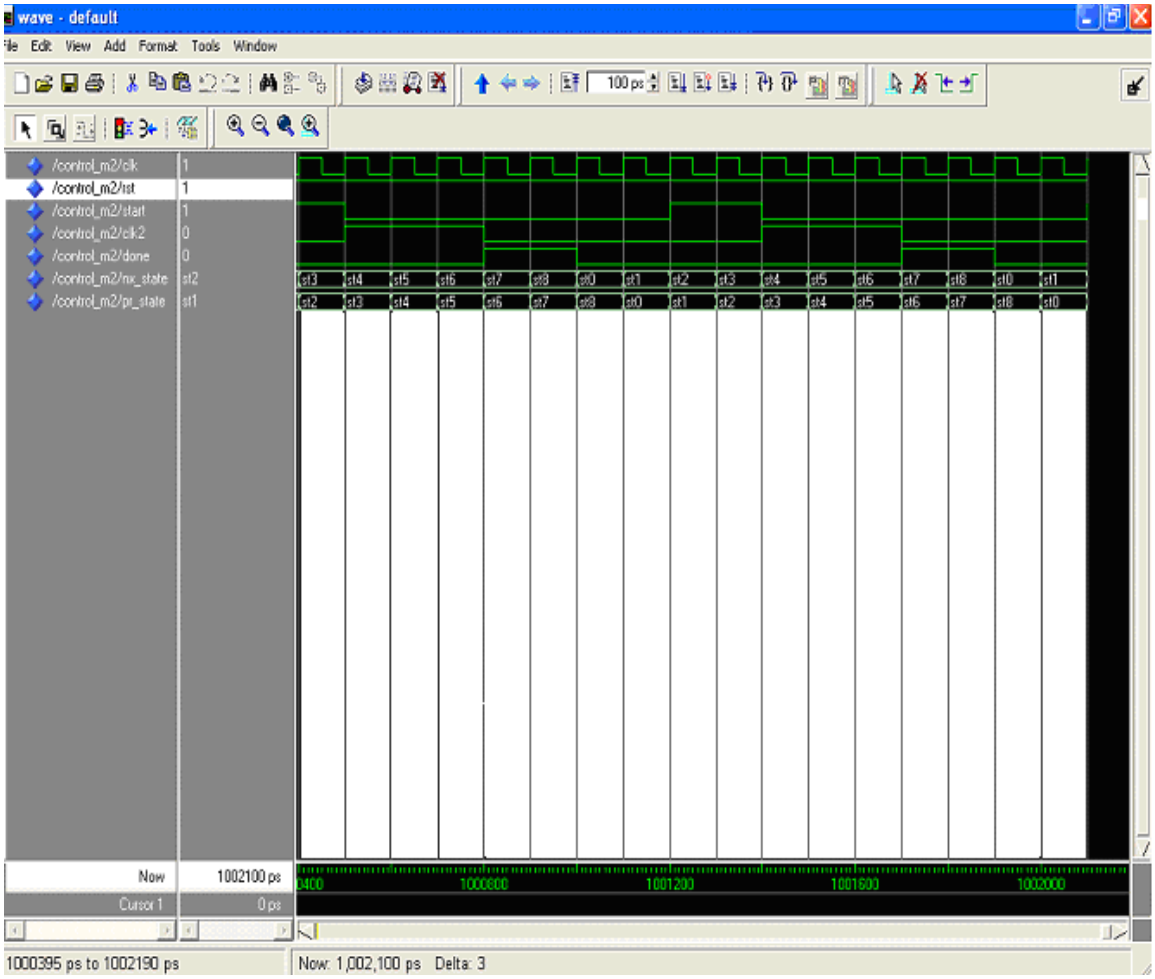

Fig B.9

B.1.3 Log- transformation Algorithm:

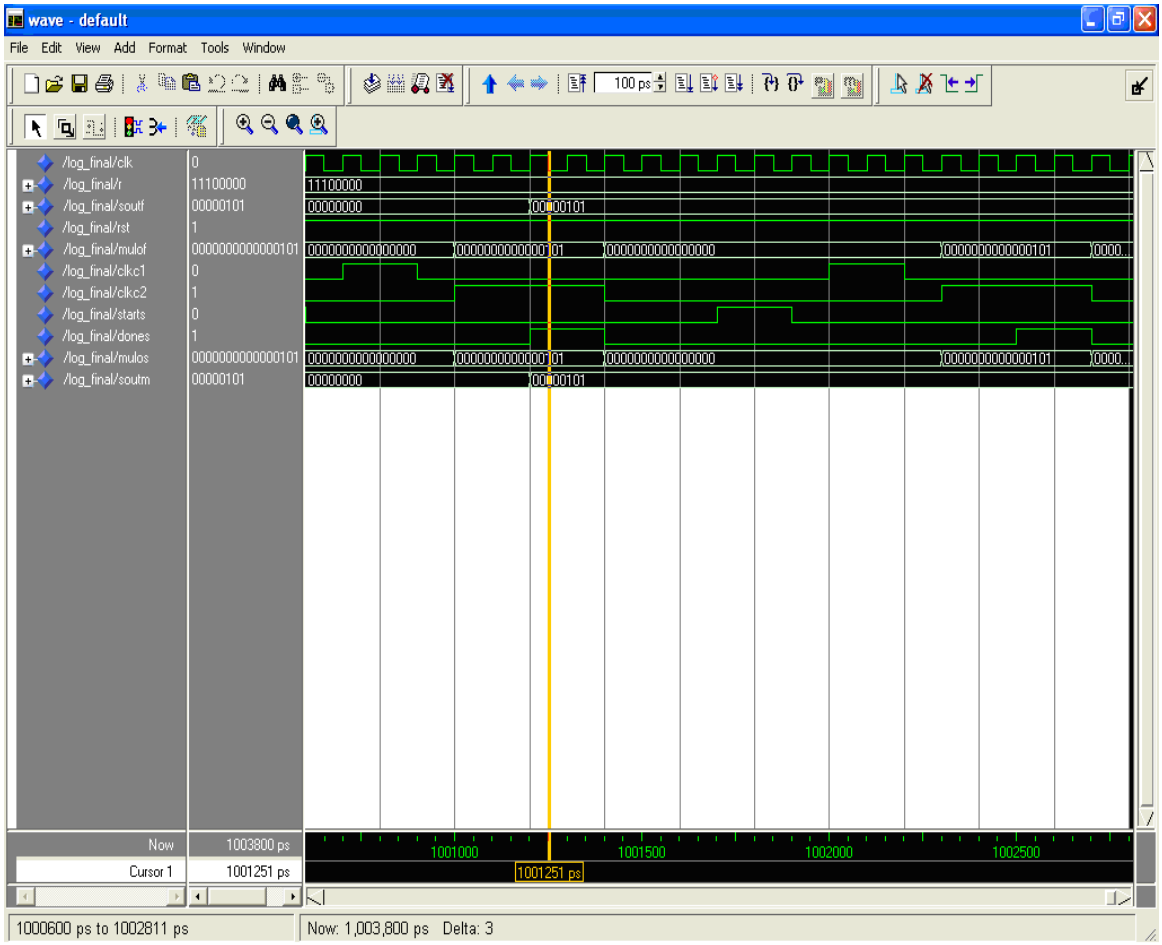

Fig B.10

B.1.3.1 Logarithmic Block:

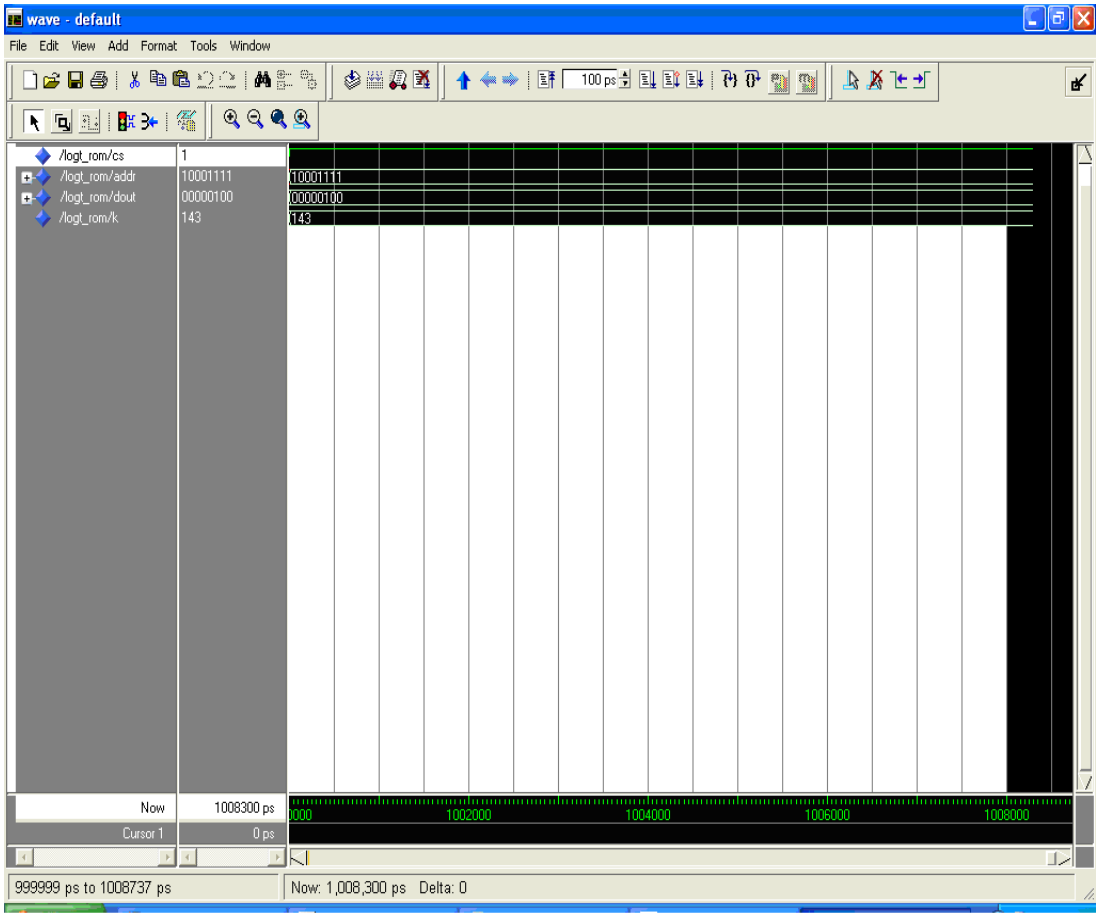

Fig B.11

B.1.3.2 Control path of Log- transformation Algorithm:

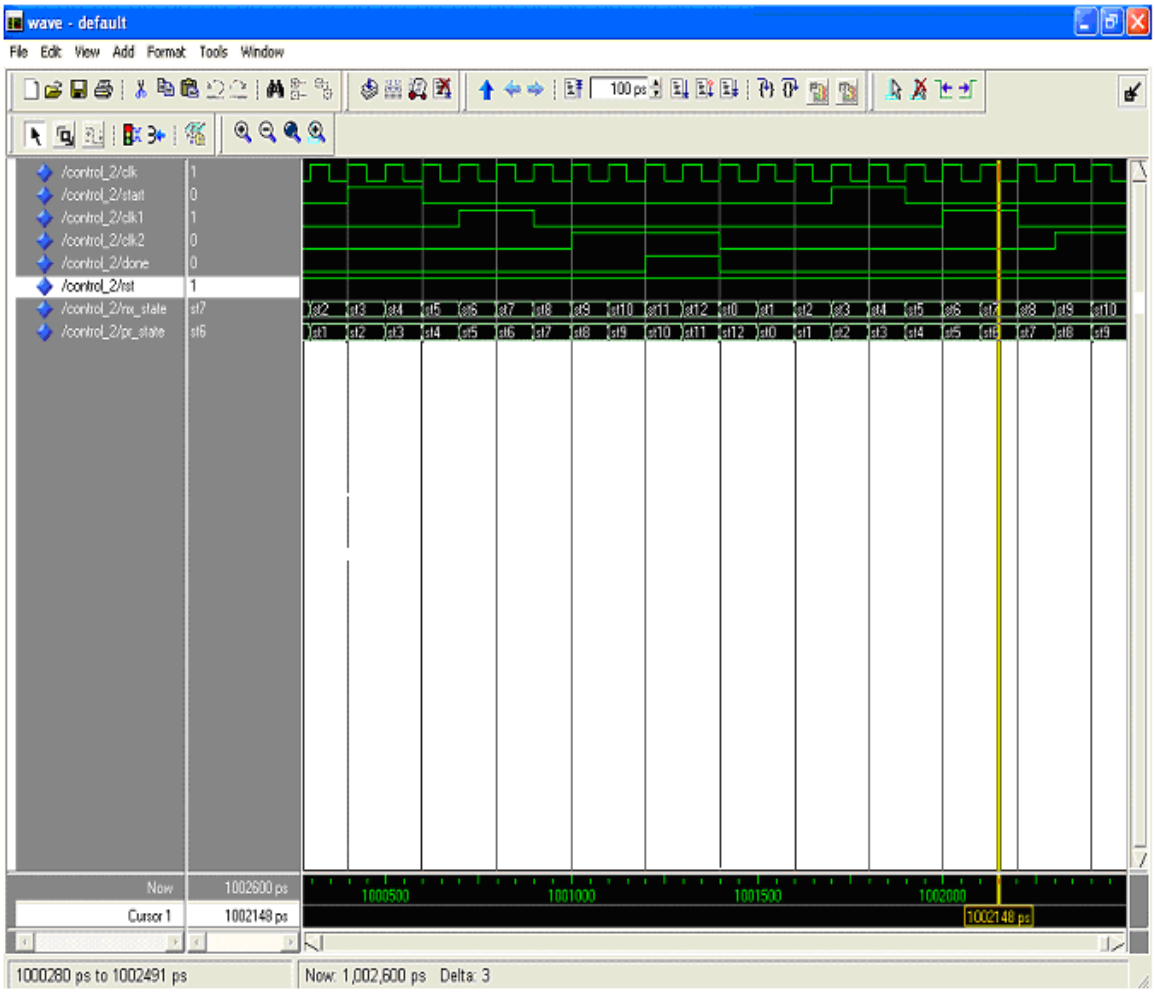

Fig B.12

B.1.4 Histogram Equalization:

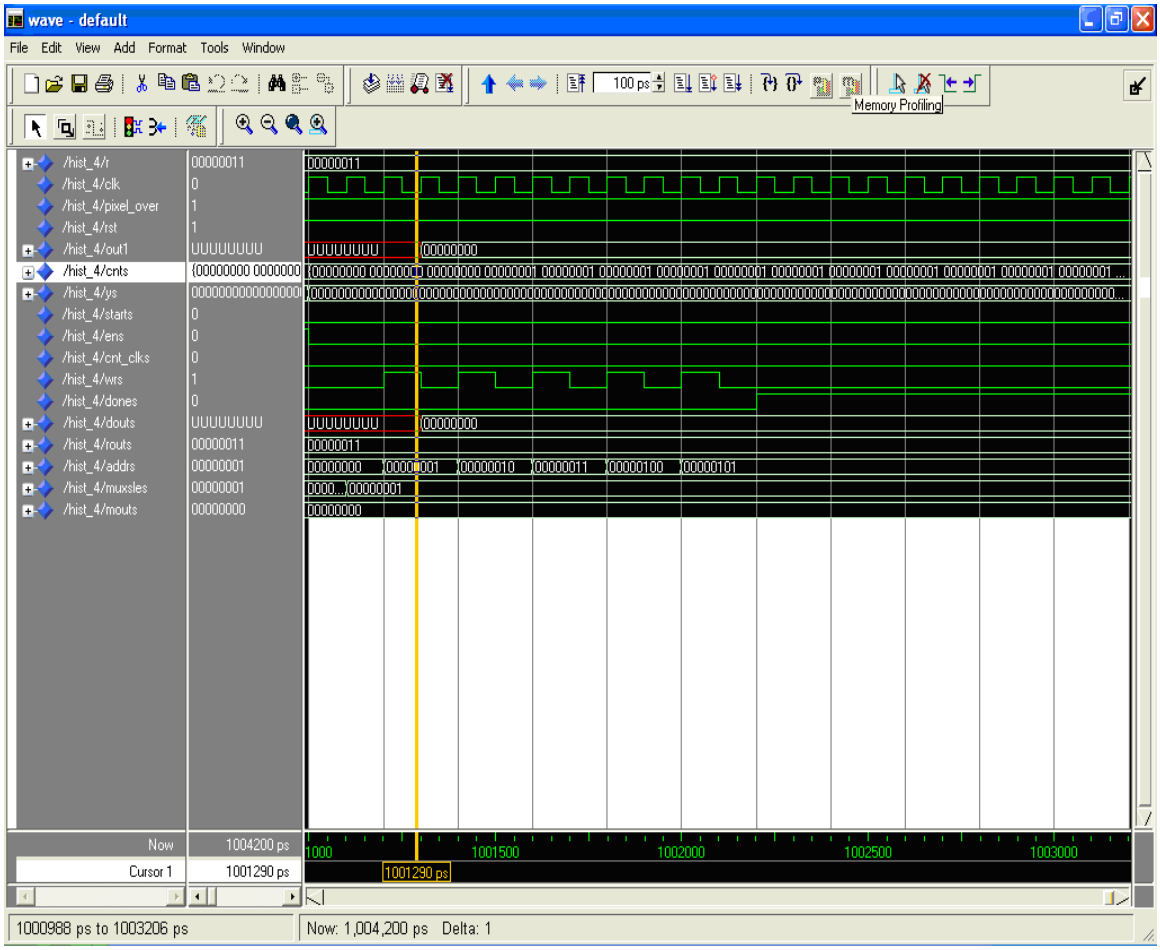

Fig B.13

B.1.4.1 Decoder 8 : 256:

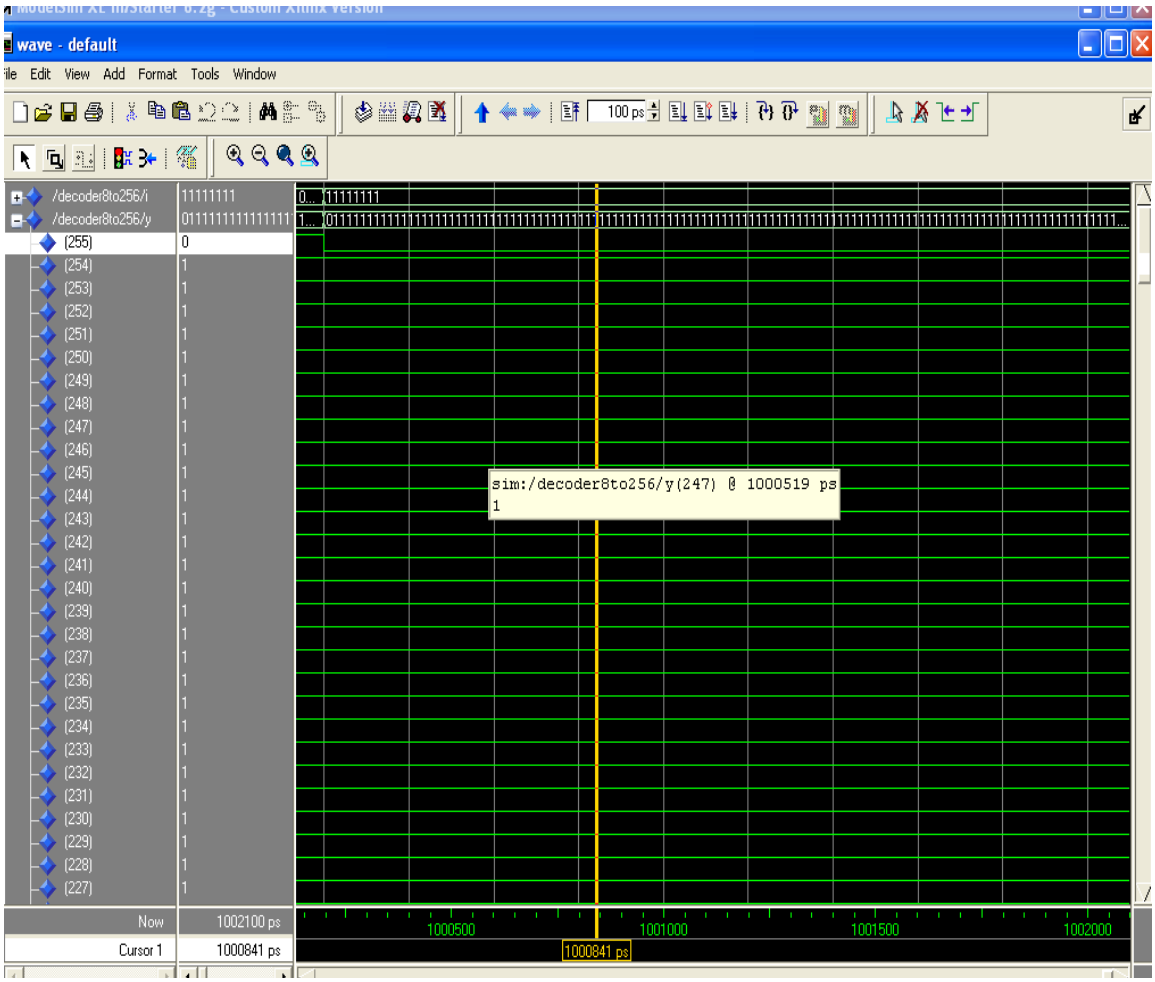

Fig B.14

B.1.4.2 Counter8 bit:

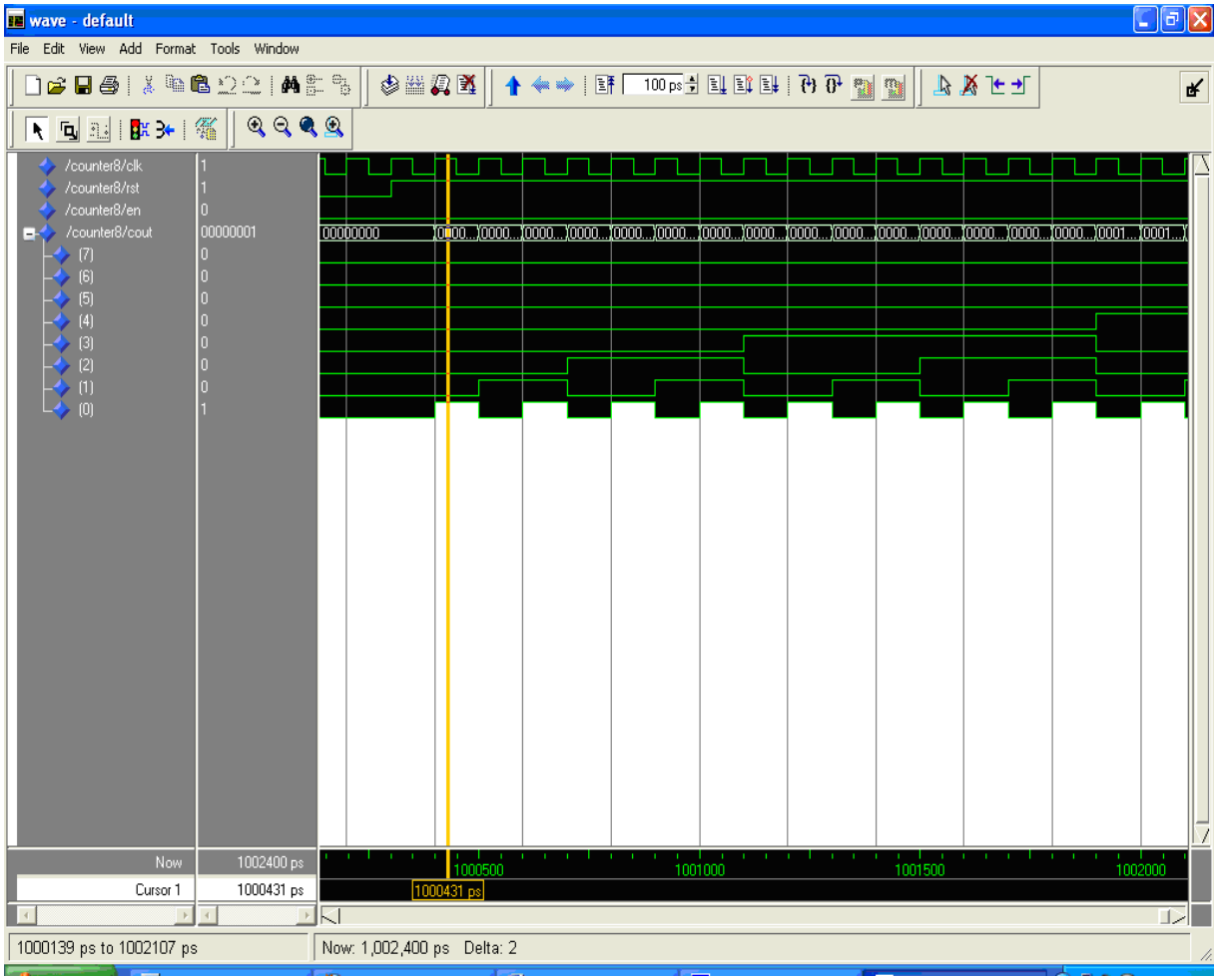

Fig B.15

B.1.4.3 MUX 256:1

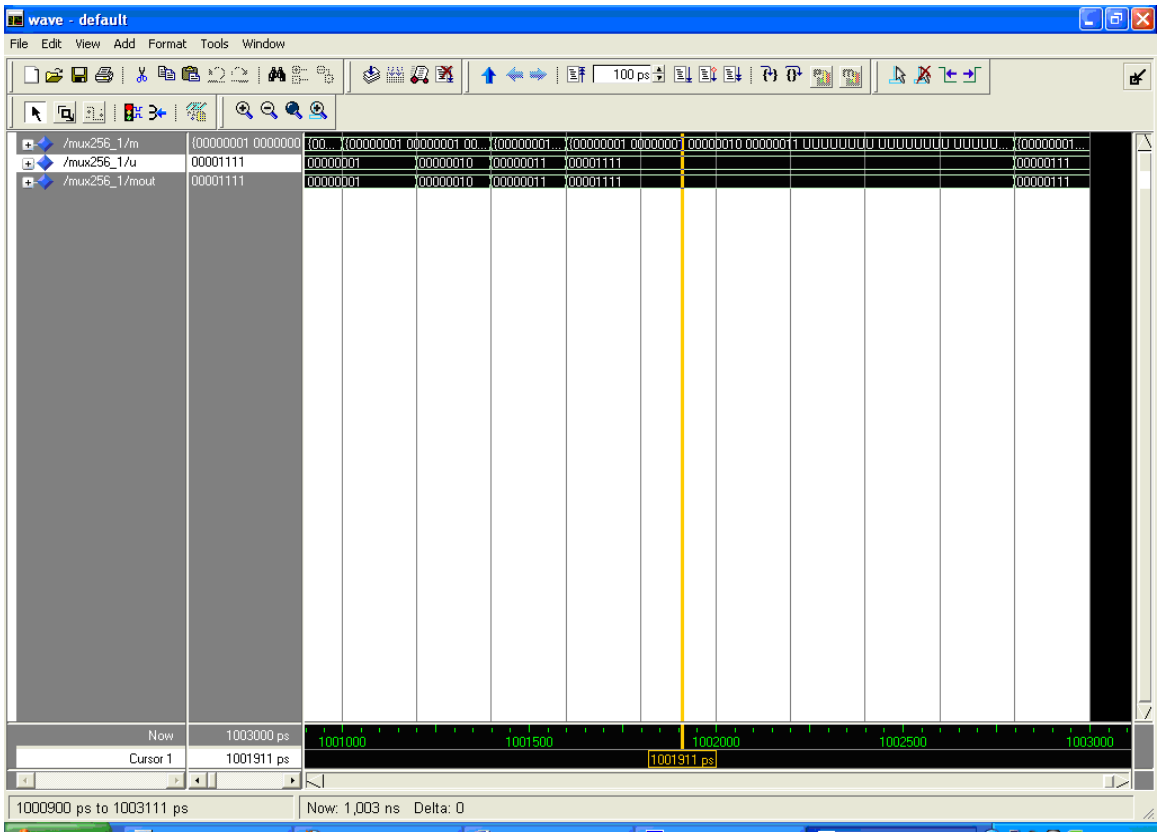

Fig B.16

B.1.4.4 RAM 256:

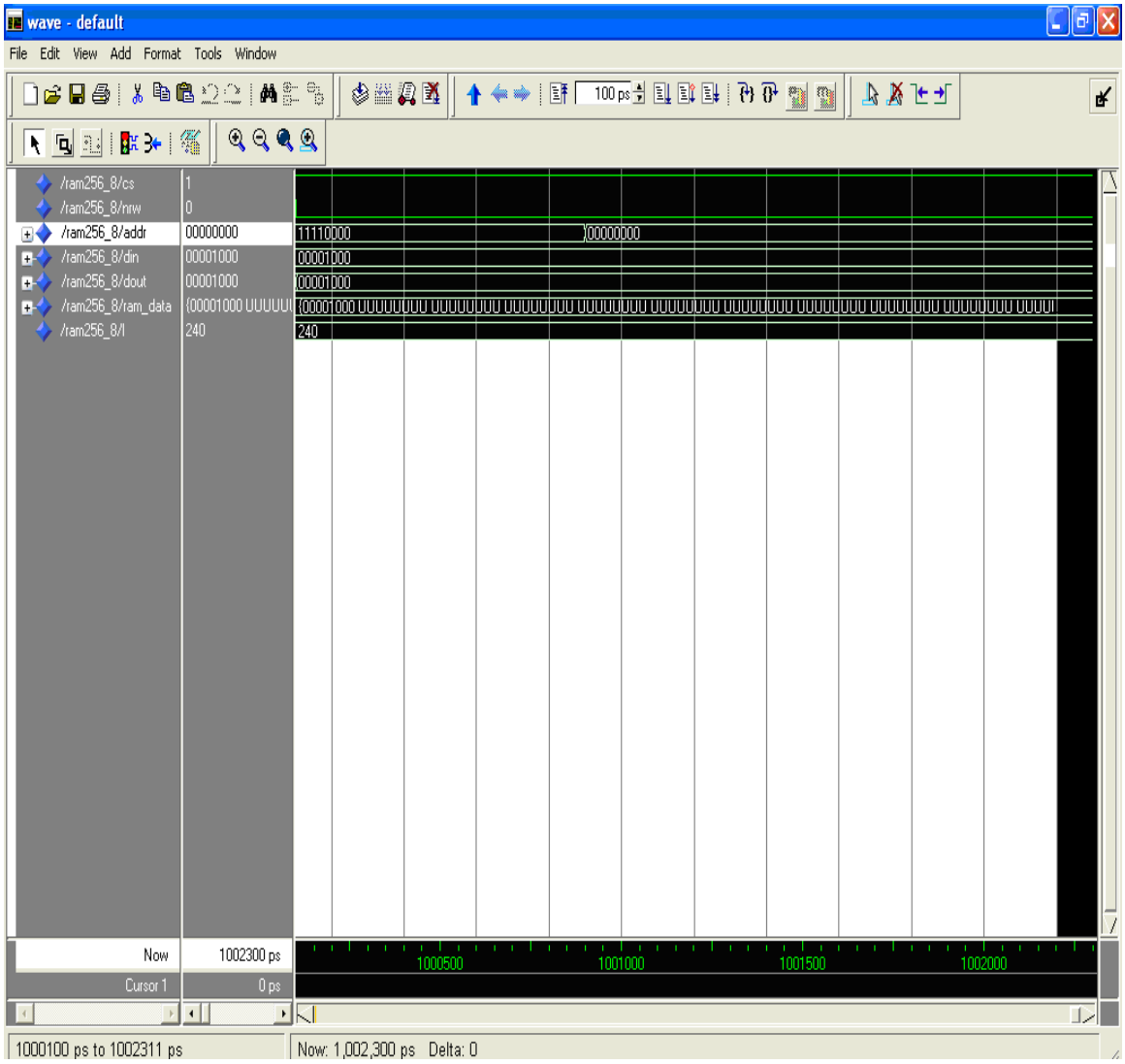

Fig B.17

B.1.4.5 Control path for histogram equalization:

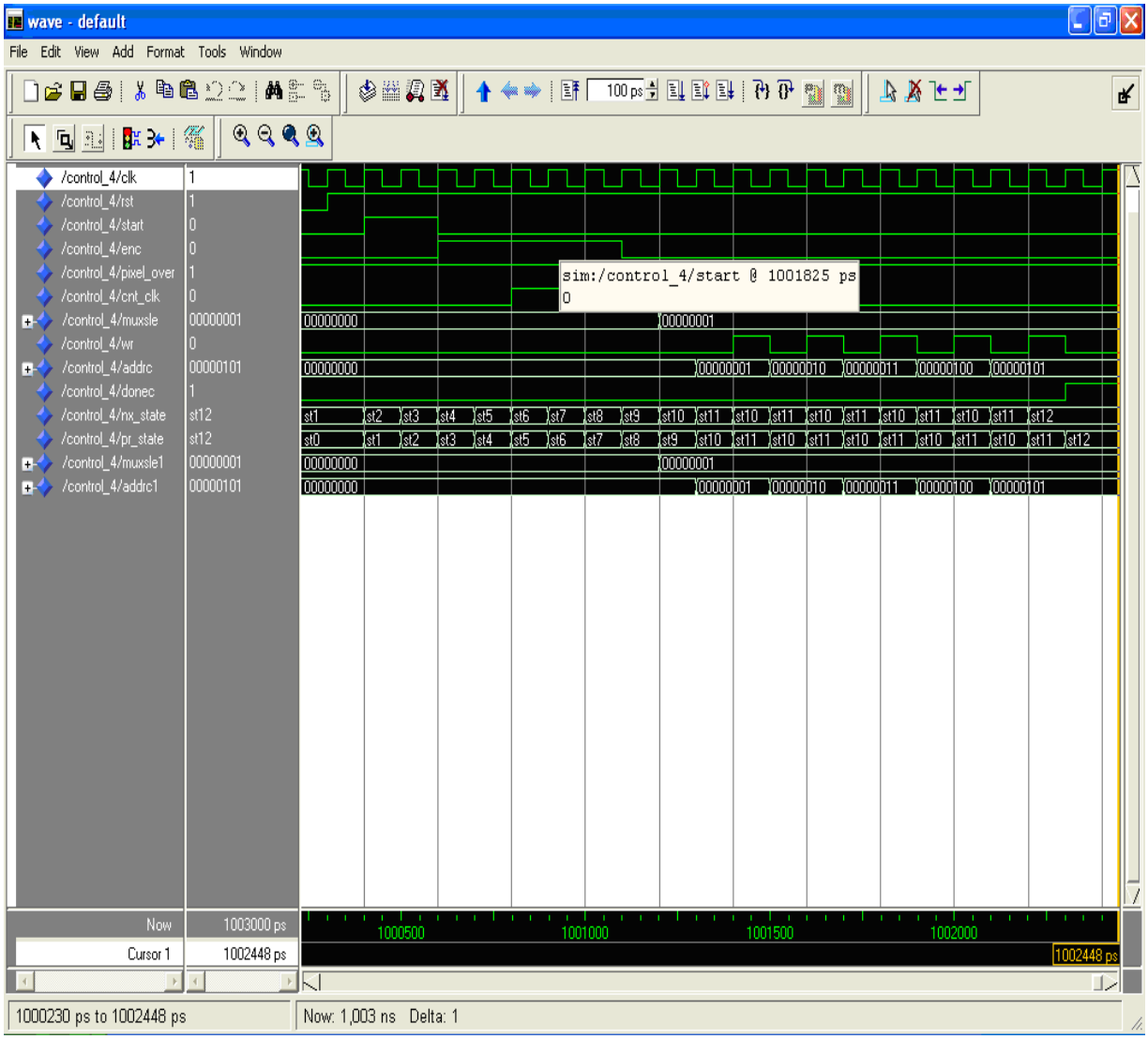

Fig B.18

List of Publications

1. Hitendra Gupta and K.K. Sharma, "FPGA Implementation of Visible Watermarking Processor"*, Proceedings of 13th IEEE/VSI VLSI Design and Test Symposium*, July 2009.

2. Hitendra Gupta, K.K. Sharma and S.D. Joshi, "VLSI Architecture and FPGA Implementation of Image Enhancement Algorithms", *Proceedings of 15th IEEE/VSI VLSI Design and Test Symposium*, July 2011.

3. Hitendra Gupta, K.K. Sharma and S.D. Joshi, "A Weighted Logarithmic Model based Enhancement of Weather Degraded Images", *International Journal of Signal Processing, Image Processing and Pattern Recognition (IJSIP),* Vol.6, No.6 (2013), pp.229-244, http://dx.doi.org/10.14257/ijsip.2013.6.6.22.

4. Hitendra Gupta, Kamalesh Kumar Sharma & Shiv Dutt Joshi (2015), "Resource Efficient FPGA Implementation of Adaptive Image Enhancement Algorithms", *IETE Journal of Research*, 61:4, 429-439, DOI: 10.1080/03772063.2015.1009397.
[Received Best Paper Award]